PHYS490 – Advanced Nuclear Physics

Contents

List of Figures

Generated: February 5, 2009

1: Nucleon-Nucleon Force

1.1 The Pauli (Iso)Spin Matrix

Matrix mechanics was formulated by Born, Heisenberg, and Jordan (1925) — introduction of commutation relations:

$$[M_x, M_y] = -i\hbar M_z, \text{ cyclic}, \tag{1}$$

for components of angular momentum $\underline{M}$. For intrinsic spin (takes only two values: *up* or *down*):

$$\underline{s} = \frac{1}{2}\hbar\underline{\sigma}, \tag{2}$$

where the components of $\underline{\sigma}$ are the *Pauli spin matrices*:

$$\sigma_1 = \begin{pmatrix} 0 & 1 \\ 1 & 0 \end{pmatrix} ; \ \sigma_2 = \begin{pmatrix} 0 & -i \\ i & 0 \end{pmatrix} ; \ \sigma_3 = \begin{pmatrix} 1 & 0 \\ 0 & -1 \end{pmatrix}$$

These have some interesting relations:

$$\sigma_1\sigma_2 = i\sigma_3 \ ; \ \sigma_2\sigma_1 = -i\sigma_3 \ ; \ \sigma_2\sigma_3 = i\sigma_1,$$

and $\sigma_1^2 = \sigma_2^2 = \sigma_3^2 = 1$.

In the fixed (*quantised*) 3-direction:

$$s_3 \begin{pmatrix} \psi_1 \\ \psi_2 \end{pmatrix} = \frac{\hbar}{2} \begin{pmatrix} \psi_1 \\ -\psi_2 \end{pmatrix}. \tag{3}$$

The two-component wavefunction satisfies a Schrödinger equation of the form:

$$H\psi = i\hbar\frac{\partial\psi}{\partial t}, \tag{4}$$

where H is a 2×2 matrix and ψ is a 1×2 matrix (column vector).

In analogy, the *Pauli Isospin Matrix* $\underline{\tau} = 2\underline{t}$ is defined in an analogous manner, i.e.

$$\tau_1 = \begin{pmatrix} 0 & 1 \\ 1 & 0 \end{pmatrix} ; \ \tau_2 = \begin{pmatrix} 0 & -i \\ i & 0 \end{pmatrix} ; \ \tau_3 = \begin{pmatrix} 1 & 0 \\ 0 & -1 \end{pmatrix}$$

with $\tau_1^2 = \tau_2^2 = \tau_3^2 = 1$.

Also:

$$\tau_\pm = \frac{1}{2}\left(\tau_1 \pm i\tau_2\right), \tag{5}$$

with

$$\tau_+ = \begin{pmatrix} 0 & 1 \\ 0 & 0 \end{pmatrix} \ ; \ \tau_- = \begin{pmatrix} 0 & 0 \\ 1 & 0 \end{pmatrix}$$

τ_+ turns a neutron into a proton, and
τ_- turns a proton into a neutron, i.e.

$$\tau_+|n\rangle = |p\rangle \;;\quad \tau_-|p\rangle = |n\rangle; \qquad (6)$$
$$\tau_+|p\rangle = \tau_-|n\rangle = 0.$$

1.2 Addition of (Iso)Spin

Eigenvalue equation with $\underline{s} = \frac{1}{2}$ (i.e. $s = \frac{1}{2}$):

$$\begin{aligned} \underline{s}^2\psi &= s(s+1)\hbar^2\psi \qquad (7)\\ &= \frac{1}{2}\left(\frac{1}{2}+1\right)\hbar^2\psi = \frac{3}{4}\hbar^2\psi \end{aligned}$$

Therefore:

$$\begin{aligned} \underline{s}^2 &= \frac{3}{4}\hbar^2 \\ s_z &= \pm\frac{1}{2}\hbar \quad \text{proton or neutron} \end{aligned}$$

— projection of *intrinsic* spin of nucleon on z-axis.
Define $\underline{\sigma}\hbar = 2\underline{s}$ where $\underline{\sigma}$ is the *Pauli Spin Matrix*.
Then:

$$\underline{\sigma}^2\hbar^2 = 4\underline{s}^2 = 3\hbar^2 \qquad (8)$$

and therefore:

$$\underline{\sigma}^2 = 3 \qquad (9)$$

Figure 1: Addition of two vectors

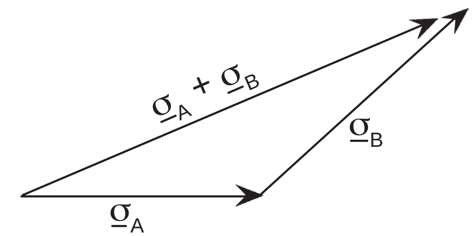

$$\begin{aligned} (\underline{\sigma}_A + \underline{\sigma}_B)^2 &= \underline{\sigma}_A^2 + \underline{\sigma}_B^2 + 2\underline{\sigma}_A.\underline{\sigma}_B \qquad (10)\\ 4\underline{S}^2/\hbar^2 &= 3 + 3 + 2\underline{\sigma}_A.\underline{\sigma}_B \qquad (11) \end{aligned}$$

Here $\underline{S} = \sum \underline{s}_i$

Thus if $\underline{S}^2 = 0$ (i.e. $S = 0$ *singlet state*) then:

$$\underline{\sigma}_A.\underline{\sigma}_B = -3 \qquad (12)$$

and if $\underline{S}^2/\hbar^2 = \underline{1} = S(S+1)/\hbar^2 = 2$ (i.e. $S = 1$ *triplet state*) then:

$$\underline{\sigma}_A.\underline{\sigma}_B = 1 \qquad (13)$$

In analogy to spin (*up* and *down* in real space) we can apply the same formalism to describe the nucleon (*up* and *down* in an abstract *isospin* space).

$$t_z = -\frac{1}{2} \quad \text{proton } \textit{down} \tag{14}$$

$$t_z = +\frac{1}{2} \quad \text{neutron } \textit{up} \tag{15}$$

$\underline{t}$ is the vector in isospin space.

For the nucleus the total isospin is $\underline{T} = \sum \underline{t}_i$ and $T_z = \frac{1}{2}(N - Z)$

In analogy with spin:

$$\underline{t}^2 = \frac{3}{4} \tag{16}$$

and $\underline{\tau} = 2\underline{t}$ where $\underline{\tau}$ is the *Pauli Isospin Matrix*.

For two nucleons A and B if $\underline{T}^2 = 0$ (i.e. $T = 0$ *singlet state*) then:

$$\underline{\tau}_A \cdot \underline{\tau}_B = -3 \tag{17}$$

and if $\underline{T}^2 = T(T+1) = 2$ (i.e. $T = 1$ *triplet state*) then:

$$\underline{\tau}_A \cdot \underline{\tau}_B = 1 \tag{18}$$

In 1932 the *neutron* was discovered. In the same year Heisenberg introduced a proton-neutron (*p-n*) potential for particles A and B of the form:

$$V_{AB} = P_{AB} F(r_{AB}) \; ; \; r_{AB} = |\underline{x}_A - \underline{x}_B| \,, \tag{19}$$

where:

$$P_{AB} = \tau_+^{(A)} \tau_-^{(B)} + \tau_-^{(A)} \tau_+^{(B)} . \tag{20}$$

Heisenberg showed that the nucleus as a p-n system system is amenable to a *non-relativistic* quantum mechanical treatment.

1.3 General Properties of the Nucleon-Nucleon Force

To lowest order, the interaction between two nucleons consists of an attractive central potential $V(r)$. However the following points must be noted:

• Force is spin dependent:

Evidence comes from, for example, the scattering of low energy neutrons from *ortho* ($I = 1$ i.e. spins of protons parallel) and *para* H_2 ($I = 0$ i.e. spins of protons antiparallel). The scattering cross-section from ortho-hydrogen, σ_{ortho} is 30 times σ_{para}. Also the $S = 0$ singlet state of the deuteron is unbound — The interaction must depend on the spins $\underline{\sigma}_A$ and $\underline{\sigma}_B$ of the nucleons.

Symmetry considerations restrict the possible form of the potential. Angular momentum is a *pseudovector* that does not invert under parity reversal ($\underline{r} \to -\underline{r}$). Under time reversal ($t \to -t$), all motions are reversed — terms such as $\underline{\sigma}_A$ and $\underline{\sigma}_B$ would violate time-reversal symmetry and are forbidden. Terms such as $\underline{\sigma}_A^2$, $\underline{\sigma}_B^2$, or $\underline{\sigma}_A.\underline{\sigma}_B$ are allowed. The last term ($\underline{\sigma}_A.\underline{\sigma}_B$) is the simplest involving both nucleon spins.

• Force is charge symmetric:

The cross section for neutron-neutron scattering, σ_{nn}, is almost the same as that for proton-proton scattering, σ_{pp}. To compare these the contribution from the *Coulomb* force has to be removed from σ_{pp}.

Note that both p-p and n-n scattering only involve π^0 exchange (see below).

• Force is nearly charge independent:

The cross-section for neutron-proton scattering, σ_{np}, is similar to σ_{nn} and σ_{pp}. The difference arises from the additional exchange of the $\pi^\pm$ which contributes to this interaction (Fig. 3). The $\pi^\pm$ meson has a different mass to the π^0.

• The nucleon-nucleon interaction has a non-central term:

A *tensor potential* mixes states of different ℓ (deuteron ground-state). Only terms that relate $\underline{r}$ to $\underline{\sigma}$ can contribute, such as $\underline{\sigma}.\underline{r}$ or $\underline{\sigma} \wedge \underline{r}$, i.e. $(\underline{\sigma}_A.\underline{r})(\underline{\sigma}_B.\underline{r})$ or $(\underline{\sigma}_A \wedge \underline{r}).(\underline{\sigma}_B \wedge \underline{r})$. From vector identities, the second form can be written in terms of the first form plus a term $\underline{\sigma}_A.\underline{\sigma}_B$. Since this has already been useed for the spin dependence, we use $V_T(r)S_{AB}$ where:

$$S_{AB} = 3\frac{(\underline{\sigma}_A.\underline{r})(\underline{\sigma}_B.\underline{r})}{r^2} - \underline{\sigma}_A.\underline{\sigma}_B. \tag{21}$$

This averages to zero over all angles.

• The nucleon-nucleon interaction may also depend on the relative velocity or momentum of the nucleons:

Forces dependent on velocity or momentum (vectors) cannot be represented by a scalar potential. The simplest form that does not violate parity or time-reversal invariance is:

$$V(r)(\underline{r} \wedge \underline{p}).\underline{S}, \tag{22}$$

where $\underline{S} = \underline{s}_A + \underline{s}_B$. The relative angular momentum of the nucleons is $\underline{\ell} = \underline{r} \wedge \underline{p}$ and hence the potential becomes:

$$V_{so}(r)\underline{\ell}.\underline{S}, \tag{23}$$

in analogy to the *spin-orbit* potential in atomic physics. Evidence — scattered nucleons can have their spins *polarised* in certain directions.

1.4 Repulsive Core

The repulsive core (Pauli Exclusion Principle) leads to a constant average separation between two nucleons, and the nuclear volume is proportional to the number of nucleons. It then follows that the radius is proportional to $A^{1/3}$.

Figure 2: Repulsive core

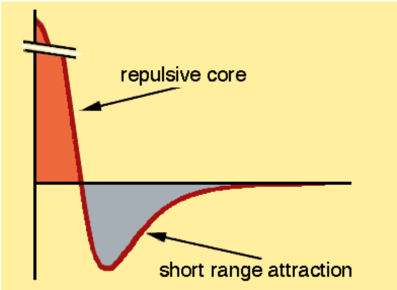

Radius of nucleon: $\sim 1 fm$; Radius of hard core: $\sim 0.2 fm$; Nucleon mean free path: $\sim 7 fm$! Volume of hard cores is only 2% of nuclear volume.

1.5 Exchange-Force Model

Evidence — (1) saturation of nuclear forces: approximately constant nuclear density and binding energy per nucleon as we go to heavier nuclei. A nucleon atracts only a small number of near neighbours, but repels at small distances to keep those neighbours from getting too close. This is analogous to a diatomic molecule where the electrons are shared or *exchanged* between the two atoms which achieve an equilibrium separation.

(2) Strong backward peaks in n-p scattering can be explained if the neutron and proton exchange places ($\pi^{\pm}$ exchange). The lightest of the mesons — the π-meson or *pion* is responsible for the major portion of the longer range ($1.0 - 1.5\ fm$) part of the nucleon-nucleon potential.
Masses — $\pi^{\pm}$: $139.6\ MeV/c^2$, π^0: $135.0\ MeV/c^2$.
At shorter ranges ($0.5 - 1.0\ fm$) two-pion exchange is probably responsible for the nuclear binding. At much shorter ranges ($0.25 fm$) the exchange of ω-mesons (mass: $783\ MeV/c^2$) may contribute to the *repulsive core*; ρ-mesons (mass: $769\ MeV/c^2$) may provide the *spin-orbit* part of the interaction.

1.6 One Pion Exchange Potential

Figure 3: Pion exchange

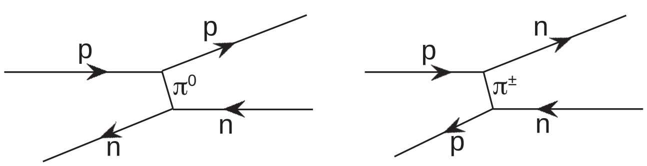

The origin of the nuclear force arises at the fundamental level from the exchange of gluons between the constituent quarks of the nucleons, but at low energies (i.e. < 1 GeV/ nucleon), i.e. interaction distance > 1 fm the interaction can be regarded approximately as being mediated by the exchange of π mesons.

At large distances the form of the potential is constructed as arising from the exchange of one π meson (hence OPEP, where *pion* $= \pi$ meson) so as to reproduce the known spin and charge properties of the force.

The form of this potential is

$$V_{\mathrm{OPEP}} = \tag{24}$$

$$g_s^2 \left(\frac{1}{3} \underline{\sigma}_A . \underline{\sigma}_B + S_{AB} \left[\frac{1}{3} + \frac{1}{\mu r} + \frac{1}{(\mu r)^2} \right] \right) \underline{\tau}_A . \underline{\tau}_B \frac{\mu^2 \mathrm{e}^{-\mu r}}{r}$$

where $\mu = m_\pi c/\hbar$, and

$$S_{AB} = 3(\underline{\sigma}_A . \underline{r})(\underline{\sigma}_B . \underline{r})/r^2 - \underline{\sigma}_A . \underline{\sigma}_B \tag{25}$$

1.7 The Deuteron

The deuteron consists of a bound proton-neutron system. Its ground state is the only state which is bound; the first excited state is unbound (Fig. 4).

Figure 4: Two-nucleon states

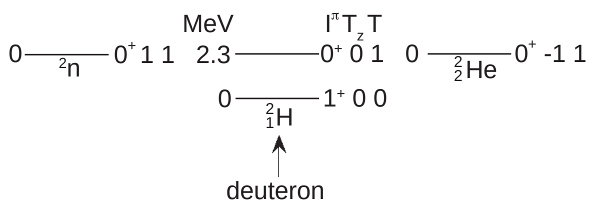

The ground state has total angular momentum and parity of $I^\pi = 1^+$.

Since

$$\underline{I} = \underline{L} + \underline{S} \tag{26}$$

and $\underline{S} = \underline{1}$ (i.e. the spins of the proton and neutron are in the same direction) for the ground state ($\underline{S} = 0$ for the unbound excited state) then $\underline{L} = 0$ or $\underline{2}$.

The deuteron is not a spherical nucleus.

In the standard proton-neutron picture of this simplest nucleus, its shape is largely determined by pion exchange which leads to strong noncentral *tensor* interactions. Its shape has been measured at high momentum transfers (q^2) corresponding to distances of the order of the proton radius.

Figure 5: The deuteron

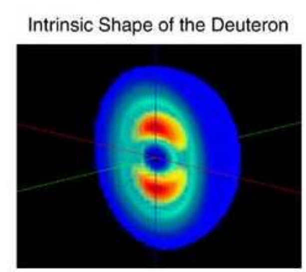

Evidence for L admixture comes from the measured electric quadrupole moment of $Q_0 = 2.82$ mb (from the hyperfine spectrum of deuterium). If the total wavefunction is written as

$$\psi = \alpha\psi(^3S_1) + \beta\psi(^3D_1) \tag{27}$$

with $\alpha^2 + \beta^2 = 1$.

In this expression the notation is ${}^{2S+1}L_I$, i.e. the same as that used in atomic spectroscopy ($S \rightarrow L = 0$, $P \rightarrow L = 1$, $D \rightarrow L = 2$).

The value of β can be obtained from the measured electromagnetic moments, and is about 0.02–0.08. Since it is non-zero then the potential does not commute with L, i.e. $[V, L] \neq 0$, otherwise the ground state would have a definite L value (e.g. 0).

This provides evidence that the n-p potential depends not only on the separation r but on the orientation of the intrinsic spins to $\underline{r}$, and accounts for the $S_{AB} = 3(\underline{\sigma}_A.\underline{r})(\underline{\sigma}_B.\underline{r})/r^2 - \underline{\sigma}_A.\underline{\sigma}_B$ term above. This term S_{AB} is called the *tensor* term.

The other members of the two-nucleon system are also shown in Fig. 4. The lowest energy levels of the di-neutron (^{2}n) and ${}^2_2$He and the first excited level of the deuteron (${}^2_1$H) are all *unbound* and have T_z values of 1, -1, and 0: they belong to the $\underline{T} = \underline{1}$ triplet. The ground state has $\underline{T} = 0$ and is bound.

If the nuclear force depended on $-(\underline{\tau}_A.\underline{\tau}_B)$ alone, as speculated by Heisenberg in analogy to the H_2^+ molecule, then the order of the $T = 0$ and $T = 1$ levels in the deuteron would have to be reversed.

1.8 Range of Nuclear Force

The range of an interaction is related to the mass of the exchanged particle. The Heisenberg uncertainty principle gives

$$\Delta E \Delta t \approx \hbar \tag{28}$$

A particle can only create another particle of mass m for a time $t \approx \hbar/mc^2$, during which interval the created particle can travel at most a distance ct. Taking ct as an estimate of the range of the interaction, R, gives:

$$R \approx \hbar/mc \tag{29}$$

This predicts that the force between two neutrons arising from the exchange of a π meson, which has a mass of ~ 140 MeV$/c^2$, has a range $R \approx 1.4$ fm, in good agreement with experiment. Analysis of high energy nucleon-nucleon scattering data reveals the presence of a *repulsive* core of ~ 0.5 fm. In terms of meson exchange theory this can arise from the exchange of a heavier *vector* mesons such as the ρ-meson and the ω-meson having $I^\pi = 1^-$.

2: Nuclear Behaviour

2.1 Mirror Nuclei

We have already seen that the force between two nucleons has the property of *charge symmetry* and *charge independence*. Fig. 6 shows the energy levels in the nuclei $^{22}_{10}$Ne, $^{22}_{11}$Na and $^{22}_{12}$Mg. The two nuclei $^{22}_{10}$Ne and $^{22}_{12}$Mg are examples of *mirror* nuclei, i.e. the number of protons in one is equal to the number of neutrons in the other.

Figure 6: Mirror nuclei: ^{22}Ne and ^{22}Mg

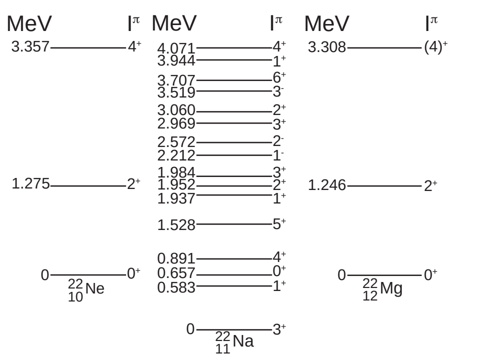

The similarity in the level schemes of mirror nuclei reflects the equality of the neutron-neutron and proton-proton force when the nucleons are in the same space-spin state, i.e. charge symmetry. The similarity between the levels in $^{22}_{10}$Ne and $^{22}_{12}$Mg and the levels at 0.657, 1.952 and 4.071 MeV in $^{22}_{11}$Na, which has a different number of neutron-proton pairs, implies charge independence.

This is an example of the similarity of the behaviour of the nucleons in the nucleus to that of the bare nucleon-nucleon force.

The above observation can be expressed in terms of isospin dependence of the nuclear force: the energy only depends on the total isospin $\underline{T}$ and not on its third component T_z where:

$$T_z = \sum_{\text{all nucleons}} t_z \tag{30}$$

where the summation is over *all* nucleons. Thus the comparable states in the three nuclei have $T_z = +1$, 0, -1, respectively, and associated with $\underline{T} = 1$. The ground state (and other states) in $^{22}_{11}$Na has $\underline{T} = 0$ with $T_z = 0$.

This is actually a simplification because we have ignored the fact that the ground state masses of these nuclei are different. This arises from:

- the neutron-proton mass difference
  This quantity depends on T_z of the nucleus.
- the Coulomb energy difference
  The Coulomb energy E_C depends on the average value of

$$\sum_p \frac{e^2}{4\pi\epsilon_0 r_{ij}} \tag{31}$$

In isospin formalism,

$$\begin{aligned} E_C &= \sum_{\text{all nucleons}} \left(\frac{1}{2} - t_{z_i}\right)\left(\frac{1}{2} - t_{z_j}\right)\frac{e^2}{4\pi\epsilon_0 r_{ij}} \\ &= \sum \left(\frac{1}{4} - \frac{(t_{z_i} + t_{z_j})}{2} + t_{z_i} t_{z_j}\right)\frac{e^2}{4\pi\epsilon_0 r_{ij}} \end{aligned} \tag{32}$$

Since $\sum(t_{z_i} + t_{z_j}) \sim T_z$ and $\sum t_{z_i} t_{z_j} \sim (T_z)^2$ then the energy difference arising from these two effects is given by:

$$E = a + bT_z + c(T_z)^2 \tag{33}$$

2.2 Isospin Substates

Again by analogy with spin, an isospin T state has $(2T+1)$ substates. For example, $T = 2$ corresponds to a vector of length $\sqrt{6}$ with components $-2 \leq T_z \leq +2$. The substates correspond to states in different nuclei, as shown in Fig. 7, for the $A = 12$ isobars:

Figure 7: Isospin substates

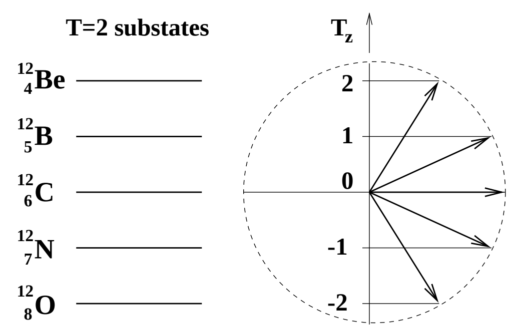

2.3 Isobaric Analogue States

Consider an odd-A nucleus made up of Z protons and N neutrons. A *mirror* nucleus is made by interchanging the numbers of protons and neutrons. At low mass, we can start with an $N = Z$ nucleus (A, N, Z) and add either one proton ($A+1$, N, $Z+1$) or one neutron ($A+1$, $N+1$, Z). The spectrum of proton states in the first nucleus should be equal to the spectrum of neutron states in the second, reflecting the charge independence of the nuclear force.

Figure 8: Isobaric analogue states

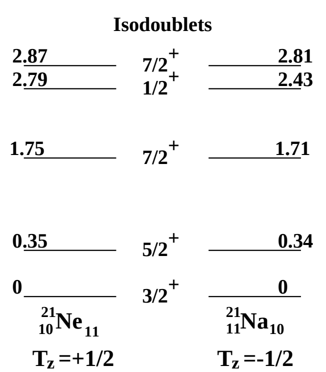

In the example of the mirror nuclei $^{21}_{10}\mathrm{Ne}_{11}$ and $^{21}_{11}\mathrm{Na}_{10}$, we have set the ground states to be equal by taking into account the neutron-proton mass difference (1.293 MeV). The levels for this $T = 1/2$ system form *isodoublets* with $T_z = \pm 1/2$. The only differences in the excitation energies should arise from the Coulomb energy (extra proton in ^{21}Na).

Next consider the $A = 18$ isobars. For $T = 0$ there is only an *isosinglet* state, but for $T = 1$ we can have three substates: $T_z = -1$, 0, $+1$ – *isotriplets*. At even higher excitation energy, $T = 2$ states are possible with five substates – we have to include $^{18}_{7}\mathrm{N}_{11}$ and $^{18}_{11}\mathrm{Na}_{7}$.

Figure 9: Isotriplets

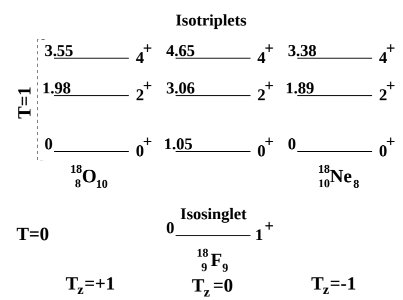

2.4 Independent Particle Model

In principle, if the form of the nucleon-nucleon force is known for bare nucleons, then the energy of the nucleon moving inside a nucleus can be calculated. This is a very difficult problem to solve as the nucleon interacts simultaneously with all the other nucleons.

Figure 10: Nuclear potential

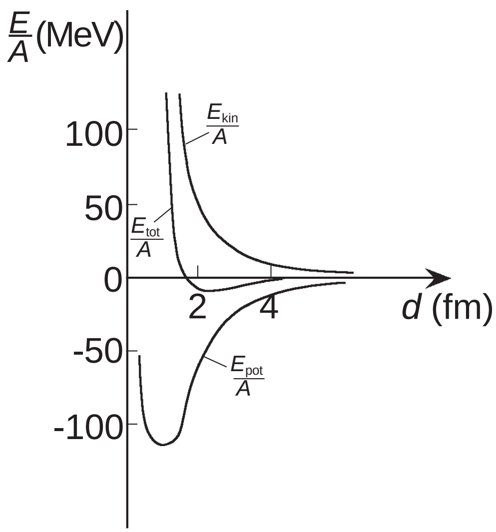

A schematic description of the nucleon energy as a function of nucleon separation is given in the Fig. 10.

The short range interaction between nucleons means that in a nucleus each nucleon moves in an **average** potential. The average separation of the nucleons, ~ 2.4 fm, is larger than the range of the nuclear force (~ 1.4 fm).

This ensures that the average potential, which results from the sum of all the nucleon-nucleon interactions, is hardly affected by the individual behaviour of the bulk of the nucleons. Nucleons cannot easily change their state unless these states are close to the Fermi surface (see below); this inhibition arises because of the Pauli exclusion principle.

The simplest model assumes that there is only an average potential governing the behaviour of the nucleons. The crudest approximation is to assume that each nucleon (labelled by the suffix i) sees the potential energy $U_i(r_i)$ arising from *pair* forces given by (Fig. 11):

Figure 11: Energy levels (ignoring proton Coulomb energy)

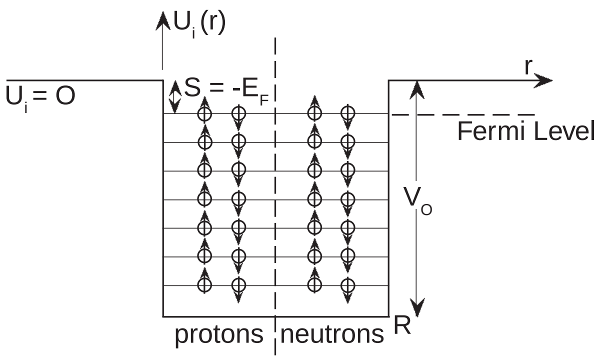

$U_i(r_i) = -V_0$ for $r < R$, the nuclear radius
and $U_i(r_i) = 0$ for $r > R$.
Hence the Hamiltonian is

$$H = \sum_i T_i + \frac{1}{2}\sum_i U_i(r_i) = \sum_i T_i - \frac{1}{2}\sum_i V_0 \quad (34)$$

where the factor $\frac{1}{2}$ arises to avoid counting the potential energies of pairs of nucleons twice.

The energy, $E = \langle H \rangle$, of the nucleus is given by:

$$E = \sum_i \langle T_i \rangle - \frac{1}{2}\sum_i \langle V_0 \rangle = \sum_i \langle T_i \rangle - \frac{1}{2}\sum_i V_0 \quad (35)$$

2.5 Degenerate Fermi Gas Model

A simple model in which nucleons are placed in a volume $V = 4\pi R^3/3$ and the interactions between them are ignored. The first nucleon will occupy the lowest energy state of the nuclear “box” and further nucleons must occupy higher energy states due to the Pauli exclusion principle.

In the limit of large volume, the number of states available for nucleon (fermion) occupation with momentum between p and $p + dp$ is:

$$dN(p) = \frac{2V 4\pi p^2 dp}{(2\pi\hbar)^3} = \frac{V p^2 dp}{\pi^2 \hbar^3} \quad (36)$$

where the factor 2 allows the two possible spin orientations of the nucleon. The total number of states available in the volume V with momentum below p_F is:

$$N = \int dN = \frac{V}{\pi^2\hbar^3}\int_0^{p_K} p^2 dp = \frac{V p_F^3}{3\pi^2\hbar^3} \quad (37)$$

p_F $(= \hbar k_F)$ is the *Fermi momentum* of the system and corresponds to the energy of the last nucleon.

A *Fermi sea* is formed. The sea is filled up to the energy corresponding to the Fermi momentum

$$E_F = \frac{p_F^2}{2m} = \frac{\hbar^2 k_F^2}{2m}; \tag{38}$$

above this energy it is empty (see Fig. 11). The ground state represents a degenerate Fermi gas.

The energy of the nucleus is given by Equation 35. In this model, $\sum \langle T_i \rangle = \frac{3}{5} T_F A$ where T_F is the kinetic energy at the Fermi level. The potential energies are the same for each nucleon ($-V_0$) so that $\sum V_0 = V_0 A$. The energy of the nucleus is then:

$$E = \frac{3}{5} T_F A - \frac{1}{2} V_0 A \tag{39}$$

and the binding energy per nucleon, B, is given by:

$$B = -E/A = -\frac{3}{5} T_F + \frac{1}{2} V_0 \tag{40}$$

The nuclear separation energy, S, is the difference between the energy of a nucleon outside the nucleus (0 in this model) and the energy of the Fermi level ($T_F - V_0$), so that:

$$\begin{aligned} S &= -T_F + V_0 \qquad (41) \\ &= AB(A,Z) - (A-1)B(A-1,Z) \end{aligned}$$

Now the nuclear force has the property of *saturation* so that $B(A,Z)$ is independent of A. This is a consequence of the Pauli exclusion principle, the spin and isospin dependence of the nuclear force and (less important) the repulsive core.

Thus

$$S = AB - (A-1)B = B = -T_F + V_0 \tag{42}$$

so that

$$T_F = \frac{5}{4} V_0 \tag{43}$$

and therefore

$$S = B = -\frac{1}{5} T_F \tag{44}$$

This is incorrect since for nuclei $S > 0$! We have to include a *momentum dependence* of the potential well which partially accounts for the non-central behaviour of the nuclear force. This implies that a nucleon has an *effective* mass (m^*) so that $m^* > m_n$ when moving in a nucleus.

2.6 Some nuclear quantities

Number density (A/V) (measured):

$$\rho(0) \approx 0.17 \quad fm^{-3}$$
$$\approx 1.5 \times 10^{18} \quad kg/m^3 \tag{45}$$

For comparison, the the density of lead is $11.3 \times 10^{-3} \quad kg/m^3$ and the Crab pulsar density is $\sim 10^{11} - 10^{13} \quad kg/m^3$ — a neutron star can be thought of as *macroscopic* nuclear matter.

Fermi Momentum:

$$\frac{p_F}{\hbar} = k_F \approx 1.4 \quad fm^{-1} \tag{46}$$

Fermi Energy:

$$E_F \approx 37 \quad MeV \tag{47}$$

Kinetic Energy of a nucleon in the nucleus:

$$\frac{3}{5}E_F \approx 25 \quad MeV \tag{48}$$

This corresponds to a velocity $(v/c)^2 \approx 0.1$.

3: Forms of Mean Potential

3.1 Single-Particle Shell Model

Assumption: Ignore the detailed interactions between nucleons — each particle moves in a state independent of the other particles. The *mean field* force is the average smoothed-out interaction with all the other particles. Each nucleon then only experiences a *central* force.

Figure 12: Mean field potential

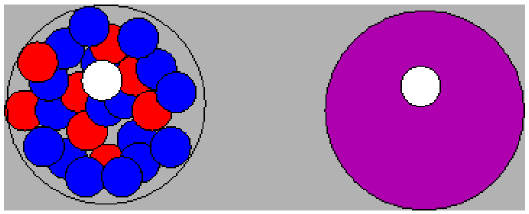

We have established that the nucleons moves in a mean potential. There are essentially two approaches to the determination of the potential: one in which an empirical form of potential is assumed (e.g. square well, harmonic oscillator, Woods-Saxon) and one in which the mean field is generated self-consistently from the nucleon-nucleon interaction.

3.2 Square Well Potential

This is the simplest form of potential (see Fig. 13) in which

$V_{\mathrm{SW}}(r) = -U_0$ for $r \leq R$

$V_{\mathrm{SW}}(r) = \infty$ for $r > R$

Since we have a spherically symmetric potential (this is the same approach for the more complex forms of potential) we separate the angular dependence of the wave function from the radial part (remember the nucleons move in *three dimensions*):

Figure 13: Square well potential

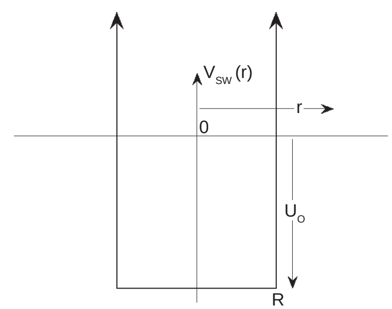

$$\psi(r,\theta,\phi) = R_{n\ell}(r) Y_{\ell m}(\theta,\phi) \tag{49}$$

The radial equation is:

$$\frac{d^2R(r)}{dr^2} + \frac{2}{r}\frac{dR(r)}{r} + \left[\frac{2m}{\hbar^2}(E+U_0) - \frac{\ell(\ell+1)}{r^2}\right] R(r) = 0 \tag{50}$$

The solutions are *Bessel* functions which satisfy the boundary condition $R_{n\ell}(R) = 0$ and the energies are given by:

$$E_{n\ell} = \left(\frac{\hbar^2}{2mR^2}\xi^2_{n\ell}\right) - U_0 \tag{51}$$

The quantum numbers are n, ℓ and m where $m = -\ell, -\ell+1, ..., 0, ..., \ell-1, \ell$, i.e. $2(2\ell+1)$ degeneracy (2 spin orientations).

Table 1: Square well shell closures

$n(\ell)$	ℓ	$2(2\ell+1)$	total	$\xi_{n\ell}$
1s	0	2	2	3.14
1p	1	6	8	4.49
1d	2	10	18	5.76
2s	0	2	20	6.28
1f	3	14	34	6.99

Note that for $\ell = 0$:

$$E_{n\ell} = \frac{n^2h^2}{8mR^2} - U_0 \tag{52}$$

3.3 Harmonic Oscillator

Fig. 14 shows the form of the potential in this case. The advantage of the harmonic oscillator, $V_{\rm HO}(r) = -U_0 + \frac{1}{2}m\omega^2r^2$, is that it is easy to handle analytically.

Figure 14: Harmonic oscillator potential

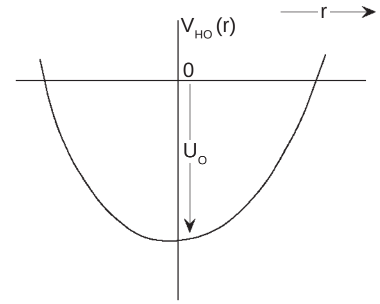

The radial equation is:

$$\frac{d^2R(r)}{dr^2} + \frac{2}{r}\frac{dR(r)}{r} + \left[\frac{2m}{\hbar^2}\left(E + U_0 - \frac{m\omega^2}{2}r^2\right) - \frac{\ell(\ell+1)}{r^2}\right]R(r) = 0 \tag{53}$$

The solutions are *Laguerre* polynomials, with energy levels:

$$E = \hbar\omega\left(N + \frac{3}{2}\right) - U_0 \tag{54}$$

For each oscillator quantum number N there are quantum numbers $n\ell$ which satisfy:

$$2(n-1) + \ell = N, \quad N \geq 0, \quad n \geq 1, \quad 0 \leq \ell \leq N \tag{55}$$

Table 2: Harmonic oscillator shell closures

N	n	ℓ	$n(\ell)$	$2(2\ell+1)$	total
0	1	0	1s	2	2
1	1	1	1p	6	8
2	2,1	0,2	2s,1d	2+10	20
3	2,1	1,3	2p,1f	6+14	40
4	3,2,1	0,2,4	3s,2d,1g	2+10+18	70
5	3,2,1	1,3,5	3p,2f,1h	6+14+22	112

Note the parity for each oscillator shell is $(-1)^N = (-1)^\ell$.

The harmonic oscillator correctly predicts shell closures for ${}^4_2\mathrm{He}_2$, ${}^{16}_8\mathrm{O}_8$, and ${}^{40}_{20}\mathrm{Ca}_{20}$ but does not reproduce higher ones.

3.4 Spin-Orbit Coupling

In order to account for the correct nucleon numbers at which the higher shell closures occur, a spin-orbit term is introduced to the nuclear potential.

In the case of the *modified* harmonic oscillator:

$$V'_{\mathrm{HO}}(r) = -U_0 + \frac{1}{2}m\omega^2 r^2 - \frac{2}{\hbar^2}\alpha\underline{\ell}.\underline{s} \qquad (56)$$

Since

$$\underline{\ell}.\underline{s} = \frac{\hbar^2}{2}\left[j(j+1) - \ell(\ell+1) - \frac{3}{4}\right] \qquad (57)$$

then the energy is modified by an additional term:

$$-\alpha\ell \quad \text{if} \quad j = \ell + \frac{1}{2} \qquad (58)$$

$$+\alpha(\ell+1) \quad \text{if} \quad j = \ell - \frac{1}{2} \qquad (59)$$

3.5 Woods-Saxon + Spin-Orbit

Usually *finite* potential forms are used so that $V(r) \to 0$ if $r \gg R$. The Woods-Saxon potential is considered to be the most realistic, see Fig. 15.

It has the following radial dependence:

$$V_{\mathrm{WS}}(r) = \frac{U_0}{t} + \frac{U_{\ell s}}{r_0^2}\frac{1}{r}\frac{d}{dr}\left(\frac{1}{t}\right)\underline{\ell}.\underline{s} \qquad (60)$$

where $t = 1 + \exp\left[(r-R_0)/a\right]$ and $R_0 = r_0 A^{\frac{1}{3}}$

Figure 15: Woods-Saxon potential

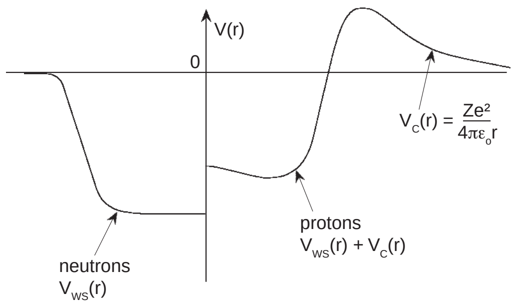

3.6 Residual Interaction

The residual interaction v between nucleons is the difference between the actual two-nucleon potential V_α experienced by a nucleon in a state α and the average potential. The matrix elements of v, $\langle\alpha|v|\beta\rangle$, are only appreciable near the Fermi surface. The interaction v is a *two-body operator* because it changes the state of two nucleons.

It could be treated in a number of ways

- from the free two-nucleon potential. DIFFICULT!
- treated as free parameters to be deduced from experimental data on energy levels and angular momenta of many nuclei.
- parameterised using physical intuition. The interaction depends on the radial separation $(\underline{r_i} - \underline{r_j})$ which can be expanded in a multipole expansion:

$$(\underline{r_i} - \underline{r_j}) = \sum v_\ell(r_i r_j) \sum_m Y_{\ell m}(\theta,\phi) Y^*_{\ell m}(\theta,\phi) \tag{61}$$

For example, if it is assumed that the interaction takes place near the Fermi surface, i.e. near $r = R$ then $v_\ell(r_i r_j) \to v_\ell(R)$.

In common use is the *quadrupole + pairing interaction*. Here it is assumed that $v_\ell(r_i r_j) = \chi r_i^\ell r_j^\ell$ so that:

$$(\underline{r_i} - \underline{r_j}) = \chi \sum_{\ell m} M_{\ell m}(i) M^*_{\ell m}(j) \tag{62}$$

$M_{\ell m}(i)$ is the *multipole operator* defined by:

$$M_{\ell m}(i) = r_i^{\ell} Y_{\ell m}(\theta_i \phi_i) \tag{63}$$

The *quadrupole-quadrupole* term (i.e. $\ell = 2$) is the most important correction to a spherical field, and is relatively long-range.

The *pairing interaction* is the important short-range component, see Fig. 16

Figure 16: Pairing interaction

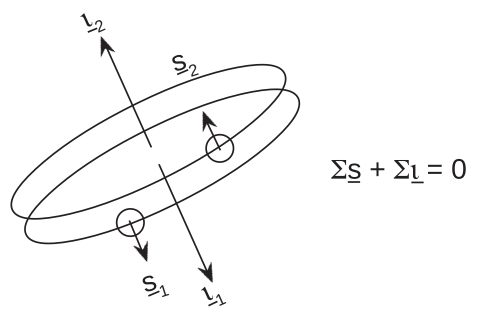

It leads to greater binding between the nucleons if their angular momenta are coupled to zero since in this state the nucleons have the maximum spacial overlap (note they that cannot have the same magnetic substate because of the Pauli principle).

This is achieved by using the approximation that:

$$\langle j^2 JM | v | j^2 J' M' \rangle = \delta_{JJ'} \delta_{MM'} \delta_{J0} \tag{64}$$

for nucleons in the same subshell (i.e. same j) i.e. the interaction only occurs in the $J = 0$ state.

3.7 Hartree Fock

The philosophy here is that the nuclear potential is *self consistent*. That is, we calculate the nucleon distribution (i.e. the nuclear density) from the net potential, and then evaluate the net potential from the nucleon-nucleon interaction. Then the potential is self-consistent if the one with which we end up with is the same as the one we start with.

The net potential is written as the sum of the two-body potentials:

$$U(\underline{r}_i) = \sum_j V(\underline{r}_i, \underline{r}_j) = \int \rho(\underline{r}') V(\underline{r}, \underline{r}') d\underline{r}' \tag{65}$$

where the summation over all interactions is replaced by an integral weighted by the nucleon density distribution $\rho(r)$.

The nucleon density distribution $\rho(r)$ is given by:

$$\rho(r) = \sum \psi^*(\underline{r})\psi(\underline{r}) \tag{66}$$

where ψ is the wavefunction of the particle at $\underline{r}$. The summation is over all individually occupied orbits. Thus the net (one-body) potential becomes:

$$U(\underline{r}) = \sum \int \psi^*(\underline{r})V(\underline{r},\underline{r}')\psi(\underline{r})d\underline{r}' \tag{67}$$

which is substituted into the one-body Schrödinger equation to solve for ψ, for all orbits. The procedure is to start with trial wavefunctions and then iterate until U (or ρ, or ψ) does not change.

4: Nuclear Deformation

The experimental observation of large electric quadrupole moments and low-lying rotational bands suggests that nuclei can be *deformed* in their ground state. The origin of deformation lies in the long range component of the nucleon-nucleon residual interaction (the quadrupole-quadrupole interaction) which gives additional binding energy to nuclei which lie between the closed shells if the nucleus is deformed. In contrast, the short range component (pairing interaction) prefers spherical shapes.

4.1 Geometric Descriptions

The general shape of a nucleus (see Fig. 17) can be expressed in terms of the spherical harmonics $Y_{\lambda\mu}(\theta,\phi)$:

$$R = R_0 \left[1 + \sum_{\lambda=0}^{\infty} \sum_{\mu=-\lambda}^{\lambda} a_{\lambda\mu} Y_{\lambda\mu}(\theta,\phi) \right] \tag{68}$$

Figure 17: Description of the nuclear shape

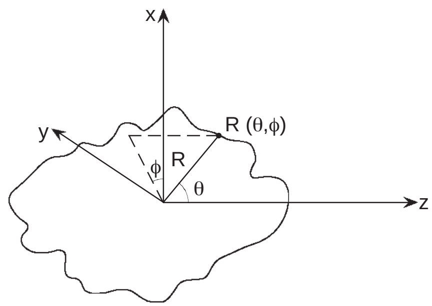

Figure 18: Nuclear deformations

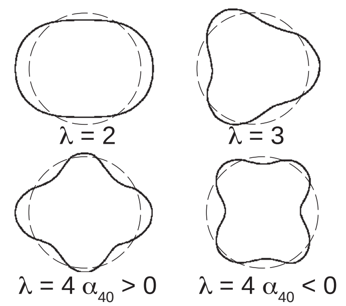

The $\lambda = 1$ term describes displacement of the mass centre and therefore cannot give rise to excitation of the nucleus – ignore this. The $\lambda = 2$ term is the most important, and describes *quadrupole* deformation.

The next higher order terms, $\lambda = 3, 4$, describe *octupole* and *hexadecapole* deformation, see Fig 18.

For quadrupole deformation, the equation reduces to:

$$R = R_0 \left[1 + \sum_{\mu=-2}^{2} a_{2\mu} Y_{2\mu}(\theta, \phi) \right] \qquad (69)$$

Figure 19: Principal axes

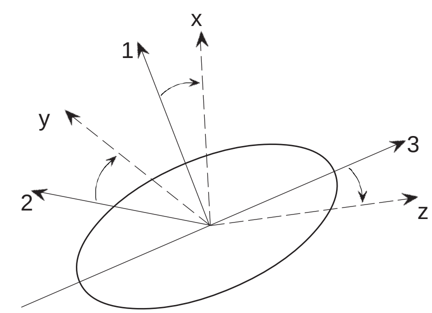

If the principal (i.e. x,y,z) axes are made to be coincident with the nuclear axes (1, 2, 3), see Fig. 19, then $a_{2\,1} = a_{2\,-1} = 0$ and $a_{2\,2} = a_{2\,-2}$

We define

$$a_{2\,0} = \beta\cos\gamma \tag{70}$$

$$a_{2\,2} = \frac{1}{\sqrt{2}}\beta\sin\gamma \tag{71}$$

so that

$$\delta R_K = R_K - R_0 = \sqrt{\frac{5}{4\pi}}R_0\beta\cos\left(\gamma - K\frac{2\pi}{3}\right) \tag{72}$$

If $\gamma = 0$ then $R_1 = R_2$ and $R_3 > R_0$, i.e. *prolate* spheroid. In this case we have:

$$\delta R_{1,2} = -\frac{1}{2}\sqrt{\frac{5}{4\pi}}R_0\beta$$

$$\delta R_3 = \sqrt{\frac{5}{4\pi}}R_0\beta \tag{73}$$

If $R_3 < R_0$ this describes an *oblate* spheroid

If $\gamma \neq n\pi/3$ where n is an integer then we have a *triaxial* shape with $R_1 \neq R_2 \neq R_3$

4.2 Theoretical Nuclear Deformations

Various calculated nuclear shapes are shown below from Möller and Nix (Los Alamos). The top row shows ground-state deformations. At the bottom left is a fission isomer trapped in a secondary energy minimum, whilea mass-asymmetric shape of a nucleus on the way to fission is shown to the bottom right.

Figure 20: Theoretical nuclear shapes

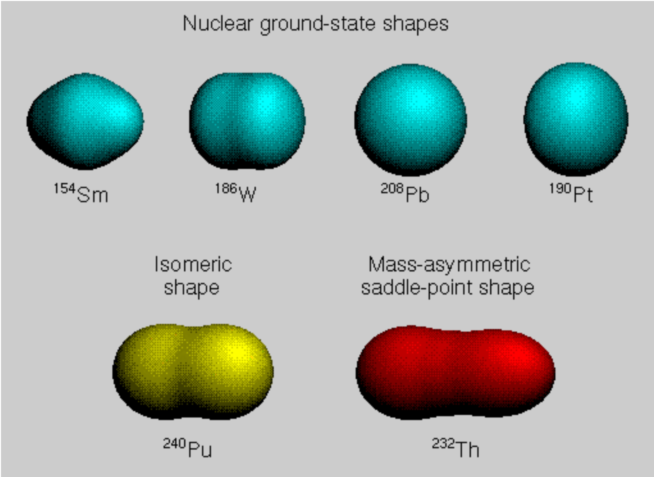

4.3 Ground-State Deformations

Theoretical ground-state quadrupole deformations are shown below, from Möller and Nix (Los Alamos). Note that low deformation occurs around the magic numbers and maximal deformation in midshell regions.

Figure 21: Deformation systematics

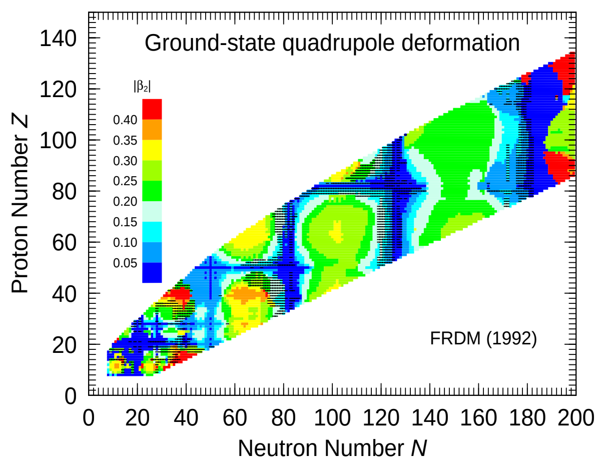

4.4 Nilsson Model

To introduce nuclear deformation Nilsson modified the the harmonic oscillator potential to become *anisotropic*:

$$V(r) = \frac{1}{2}m\left(\omega_1^2 x^2 + \omega_2^2 y^2 + \omega_3^2 z^2\right) \tag{74}$$

so that

$$\omega_K R_K = \omega_0 R_0 \tag{75}$$

If axial symmetry is assumed (i.e. $\gamma = 0$) then the deformation is described by ε where

$$\varepsilon = (\omega_{1,2} - \omega_3)/\omega_0 \tag{76}$$

Therefore, using Equations (73) and (75):

$$\begin{aligned} \varepsilon &= \left(\frac{\omega_0 R_0}{R_{1,2}} - \frac{\omega_0 R_0}{R_3}\right)/\omega_0 = \frac{(R_3 - R_{1,2})R_0}{R_{1,2}R_3} \\ &= \frac{(\delta R_3 - \delta R_{1,2})R_0}{R_0^2} = \frac{3}{2}\sqrt{\frac{5}{4\pi}}\beta \approx 0.95\ \beta \end{aligned} \tag{77}$$

so that $\varepsilon \approx \beta$.

In order to reproduce the observed nuclear behaviour the empirical potential energy term has to include two extra terms and becomes:

$$V(r) = \frac{1}{2}m\left(\omega_1^2 x^2 + \omega_2^2 y^2 + \omega_3^2 z^2\right) - C\underline{\ell}.\underline{s} - D\underline{\ell}^2 \tag{78}$$

The $C\underline{\ell}.\underline{s}$ term is the spin-orbit term introduced already to account for the observed nuclear shell structure. The $D\underline{\ell}^2$ term has the effect of flattening the potential well to make it look more like the actual nuclear shape. Without these additional terms the Nilsson energy levels are:

$$\hbar\omega_1\left(n_1+\frac{1}{2}\right) + \hbar\omega_2\left(n_2+\frac{1}{2}\right) + \hbar\omega_3\left(n_3+\frac{1}{2}\right)$$
$$= \left[\left(N+\frac{3}{2}\right) - \varepsilon\left(n_3 - \frac{N}{3}\right) + \frac{1}{9}\varepsilon^2\left(N+\frac{3}{2}\right)\right]\hbar\omega_0 \tag{79}$$

where $N = n_1 + n_2 + n_3$ is the oscillator quantum number (see Equation 54), and n_3 describes the z-axis component, etc. In addition to N and n_3 the quantum numbers $\ell_z = \Lambda$, $s_z = \Sigma = \pm\frac{1}{2}$ and $j_z = \Omega = \Lambda + \Sigma$ are also used. These are the projections of $\underline{\ell}$, $\underline{s}$ and $\underline{j}$ of a single nucleon on the nuclear z-axis. The *parity* is $(-1)^\ell$ and the labels of the energy levels in the Nilsson scheme: $\Omega^\pi[Nn_3\Lambda]$.

Figure 22: Nilsson diagram

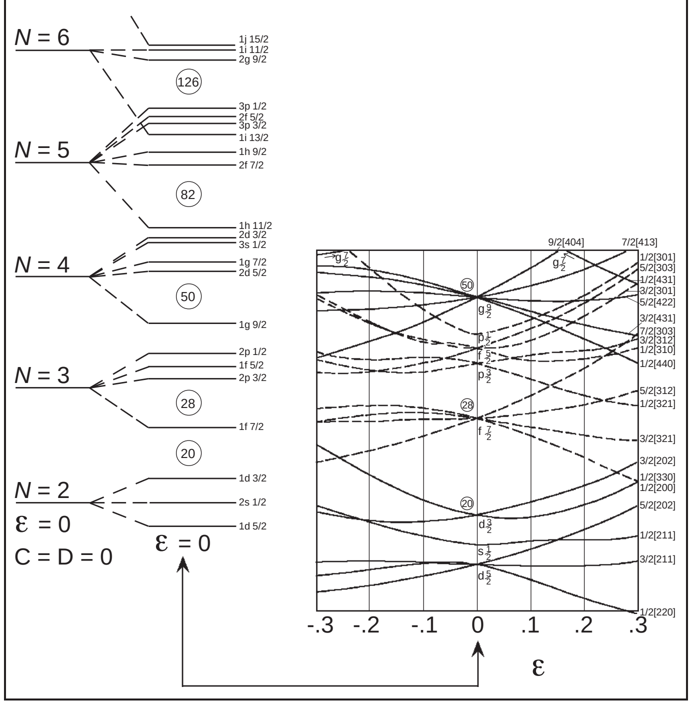

Note that many degeneracies are lifted for a deformed nucleus, i.e. $\varepsilon \neq 0$

Because of the additional $\underline{\ell}.\underline{s}$ and $\underline{\ell}^2$ terms the physical quantities labelled by n_3 and Λ are not constants of motion, only approximately so. They are called *asymptotic* quantum numbers as they become "good" only as $\varepsilon \to \infty$. The quantum numbers Ω, π and N are always good labels provided (i) the nucleus is not rotating, (ii) there are no residual interactions.

The following observations can be made from the Fig. 22:

- each *spherical* level, labelled by $(\ell)_j$ at $\varepsilon = 0$, is split into $(2j+1)/2$ levels, i.e.

$$\Omega = \pm\frac{1}{2},\ \pm\frac{3}{2},\ ...,\ \pm j \tag{80}$$

- the remaining $\pm\Omega$ degeneracy means that each *deformed* level can accommodate 2 neutrons or 2 protons.

- orbits with lower Ω are shifted downwards for $\varepsilon > 0$ (prolate), upwards for $\varepsilon < 0$ (oblate).

4.5 Large Deformations

If ε becomes large then the $\underline{\ell}.\underline{s}$ and $\underline{\ell}^2$ terms can be neglected relative to deformation effects and the energy levels are given by Equation 79 (see Fig. 23).

Figure 23: Deformed shell gaps

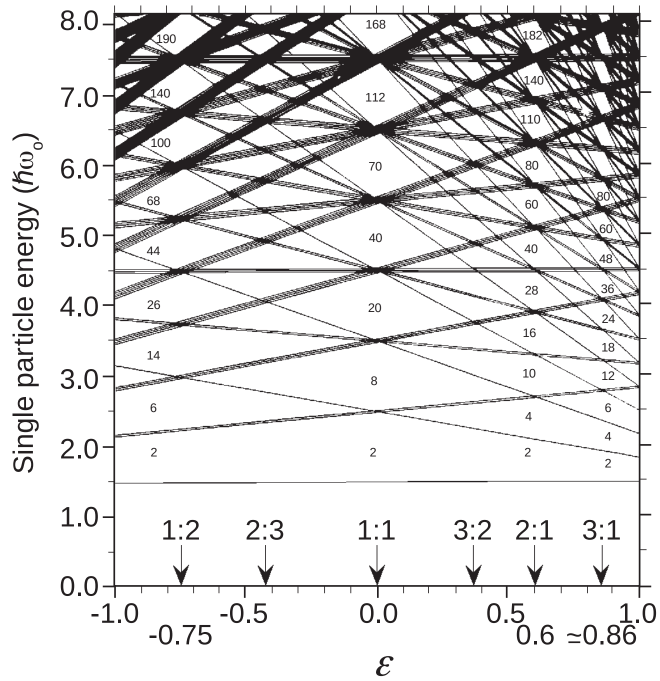

Fig. 23 shows that if ω_3 and $\omega_{1,2}$ are in the ratio of integers, i.e.

$$\omega_3/\omega_{1,2} = p/q \tag{81}$$

then large degeneracies become apparent and *deformed* shell effects emerge. This is the origin of *superdeformed* shapes which have favourable energies at a p/q ratio of $1/2$ (see Section 5.3).

This corresponds to a long-to-short axis ratio of

$$R_3 : R_{1,2} = 2:1 \quad \text{with} \quad \varepsilon \approx 0.60$$

Other favourable shapes occur at an axis ratio of 3:2 ($\varepsilon \approx 0.37$) and searches are currently being made for nuclei with a *hyperdeformed* shape:

$$R_3 : R_{1,2} = 3:1 \quad \text{with} \quad \varepsilon \approx 0.86$$

What next? *megadeformation*!

5: Hybrid Models

5.1 Deformed Liquid Drop

In the assumption that the nucleus behaves as a charged, liquid drop the semi-empirical expression can be obtained for the total nuclear energy:

$$\mathrm{E}(A, Z) = -a_V A + a_S A^{2/3} + a_C Z^2 A^{-1/3} \tag{82}$$

where a_V, a_S, and a_C are the coefficients of the volume, surface and Coulomb energies, respectively. To correct for deformation the nuclear radius R_0 is replaced by:

$$\begin{aligned} R_3 &= R_0(1+\delta) \\ R_{1,2} &= R_0\left(1 - \frac{1}{2}\delta\right) \end{aligned} \tag{83}$$

where

$$\delta = \sqrt{\frac{5}{4\pi}}\beta = \frac{2}{3}\varepsilon \tag{84}$$

(see Equation 77).

It can be shown that the above expression for the energy becomes (for small values of δ):

$$\mathrm{E}(\delta, A, Z) = -a_V A + a_S A^{2/3}\left(1 + \frac{2}{5}\delta^2\right) + a_C Z^2 A^{-1/3}\left(1 - \frac{1}{5}\delta^2\right) \qquad (85)$$

Figure 24: Deformed–spherical energies

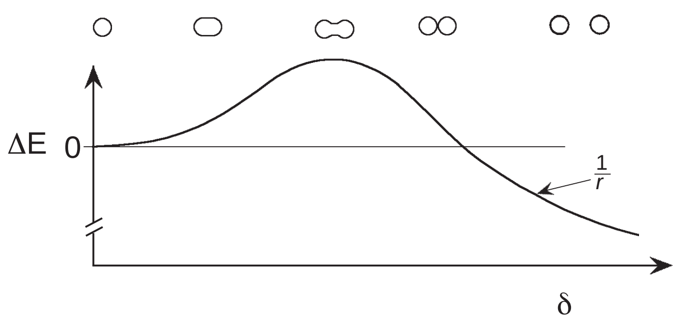

A plot of $\Delta\mathrm{E}(\delta) = \mathrm{E}(\delta) - \mathrm{E}(\delta = 0)$ is shown in Fig. 24. This predicts that the nucleus is always spherical (i.e. $\Delta\mathrm{E} > 0$ for $\delta > 0$) unless $Z^2/A > 49$ in which case the nucleus prefers infinite deformation (i.e. it fissions).

This is clearly wrong!

5.2 Shell Correction - Strutinsky Method

The liquid drop model can be extended to take into account *shell-model* effects, i.e. effects which arise from the individual nucleon motion. Additional terms arising from the symmetry energy (which prefers $Z = N$) and the pairing energy (Δ, 0, $-\Delta$ for even-even, odd-even and odd-odd nuclei) can be added to the above expression. Alternatively the total energy can be calculated using mean field potentials, either self consistently (the Hartree Fock method) or using empirical potentials such as Nilsson and Woods-Saxon. This is *not* the sum of the individual eigenvalues e_i because the potential energy of each nucleon would be counted twice. The eigenvalue for each nucleon is:

$$e_i = \langle T_i \rangle + \langle \sum_{j \neq i} V_{ij} \rangle \qquad (86)$$

and the total energy E is:

$$\sum \langle T_i \rangle + \langle \frac{1}{2} \sum_{i,j \neq i} V_{ij} \rangle = \frac{1}{2}\sum e_i + \frac{1}{2}\sum \langle T_i \rangle \qquad (87)$$

For particles moving in the harmonic oscillator potential it can be shown that:

$$\langle T_i \rangle = \langle V_i \rangle = \sum_{i,j \neq i} V_{ij} \tag{88}$$

so that:

$$E = \frac{3}{4} \sum e_i \tag{89}$$

This method has difficulty in producing the correct energy because errors in the individual values of e_i give large errors in the summation. To obtain both the global (liquid drop) and local (shell-model) variations with δ, Z and A more accurately, Strutinsky developed a method to combine the best properties of both models. He achieved this by considering the behaviour of the *level density*, $\rho(e)$ (e is the nucleon energy) in the two models.

Fig. 25 shows the level densities at the Fermi surface $\rho_{\mathrm{F}}(e)$ without and with single particle effects.

Figure 25: Level densities at the Fermi surface

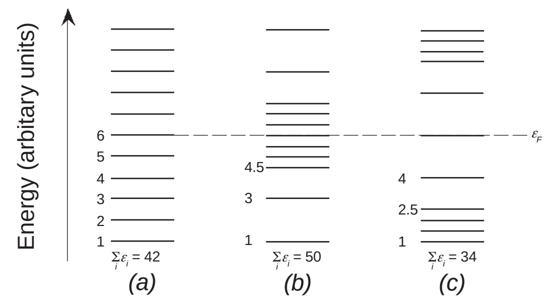

If there are no single particle effects (Fig. 25(a)) then the spacing of the energy levels is uniform and $\rho_{\mathrm{F}}(e) = \rho_{AV}(e)$, the average value. This is the **liquid drop prediction**. In Figs. 25(b) and (c) the level densities are non-uniform because of single particle effects.

The values of both $\rho_{\mathrm{AV}}(e)$ and $\rho_{\mathrm{F}}(e)$ can be calculated using (for example) the Nilsson model by averaging over a large (5–10 MeV) and small (1–2 MeV) energy interval respectively. A change in nuclear binding will arise from the value of $\rho_{\mathrm{AV}}(e) - \rho_{\mathrm{F}}(e)$ — negative in Fig. 25(b) and positive in Fig. 25(c). The calculated *fluctuating* energy correction is then added to the liquid drop energy.

Figure 26: Shell-correction energies

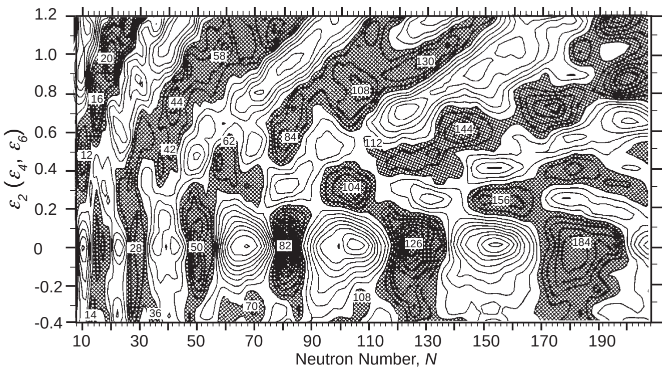

Fig. 26 shows the variation of the shell correction energy with δ and N in the form of a contour plot.

The spherical shell gaps 20, 28, 50, 82, 126 and 184 can be seen for $\varepsilon = 0$, but in general the minimum in energy will occur for non-zero values of ϵ. In addition, there are *deformed* shell gaps which occur at 16, 44, 84, 112 and 144 for $\varepsilon = 0.6$. The single particle model used to calculate the fluctuating correction is more sophisticated than that used in Section 4.5 and the *superdeformed* shell gaps lie closer to those observed experimentally.

5.3 Fission Isomers

If the increase in liquid drop energy for increasing deformation, $\Delta E(\delta)$, is small enough (e.g. $Z^2/A > 35$) then any secondary minimum in the total energy arising from the shell correction will become similar in energy to the first minimum.

Fig. 27 shows the variation in total nuclear energy with deformation for the nucleus ^{240}Pu. For this nucleus two minima in the energy are seen, both occuring for non-zero deformations.

Figure 27: Potential energy versus deformation

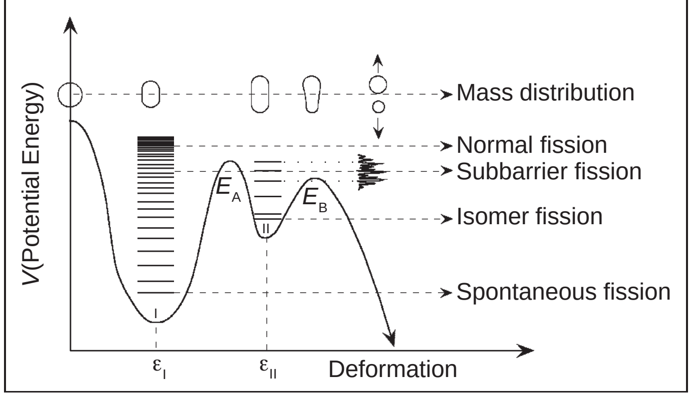

The 'second' minimum, which corresponds to a superdeformed nuclear state, can decay by penetration through the outer barrier to fission rather than by penetrating the inner barrier to the ground state. The first and second minimum states are said to *coexist*, i.e. the nucleus can exist in either state, each having very different deformation to each other.

The fission lifetime for the second minimum is much shorter than for the first minimum but is much longer than the lifetime of excited states built upon it. For this reason it is called a *fission isomer* where 'isomeric' means long-lived.

Evidence for the large deformation of the second minimum has come from direct measurement of its electric quadrupole moment.

The electric multipole moments are given by:

$$\mathcal{M}_\lambda = \sum_{k=1}^{Z} r_k^\lambda Y_{\lambda 0}(\theta_k) \tag{90}$$

where (r_k, θ_k, ϕ_k) are the co-ordinates of the k^{th} proton and $Y_{\lambda 0}$ is a spherical harmonic of order λ.

The electric quadrupole moment is:

$$\mathcal{M}_2 = \sum_{k=1}^{Z} r_k^2 Y_{20}(\theta_k) = \sqrt{\frac{5}{16\pi}} \sum r_k^2 \left(3\cos^2\theta_k - 1\right)$$
$$= \sqrt{\frac{5}{16\pi}} \sum \left(3z_k^2 - r_k^2\right) \tag{91}$$

since $\cos\theta = z/r$.

For a nuclear shape having quadrupole *mass* deformation, we assume that the protons are uniformly distributed throughout the nucleus. Equation 91 is integrated over the spheroidal shape of the nucleus, giving

$$\mathcal{M}_2 = \frac{1}{\sqrt{20\pi}} Z\left(R_3^2 - R_{1,2}^2\right) \approx \frac{3}{4\pi} Z R_0^2 \beta \tag{92}$$

By convention, we define the *intrinsic quadrupole moment*, Q_0, as:

$$Q_0 = \sqrt{\frac{16\pi}{5}}\mathcal{M}_2 = \frac{3}{\sqrt{5\pi}}ZR_0^2\beta = \frac{6}{5}ZR_0^2\delta \qquad (93)$$

The measurement of Q_0 can be achieved in a number of ways. For example it is directly related to the probability of the emission of a photon in the decay of an excited nuclear state within a *rotational band* which is characteristic of the deformed structure. From this measurement the nuclear deformation β can be extracted.

6: Nuclear Excitation

6.1 Spherical Nuclei

Figure 28: Level schemes: even-even nuclei

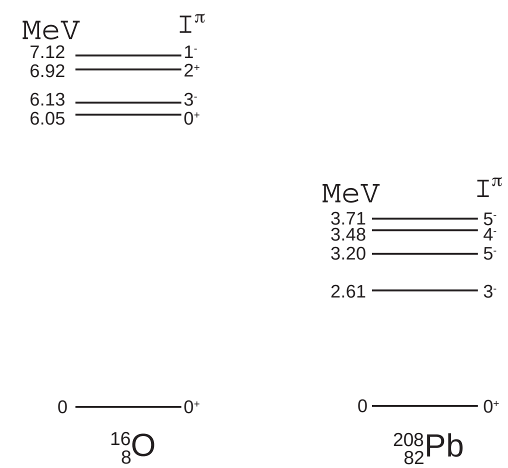

Fig. 28 shows the energy levels of two nuclei, ^{16}O and ^{208}Pb. Note that in common with *all even-even nuclei* their ground states have angular momentum I and parity π of 0^+, a consequence of nuclear pairing.

These particular nuclei, in common with *all closed shell nuclei* are spherical in their ground state so that excitations can only occur by breaking pairs of nucleons or by vibrations. The energy difference between the ground state and the lowest excited states is a rough measure of the pairing energy. For odd mass nuclei which are one nucleon added or removed to the closed shell, the low-lying energy levels (Fig. 29) represent the single particle excitation in either direction from the Fermi surface.

Figure 29: Level schemes: odd-A nuclei

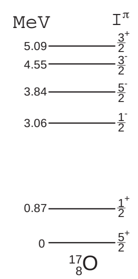

The *configuration* of the low-lying levels are written as $(\pi(\ell)_j)^n I^\pi$ (odd-Z) or $(\nu(\ell)_j)^n I^\pi$ (odd-N), e.g.: ^{17}O is $(\nu(\ell)_j)^1 I^\pi$ for a closed shell + one neutron, ^{207}Tl is $(\pi(\ell)_j)^{-1} I^\pi$ for closed shell + 1 proton hole.

In this case the total angular momentum I of the nucleus equals the angular momentum of the odd particle j. Higher excitations can occur by breaking pairs of nucleons e.g. $(\nu \mathrm{p}_{\frac{3}{2}})^{-1}(\nu \mathrm{d}_{\frac{5}{2}})^2 \; \frac{3}{2}^-$ for the 4.55 MeV level in ^{17}O would be a 1-hole 2-particle state.

6.2 Vibrations

From the liquid drop dependence on deformation (see Equation 85) we can estimate the restoring force if the nucleus is deformed from its equilibrium shape along the symmetry (z-)axis:

$$\begin{aligned} F &= -\frac{d\mathrm{E}}{dR_3} = -\frac{d\mathrm{E}}{d\delta}\frac{d\delta}{dR_3} = -\frac{d\mathrm{E}}{d\delta}\frac{1}{R_0} \\ &= -\left(\frac{4}{5}a_S A^{2/3} - \frac{2}{5}a_C Z^2 A^{-1/3}\right)\frac{\delta}{R_0} \end{aligned} \tag{94}$$

The vibration can be any distortion in the nuclear shape since (see Equations 68 and 83):

$$\delta \propto \frac{R - R_0}{R_0} = \sum_\lambda \sum_\mu a_{\lambda\mu} Y_{\lambda\mu}(\theta, \phi) \tag{95}$$

At low energy the most important are oscillations in

- a_{20} (β-vibrations – oscillations along the symmetry axis)
- a_{22} (γ-vibrations – oscillations perpendicular to the symmetry axis)
- a_{30} (octupole vibrations)

Figure 30: Nuclear vibrations

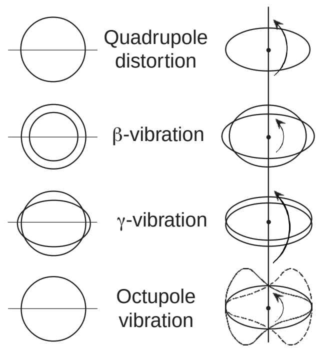

The energy levels of the vibrating system are those of the 1-D harmonic oscillator and are:
0, $\hbar\omega$, $2\hbar\omega$, ...
These correspond to excitations of 0, 1, 2 ... *phonons*.

For a given mode of vibration, each phonon has an associated angular momentum and parity: quadrupole phonons have 2^+ and octupole phonons have 3^-. For a pure vibrator the energy levels corresponding to the ways the n phonons are combined have the same energy $n\hbar\omega$; for real nuclei this degeneracy is removed, see Fig. 31.

Figure 31: Realistic vibrational levels

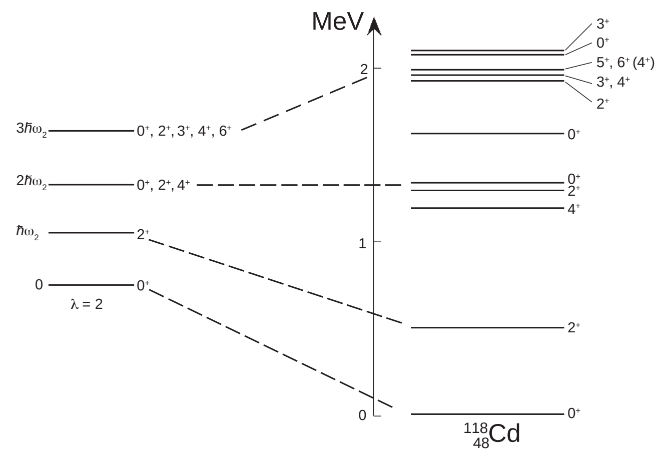

Note that the γ-vibration can only occur for a deformed system.

6.3 Rotations of a Deformed System

Examination of the low-lying energy levels of *deformed* even-even nuclei which lie far from closed shells reveal a regular sequence of levels whose energy is much lower than the pairing energy. This arises from nuclear *rotation*. The Hamiltonian corresponding to the rotation of the deformed system is:

$$H_{\rm rot} = \frac{\hbar^2}{2\mathcal{J}}\underline{R}^2 = \frac{\hbar^2}{2\mathcal{J}}(\underline{I} - \underline{J})^2 \qquad (96)$$

where $\mathcal{J}$ is the moment of inertia, $\underline{R}$ is the rotational angular momentum and $\underline{J}$ is additional angular momentum generated by for example, the odd particle in an odd-A nucleus, or by vibrations. All angular momenta are in units of $\hbar$. For an even-even nucleus with no vibrations $\underline{J} = 0$ and $\underline{I} = \underline{R}$. Fig. 32 shows how these angular momentum vectors are oriented in space.

Figure 32: Nuclear angular-momentum vectors

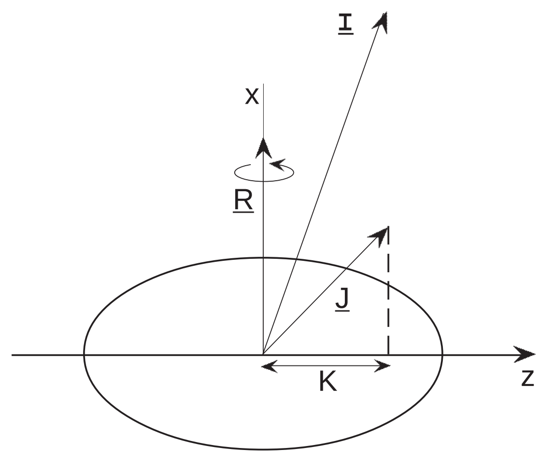

Note that for an axially-symmetric system rotation cannot occur around the symmetry (z-)axis so $\underline{R}$ is along the x- or y-axis. These are equivalent and the x-axis is usually selected.

The rotational Hamiltonian can be expanded:

$$\begin{aligned} \underline{R}^2 &= (\underline{I} - \underline{J})^2 = \underline{I}^2 - 2\underline{I}.\underline{J} + \underline{J}^2 \\ &= \underline{I}^2 + \underline{J}^2 - 2K^2 - (I_+J_- + I_-J_+) \end{aligned} \qquad (97)$$

where $I_\pm = I_x \pm iI_y$, $J_\pm = J_x \pm iJ_y$ and $J_z = I_z = \pm K$.

The quantity K is the projection of I along the symmetry axis. ($R_z = 0$ as already discussed). The coupling term $(I_+J_- + I_-J_+)$ corresponds to the Coriolis force and couples $\underline{J}$ to $\underline{R}$. The operators $I_\pm$ can however only link states with K differing by ± 1. This *Coriolis coupling* term can be ignored provided:

- rotational bands with $\Delta K = 1$, corresponding to different intrinsic excitation, lie far apart in energy;
- the band does not have $K = \pm\frac{1}{2}$

Neglecting the coupling term gives the following expression for the excitation energies:

$$E_{\rm rot} = \frac{\hbar^2}{2\mathcal{J}}\left[I(I+1) + J(J+1) - 2K^2\right]$$
$$I = K, K+1, K+2, \ldots \qquad (98)$$

In the absence of the Coriolis effects K is a constant of motion; since J is also constant then

$$E_{\rm rot} = E_K + \frac{\hbar^2}{2\mathcal{J}}I(I+1), \; I = K, K+1, K+2, \ldots \quad (99)$$

where E_K is the energy of the lowest member of the rotational band having $I = K$, the *bandhead*.

6.4 Examples

The low lying energy levels of three nuclei illustrate rotational structure.

6.4.1 ^{232}Th

Figure 33: ^{232}Th level scheme

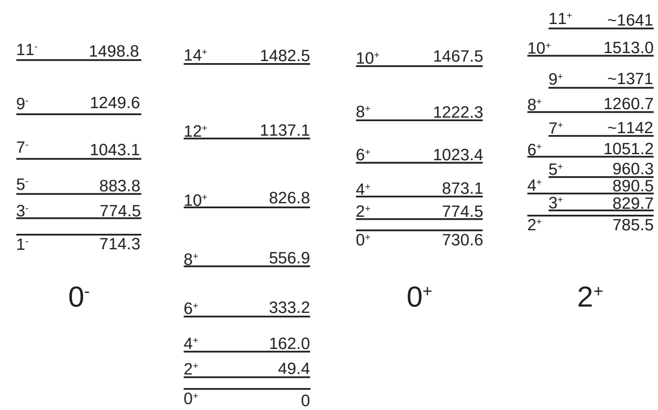

Here the low-lying excitations are all collective (i.e. rotational and vibrational).

The following rotational bands can be seen in Fig. 33:

Ground state band.
$K^\pi = 0^+, \quad I^\pi = 0^+, 2^+, 4^+, 6^+, ...$

β-band. Here $J^\pi = 2^+$, $K^\pi = 0^+$ so
$I^\pi = 0^+, 2^+, 4^+, 6^+, ...$

γ-band. Here $J^\pi = 2^+$, $K^\pi = 2^+$ so
$I^\pi = 2^+, 3^+, 4^+, 5^+, 6^+ ...$

Octupole band. Here $J^\pi = 3^-$, $K^\pi = 0^-, 1^-, 2^-$ or 3^-. The lowest energy band has
$K^\pi = 0^-, \quad I^\pi = 1^-, 3^-, 5^-, 7^-$

Note that if $K^\pi = 0^+$ then the I values 1, 3, 5,... are not present. Similarly the I values 0, 2, 4,... disappear if $K^\pi = 0^-$. This is a consequence of the nuclear wavefunction being identical under a rotation of 180° (reflection symmetry about the plane containing the x, y axes). This is the case for ^{232}Th which has no *octupole deformation*, i.e. $\beta_3 = 0$.

6.4.2 ^{224}Ra

Figure 34: ^{224}Ra level scheme

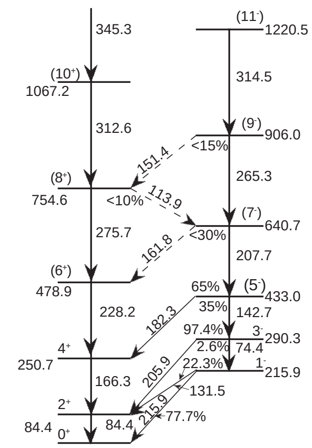

This nucleus is reflection asymmetric (i.e. $\beta_3 \neq 0$) in its ground state: we say it has *octupole deformation*. The nuclear wavefunction in its 'intrinsic' frame is not an eigenfunction of parity ($\psi^2(x, y, z) \neq \psi^2(-x, -y, -z)$). In the laboratory frame (i.e. averaged over all nuclear orientations) the levels have *alternating parity*

$K^\pi = 0^+, \quad I^\pi = 0^+, 1^-, 2^+, 3^-, 4^+, 5^-, 6^+, ...$

6.4.3 $^{153}_{69}$Tm

Figure 35: ^{153}Tm level scheme

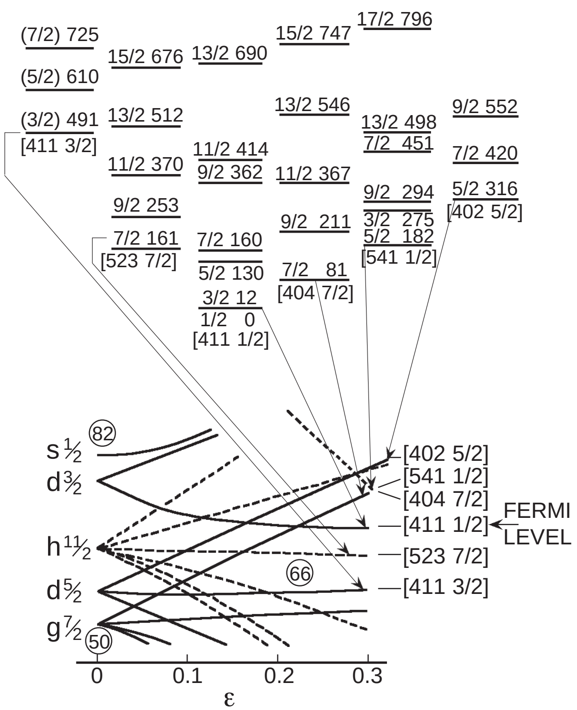

The low-lying excitations are rotational bands built upon single proton excitations, so that $K = j_z = \Omega$.

7: Rotating Systems

7.1 Moment of Inertia

The purely geometric model described earlier assumes a given nuclear shape such as a deformed liquid drop. Two questions arise:

- What is the moment of inertia of the nucleus?
- What is the effect of rotations on individual nucleons?

Inglis showed in 1952 that for a Fermi gas of nucleons the moment of inertia $\mathcal{J}$ around the x-axis is given by:

$$\mathcal{J}_x = 2 \sum \frac{|\langle p|\hat{I}_x|h\rangle|^2}{\epsilon_p - \epsilon_h} \qquad (100)$$

where the summation is over all possible 1-particle 1-hole excitations (see Fig. 36) in a deformed shell model (DSM) potential such as the Nilsson potential.

Figure 36: Particle and hole levels

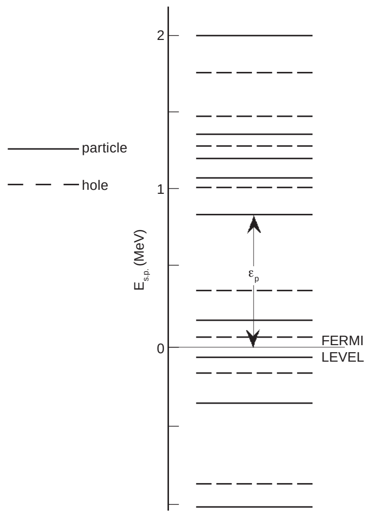

The quantities ϵ_p and ϵ_h are the energies of single particle and single hole states respectively. The operator $\hat{I}_x$ is the angular momentum operator about the x-axis.

If, for example, the single particle Nilsson model is used to calculate $\mathcal{J}$ using this expression, it gives comparable values to the **rigid-body** value for the moment-of-inertia of a deformed liquid drop:

$$\mathcal{J}_x = \frac{2}{5} m_{\mathrm{u}} A R_0^2 \left[1 + \frac{1}{2}\sqrt{\frac{5}{4\pi}}\beta \right] \qquad (101)$$

where m_{u} is the nucleon mass and R_0 is the nuclear radius. These are much higher than the experimental values, see Fig. 37

Figure 37: Nuclear moments of inertia

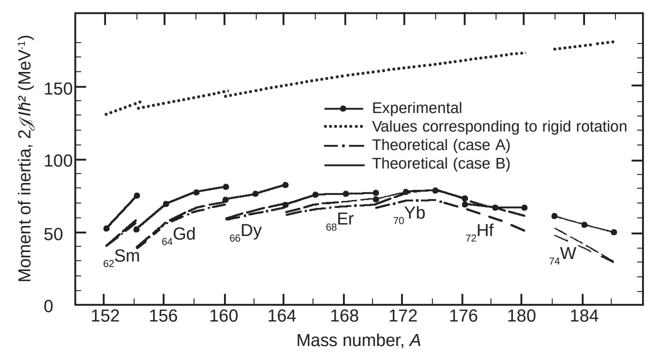

The discrepancy lies in the residual interactions, particularly the **pairing term**, which is ignored in the simple deformed potential model. We have seen that intrinsic excitation can only occur in even-even nuclei by breaking pairs of nucleons, so the energy level diagram becomes:

Figure 38: Effect of pairing

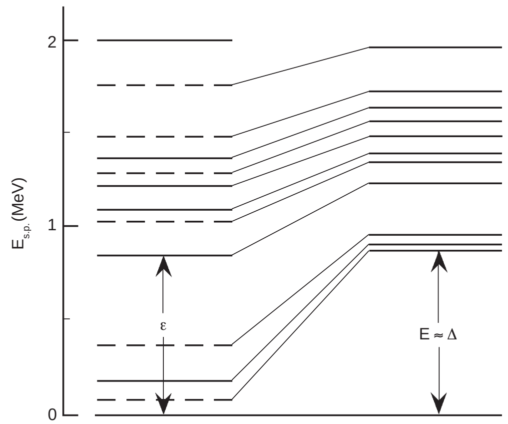

A rough estimate of the energy required to create a particle-hole excitation is 2Δ, where Δ is the pairing gap. Since the denominator in the formula for $\mathcal{J}$ (see Equation 100) depends on $(\epsilon_p - \epsilon_h)$, and $(\epsilon_p - \epsilon_h) \approx 2\Delta \approx 2$ MeV for mass 150 nuclei then $\mathcal{J}$ must be reduced because of pairing.

7.2 Cranking Model

The Deformed Shell Model (e.g. Nilsson Model) can be modified to take into account **pairing**. To include **rotational effects** it is convenient to subtract the effects of rotational forces (Coriolis and centripetal) which occur when the nucleus rotates with frequency ω about the x-axis. Classically, the 'potential' energy of these forces is $\underline{\omega}.\underline{I}$ so that the corresponding quantum operator is $\omega\hat{I}_x$ where $\hat{I}_x$ is the operator corresponding to the component of $\underline{I}$ along the rotation axis. The Hamiltonian becomes:

$$H^\omega = H_{\mathrm{DSM}} - \omega\hat{I}_x \tag{102}$$

which is the energy in the rotating frame - called the **Routhian**. The energy of the system in this frame is

$$E^\omega = E - \omega\langle\hat{I}_x\rangle \tag{103}$$

where $\langle\hat{I}_x\rangle$ is the expectation value of $\hat{I}_x$. This is the average value of I_x and is called the **aligned angular momentum**.

Two important relationships, which arise because E is independent of ω and E^ω is independent of I, are:

$$\frac{dE^\omega}{d\omega} = -\langle \hat{I}_x \rangle \qquad (104)$$

and

$$\frac{dE}{dI} = \omega \frac{d\langle \hat{I}_x \rangle}{dI} \qquad (105)$$

Figure 39: Projections of the nuclear spin

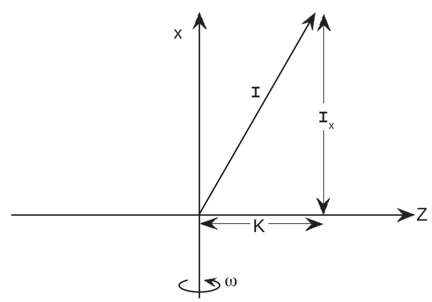

Since (see Fig. 39) $I_x^2 = I^2 - K^2$ we have

$$\langle \hat{I}_x \rangle = \sqrt{I(I+1) - K^2}\, \hbar \qquad (106)$$

If $K = 0$ then $\langle \hat{I}_x \rangle = \sqrt{I(I+1)}\, \hbar \approx I\hbar$ so that (using Equation 105):

$$\frac{dE}{dI} = \omega\hbar \qquad (107)$$

Using Equation 99, the energy of a rotational band for $K = 0$ is:

$$E = E_0 + \frac{\hbar^2}{2\mathcal{J}} I(I+1) \quad I = 0, 2, 4, \ldots \qquad (108)$$

so that

$$\frac{dE}{dI} = \frac{\hbar^2}{2\mathcal{J}}(2I+1) \qquad (109)$$

Since the energy of a transition ΔE between two consecutive states in a rotational band with angular momentum $I+1$ and $I-1$, respectively, is:

$$\Delta E = \frac{\hbar^2}{2\mathcal{J}}(\{I+1\}\{I+2\} - \{I-1\}I) = \frac{\hbar^2}{2\mathcal{J}}(4I+2) \qquad (110)$$

Thus, using Equation 109:

$$\Delta E = 2\frac{dE}{dI} \qquad (111)$$

and we therefore have the following relationship between ω and ΔE:

$$\omega\hbar = \Delta E/2 \qquad (112)$$

7.3 Backbending

Fig. 40 shows the behaviour of the moment of inertia $\mathcal{J}$ with ω^2 for two different nuclei ^{174}Hf and ^{158}Er.

Figure 40: Behaviour of moments of inertia

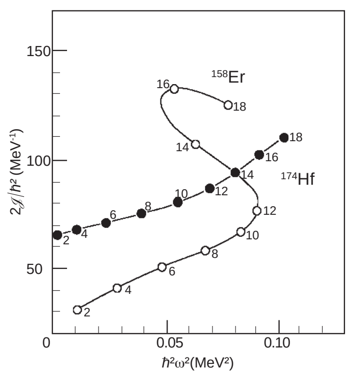

$\mathcal{J}$ is derived using Equation 110, and ω using Equation 112. Both exhibit the phenomenon that $\mathcal{J}$ increases as ω increases.

The case of ^{158}Er exhibits a more pronounced effect called backbending, so called from the characteristic '$\mathcal{S}$' shape of the plot.

This is the effect of two bands 'crossing', the ground state band (labelled 'g' in the figure) and a 'super'- or s-band (labelled 's'):

Figure 41: Crossing bands

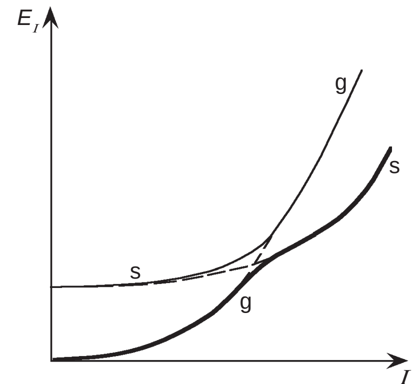

The states which are actually observed are the 'yrast' states (thick line in the figure) which have the lowest energy for a given value of I. The s-band arises from a breaking of a particular pair of nucleons ($i_{\frac{13}{2}}$ neutrons in the case of ^{158}Er) in the rotating core so that their angular momentum $\underline{j}_1$, $\underline{j}_2$ **aligns** with the rotation axis:

Figure 42: Pair breaking

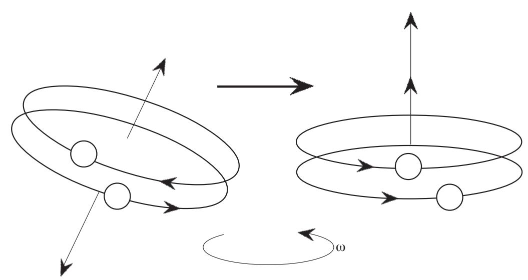

For the ground state band

$$E_g = \frac{\hbar^2}{2\mathcal{J}_g} I(I+1) \tag{113}$$

For the s-band (see Equation 96)

$$E_s = \frac{\hbar^2}{2\mathcal{J}_s} (\underline{I} - \underline{J})^2 + E_J \tag{114}$$

where $\underline{J} = \underline{j}_1 + \underline{j}_2$ and E_J is the energy required to break a pair of nucleons,

$$E_J \approx 2\Delta \approx 24\,.\,A^{-\frac{1}{2}} \text{ (MeV)} \tag{115}$$

The aligned angular momentum of the s-band increases by approximately $j_1 + j_2 - 1$ ($= 12\hbar$ for ^{158}Er).

Figure 43: Rotational alignment

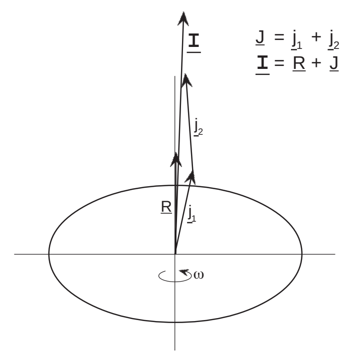

The two bands will cross when $E_g \approx E_s$, which occurs when $I \approx 12\hbar$. Equation 110 is not valid in the band crossing region but we can still use it to define an *effective* moment of inertia:

$$\mathcal{J}_{\text{eff}}/\hbar^2 = (2I+1)/\Delta E \approx I/\omega \tag{116}$$

The sharpness of the backbend depends on how strongly the bands 'interact' with each other, i.e. how much the wavefunctions of the states below the crossing in the ground state band overlap with the wavefunctions of the states above the crossing in the s-band. The bigger the overlap, the smoother the band crossing and the weaker the effect.

8: Nuclei at Extremes of Spin

As the nucleus is rotated to states of higher and higher angular momentum or *spin* I it tries to assume the configuration which has the lowest rotational energy (see Equation 96):

$$E_R = \frac{\hbar^2}{2\mathcal{J}} \underline{R}^2 \tag{117}$$

where $\underline{I} = \underline{R} + \underline{J}$ and J arises from the angular momenta of individual nucleons (or, less important in this context, from vibrations). This can be achieved by either reducing R or by increasing the moment of inertia $\mathcal{J}$, and the configuration chosen depends on the value of I and proton and neutron number of the nucleus. In either case the nuclear pairing is broken by the effect of rotations.

8.1 Generation of Angular Momentum

The two basic modes of nuclear spin generation are shown below.

Figure 44: Collective and noncollective spin

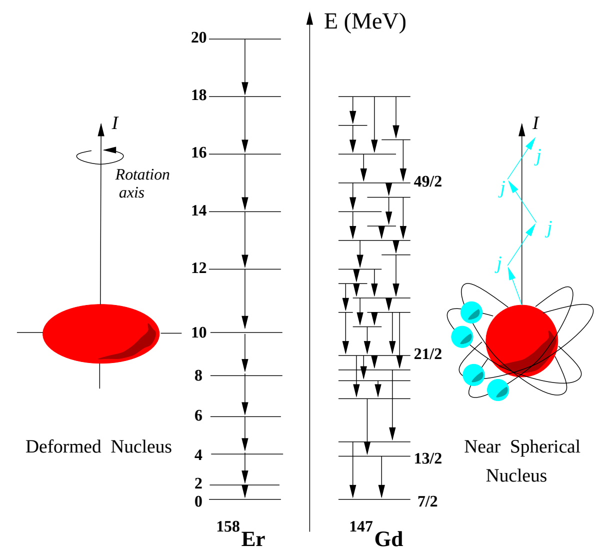

8.2 High I_x bands

We have seen how in nuclear backbending the value of R is reduced by breaking a single pair of nucleons and aligning their individual angular momentum with the x-axis, so that (see Figs. 42 and 43)

$$I_x = \sum j_x + R \tag{118}$$

is approximately a good quantum number; a given nuclear state is described by a *single* value of I_x.

The alignment of broken pairs with the rotation axis becomes easier if

- The particle angular momentum j is large and its projection on the z-axis (Ω) is small, e.g. the $\mathrm{i}_{\frac{13}{2}}$ neutron which has $\Omega = \frac{1}{2}$ or $\Omega = \frac{3}{2}$.
- the rotational **Coriolis** force is large. Since the energy associated with this is proportional to $\frac{\hbar^2}{2\mathcal{J}}$ then this occurs when $\mathcal{J}$ is small, i.e. the nuclear deformation is small.

We deduce that alignment effects should be prominent for nuclei which have a few nucleons outside the closed shell, such as ^{158}Er, which has 8 neutrons outside the closed neutron shell ($N = 82$).

Figure 45: Aligned particles: band termination

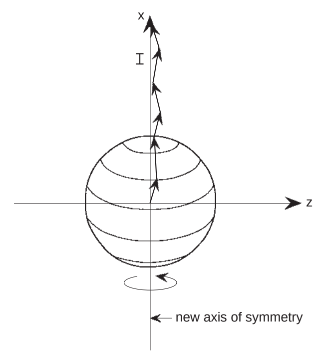

If we continue rotating the system to higher and higher values of ω then more and more pairs of nucleons will break and align their angular momenta with the rotation axis. Since the aligned particles move in equatorial orbits, this will eventually give rise to an **oblate** nucleus rotating around its axis of symmetry which is now the x-axis. The total angular momentum $\underline{I}$ would arise not from collective rotation of a prolate deformed core, but the sum of the individual $\underline{j}_i$, see Fig. 45.

Eventually we align all the n_p protons and n_n neutrons outside the closed shell so that

$$I = \sum_{i=1}^{n_\mathrm{p}} j_i(\mathrm{p}) + \sum_{i=1}^{n_\mathrm{n}} j_i(\mathrm{n}) \tag{119}$$

and the rotational band is said to *terminate*, see Fig. 46.

Figure 46: Band termination at 46^+ in ^{158}Er

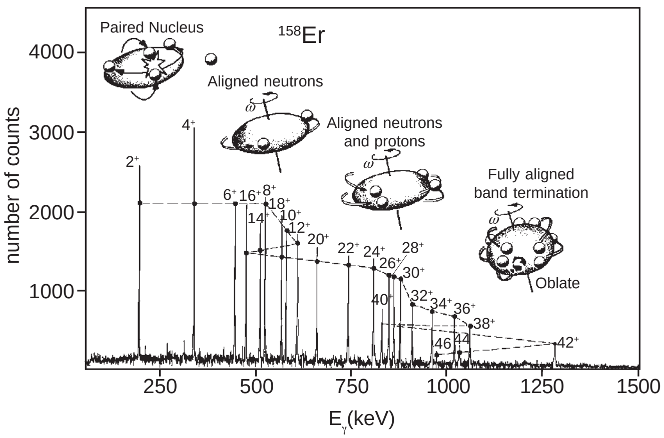

At termination, ^{158}Er can be considered as a spherical core ($^{146}_{64}\mathrm{Gd}_{82}$) plus twelve (4 protons and 8 neutrons) aligned valence particles which generate a maximum spin of 46^+ (see Table 3).

Table 3: Configuration of the 46^+ state in ^{158}Er

Subshell	j_i	$\sum j_i$
$\pi(h_{11/2})^4$	11/2, 9/2, 7/2, 5/2	$32/2^+$
$\nu(i_{13/2})^2$	13/2, 11/2	$24/2^+$
$\nu(h_{9/2})^3$	9/2, 7/2, 5/2	$21/2^-$
$\nu(f_{7/2})^3$	7/2, 5/2, 3/2	$15/2^-$
		$I^\pi = 46^+$

8.3 High K (I_z) bands

If we have many paired nucleons outside the closed shell in the ground state, then alignment with the x-axis as the nucleus rotates becomes difficult because the nucleons near the Fermi level have their spin vector lying closer to the direction of the z-axis than to the x-axis, i.e. Ω is no longer small (see Section 4.4).

Instead the nucleon angular momentum j continues to align with the symmetry (z-)axis so that:

$$K = I_z = \sum j_z = \sum \Omega_i \tag{120}$$

is a good quantum number, see Fig. 47.

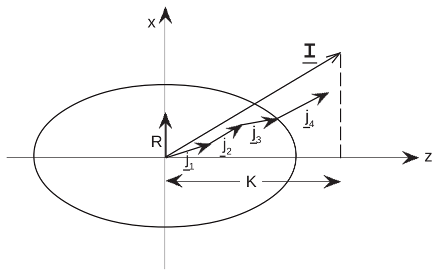

Figure 47: The K quantum number

Again J is increased by breaking nucleon pairs so that R is reduced. Fig. 48 shows the case of $^{172}_{72}\mathrm{Hf}_{100}$ where several high K bandheads can be seen.

Figure 48: High-K bands in ^{172}Hf

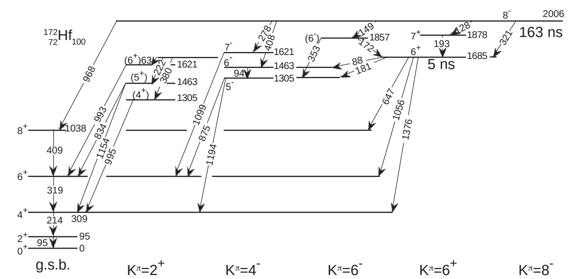

For example, the $K^\pi = 8^-$ band head is formed by the breaking of a pair of protons so that they occupy the Nilsson 'configurations'

$$\Omega[Nn_3\Lambda] = \frac{7}{2}[404] \text{ and } \frac{9}{2}[514] \tag{121}$$

In this case

$$K = \frac{7}{2} + \frac{9}{2} = 8 \tag{122}$$

and

$$\pi = (-1)^{N(1)}.(-1)^{N(2)} = (-1)^4.(-1)^5 = -1 \tag{123}$$

It is difficult for these rotational bands with high K values to decay to bands with smaller K since the nucleus has to change its angular momentum orientation. The bandhead can become **isomeric**.

For example the $K^\pi = 8^-$ bandhead is isomeric and which tries to decay to the $K^\pi = 0^+$ ground state band by γ-emission.

The decay to the $K^\pi = 6^+$ band requires the emission of an improbable $M2$ transition). The lifetime ($\tau = 163$ ns) of the bandhead is much longer than those of the rotational states built upon it.

8.4 Superdeformation

We have already seen in Section 4.5 that shell effects can give large energy corrections for large values of prolate deformation, e.g when the major/minor axis ratio is 2:1. Since the smooth liquid drop contribution to the total nuclear energy now includes the rotational energy, this can be substantially reduced at high spin by increasing the value of the moment of inertia, $\mathcal{J}$, see Equation 101. At sufficiently high angular momentum ($I \approx 60\hbar$ for mass 150 nuclei) the *superdeformed* second minimum can become energetically favourable, see Fig. 49

Figure 49: Superdeformed second minimum

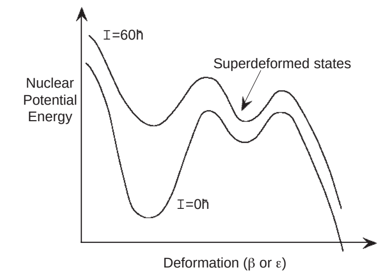

For such nuclei the rotational forces play the same role as the Coulomb forces for heavy nuclei in lowering the energy of the second minimum relative to the first minimum (see Section 5.3).

The experimental signature of these **superdeformed** shapes is a very regular sequence of γ-rays whose energies are given by Equation 110. Fig. 50 shows such a γ-ray spectrum for $^{152}_{66}\mathrm{Dy}_{86}$. The superdeformed band spans a spin range $26 - 60\hbar$.

Figure 50: Superdeformed band in ^{152}Dy

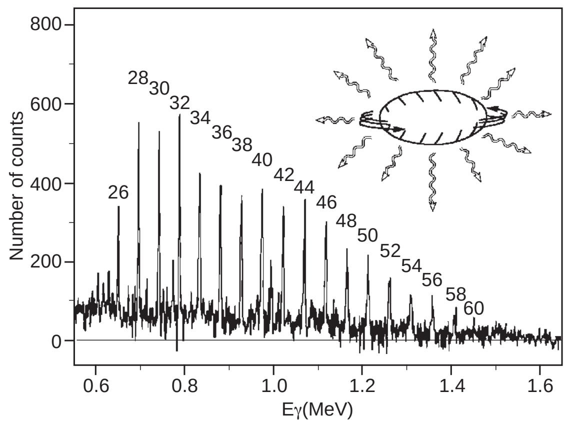

8.5 Shape Coexistence

For any given nuclear system at a given value of angular momentum, a number of configurations may exist, but only one is energetically favourable. We can regard the configurations as **co-existing**. Instead of a smooth (classical) transition from one shape to another we say that there are minima in the total nuclear potential energy corresponding to each shape.

At some critical value of angular momentum, the shape having the lowest energy changes.

A typical example is $^{152}_{66}$Dy$_{86}$ which has the following coexisting structures:

1. prolate normal deformed (*collective*)
2. prolate superdeformed (*collective*)
3. oblate aligned (*non-collective*)

The last one is energetically favourable at low spin and represents the ground state of ^{152}Dy (see Fig. 51).

As we move to the middle of both proton and neutron shells, the prolate normal deformed shape eventually becomes lowest in energy for the ground state, and the superdeformed shapes become less and less favourable even at very high spin.

Figure 51: Shape coexistence in ^{152}Dy

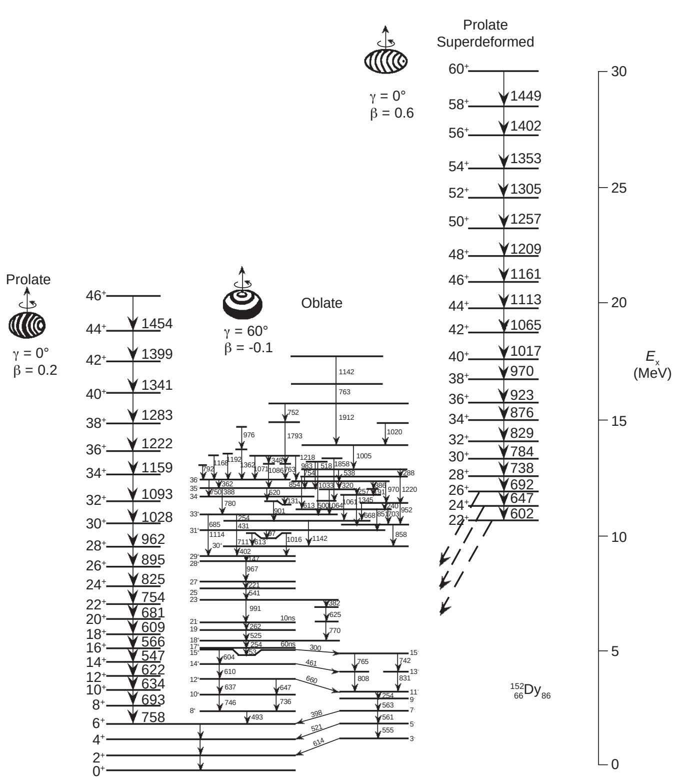

8.6 Extremely High Spin: Jacobi Instabilities

Jacobi (1834) realised that at a certain critical angular momentum, the stable equilibrium shape of a gravitating mass rotating synchronously (i.e. with all mass elements sharing a common angular velocity) changes abruptly from a slightly *oblate* spheroid to a *triaxial ellipsoid* rotating about its shortest axis.

Beringer and Knox (1961) suggested that a similar phenomenon might occur in the case of atomic nuclei idealised as *charged incompressible liquid drops* endowed with a *surface tension*.

The critical angular momentum at which the *Jacobi* transition takes place is:

$$L_1 = 0.06029 A^{7/6} \sqrt{40.83 - \zeta}, \qquad (124)$$

where the fissility ζ is defined:

$$\zeta = \frac{Z^2}{A\left[1 - 1.7826\left(\frac{A-2Z}{A}\right)^2\right]}. \qquad (125)$$

The angular momentum at which the fission barrier vanishes is:

$$L_2 = 0.09108 A^{7/6} \sqrt{36.34 - \zeta}. \qquad (126)$$

The region between L_1 and L_2 in the following figure is where the triaxial Jacobi configurations are predicted to exist. Note that the heavier nuclei fission before the Jacobi transition is reached.

Figure 52: Critical angular momenta

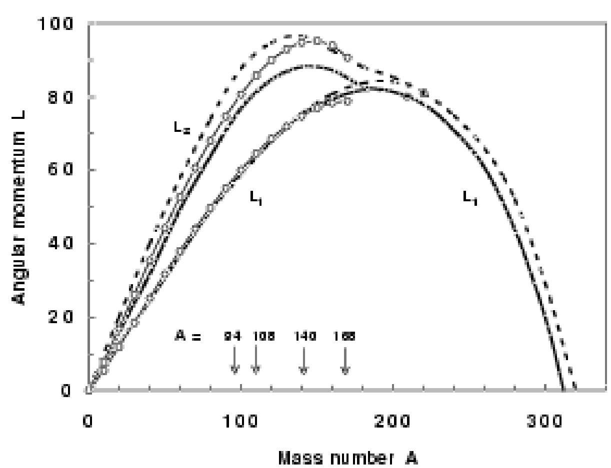

This figure shows the predicted γ-ray energies in a rotational band as a function of spin. A *giant backbend* in the γ-ray energies occurs at the Jacobi transition — the originally increasing γ-ray energies suddenly begin to decrease. This is the regime of Jacobi shapes, associated with rapidly increasing moments of inertia.

Figure 53: Calculated signal of the Jacobi transition

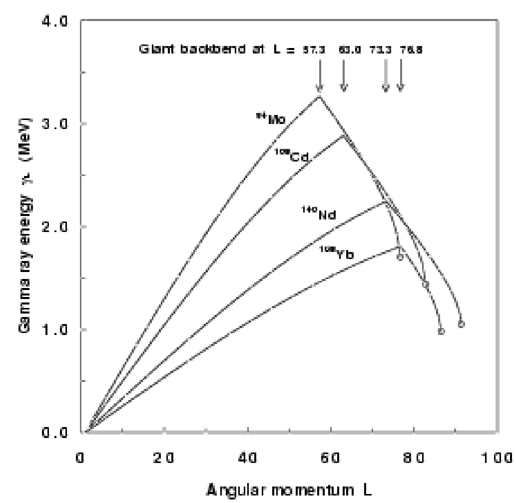

9: Nuclei at Extremes of Isospin

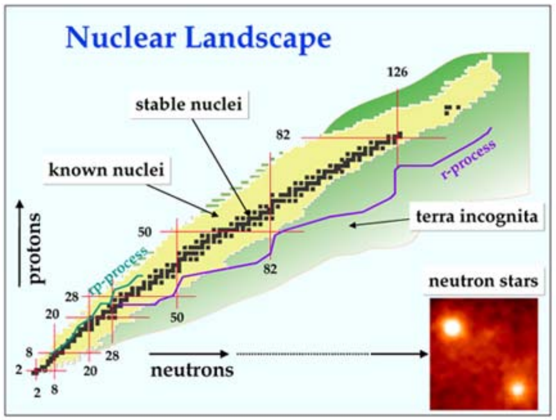

Figure 54: The chart of the nuclides

Distribution of stable nuclei:

A	N	Z	No. stable
even	even	even	166
	odd	odd	8
odd	even	odd	57
	odd	even	53
			$\sum = 284$

But remaining $\sim$ 2300 nuclei exist – particle bound

We have extensive knowledge, both theoretical and experimental, about the behaviour of nuclei near the line of stability. Fig. 55 shows

1. the shell closures at N or Z = 2, 8, 20, 28, 50, 82 and (for N) 126
2. the stable elements versus Z and N
3. values of Z, N for which the binding energy is zero, called the proton or neutron **drip line**

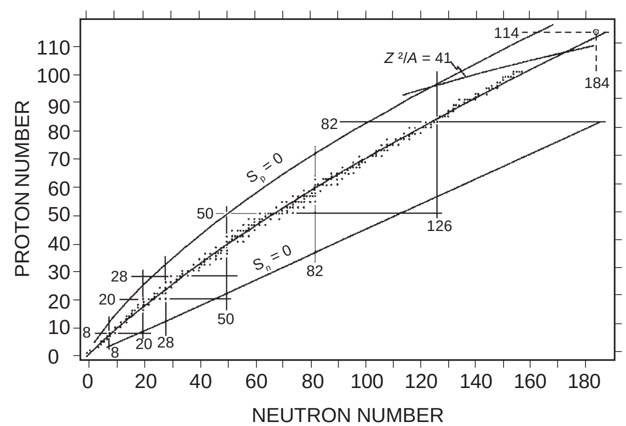

Figure 55: Chart of the nuclides

9.1 Nucleon Driplines

A semiclassical approach (Bethe-Weizsäcker) was to try to fit the following expression for nuclear binding energy to experimental data:

$$m(N,Z) = NM_n + ZM_H - \frac{1}{c^2}B(N,Z), \qquad (127)$$

leading to the *semi-empirical mass formula*:

$$B = a_v A - a_s A^{2/3} - a_c \frac{Z^2}{A^{1/3}} - a_i \frac{(N-Z)^2}{2A} + a_\delta A^{-3/4}.$$

Typical values (MeV) of the parameters are:

Volume term	$a_v = 15.760$,
Surface term	$a_s = 17.810$,
Coulomb term	$a_c = 0.711$,
Isospin term	$a_i = 23.703$,

$$\text{Pairing term } a_\delta = \begin{cases} 34 & \text{even-even nuclei,} \\ 0 & \text{odd-even, even-odd,} \\ -34 & \text{odd-odd.} \end{cases}$$

The last two terms take into account quantal effects. This formula accounts very well for the general trend of observed nuclear masses.

Using the semi-empirical mass formula, the heaviest neutron isotope of a given element occurs when:

$$\left(\frac{\partial B}{\partial N}\right)_{Z=\text{const}} = 0, \qquad (128)$$

which defines the *neutron dripline*. Similarly, the *proton dripline* occurs when:

$$\left(\frac{\partial B}{\partial Z}\right)_{N=\text{const}} = 0. \qquad (129)$$

The beta-stability line can be estimated from:

$$\left(\frac{\partial m(N,A)}{\partial N}\right)_{A=\text{const}} = 0, \qquad (130)$$

where

$$\begin{aligned} m(N,A)c^2 &= N(M_n - M_H)c^2 + AM_Hc^2 - a_v A \\ &\quad + a_s A^{2/3} + a_c \frac{(A-N)^2}{A^{1/3}} + a_i \frac{(2N-A)^2}{2A}. \end{aligned}$$

The solution yields:

$$N - Z = \frac{a_c A^{2/3} - (M_n - M_H)c^2}{(2a_i/A) + a_c/A^{1/3}}. \qquad (131)$$

Nuclei somewhat neutron deficient of those at stability (e.g. ^{152}Dy which is 4 neutrons lighter than the nearest stable isotope, ^{156}Dy) have also been investigated at high angular momentum (high 'spin' as discussed in Sections 8.4, 8.5) since they can be formed by compound nucleus reactions. Current directions of research aim to measure nuclear properties where the proton and neutron number (nuclear **isospin**) are very different from those for stable nuclei.

9.2 Heavy $N = Z$ Nuclei

We have seen that calculations which allow shell corrections to the deformed liquid drop energy (Section 5.2) give minima in the nuclear energy at non-zero deformation. Close inspection of Fig. 26 reveals a minimum at $N = 42$ for $\varepsilon = 0.4$. If both protons and neutrons have this number then the shell correction becomes large enough so that the minimum in the potential energy at this deformation corresponds to the ground state.

Such nuclei are very unstable and therefore difficult to produce in the laboratory. As the nucleus Z increases, the nuclei have to gain an excess of neutrons over protons to counteract the large Coulomb repulsion energy, so that when $Z = 40$, the lightest **stable** zirconium isotope has $N = 50$.

Fig. 56 shows the γ-ray spectrum corresponding to emission from excited states in $^{80}_{40}$Zr$_{40}$, which is formed by 1 in 10^5 decays of the compound nucleus of ^{58}Ni + ^{24}Mg.

Figure 56: Gamma-ray spectrum of ^{80}Zr

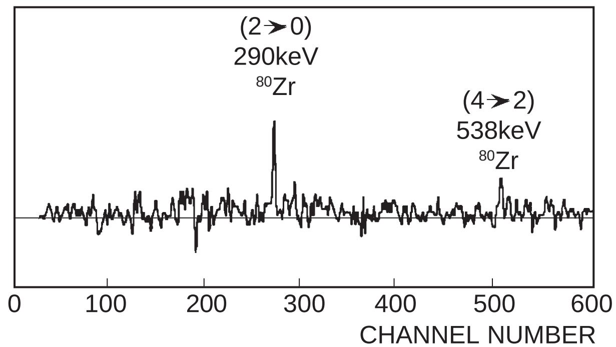

In this experiment the mass of the Zr isotope is measured from the deflection of the Zr atom in a magnetic field, using

$$qe\frac{d\underline{z}}{dt} \times \underline{B} = m\frac{d^2\underline{x}}{dt^2} \tag{132}$$

Here q is the charge state of the recoiling ionised atom, which loses some of its outer electrons as it moves through the target material.

The energies of the $2^+ \rightarrow 0^+$ transition are plotted in Fig. 57 for various $Z = N$ nuclei in this mass region, and show that the most deformed nuclei indeed have $Z \sim N \sim 40$.

Figure 57: Energies of 2^+ states for $Z = N$ nuclei

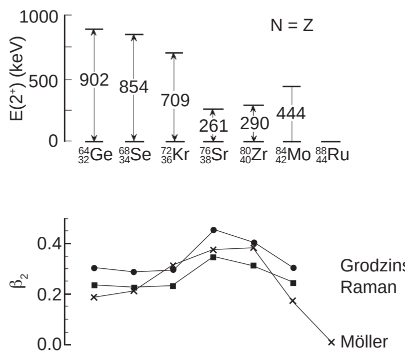

This follows from empirical evidence that the excitation energy of the first 2^+ state in even-even nuclei can be directly related to their deformation: the smaller the energy, the larger the deformation.

Equation 98 predicts that

$$E_{\mathrm{rot}}(I = 2) - E_{\mathrm{rot}}(I = 0) = 3\frac{\hbar^2}{2\mathcal{J}} \tag{133}$$

for *rotational* nuclei. The value of the nuclear quadrupole deformation (ε or β) can be estimated from the moment of inertia $\mathcal{J}$ since the two are related (see Equation 101 for a *rigid* body).

9.3 Proton-Rich Nuclei: Proton Radioactivity

The *proton dripline* is defined by the most massive bound nucleus of every isotonic (N constant) chain. For nuclei that lie above this line, the last proton has a positive energy and, hence, is *unbound*. The proton does not however escape from the nucleus instantaneously as it must overcome the *Coulomb barrier* by quantum tunneling.

Systematics of these proton-emitting nuclei are shown in Fig. 58.

Figure 58: Ground-state proton emitters

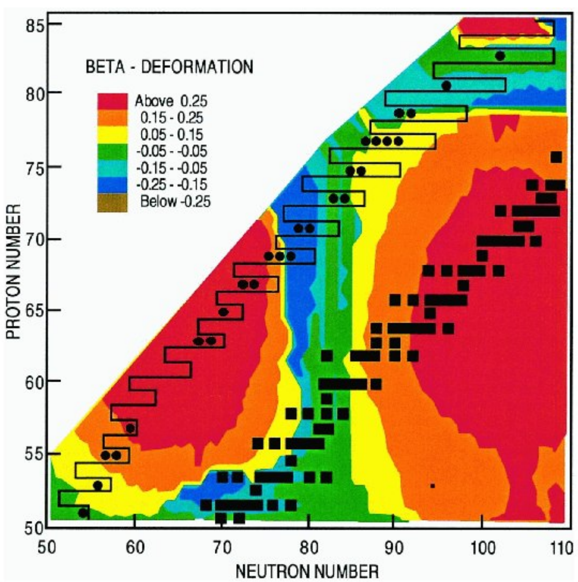

The proton decay probability is sensitive to the energy and *angular momentum* of the proton.

The half-lives of such *proton radioactivity* gives useful information on the specific proton orbitals near the Fermi surface. The half-lives are also sensitive to the nuclear deformation — measured half-lives in ^{131}Eu and ^{141}Ho could only be understood if the nucleus was *deformed* — later confirmed by the observation of rotational bands in ^{141}Ho.

Figure 59: Rotating (deformed) proton emitter: ^{141}Ho

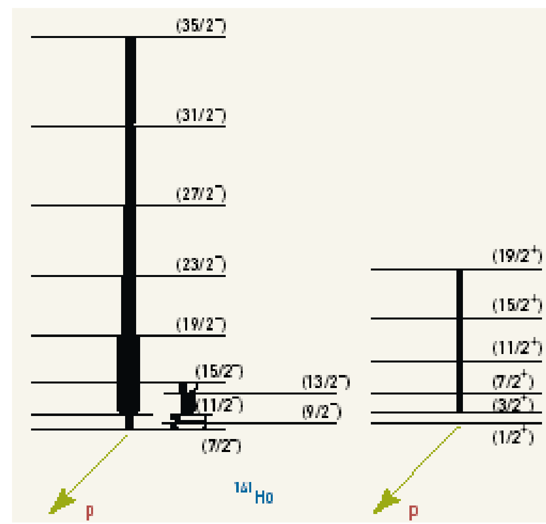

Fine Structure in Proton Decay

In ^{131}Eu, proton decay has been observed to both the ground state of ^{130}Sm and to the first excited state. This establishes the first 2^+ state in ^{130}Sm at an energy of only 121 keV — this implies a large moment of inertia and hence a large prolate ground-state deformation for ^{130}Sm.

Figure 60: Fine structure in proton decay: ^{131}Eu

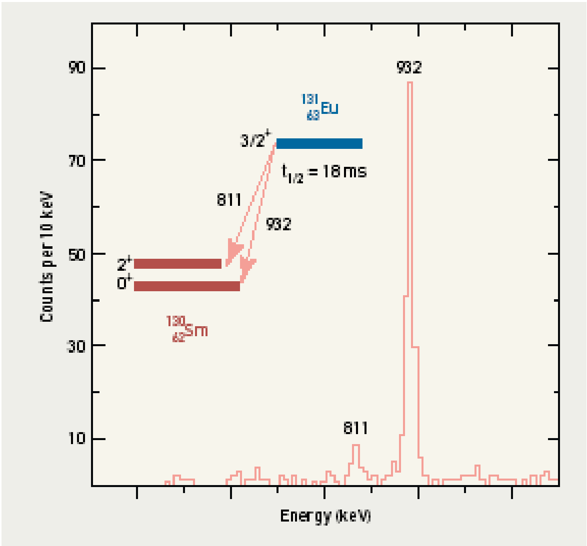

9.4 Direct Two-Proton Decay

A new mode of nuclear decay, *direct two-proton emission*, has been shown to occur in ^{18}Ne. This mode was predicted decades ago, but until recently, experimental efforts had found only sequential emission through an intermediate state — a mechanism energetically forbidden in ^{18}Ne.

Figure 61: Two-proton decay: ^{18}Ne

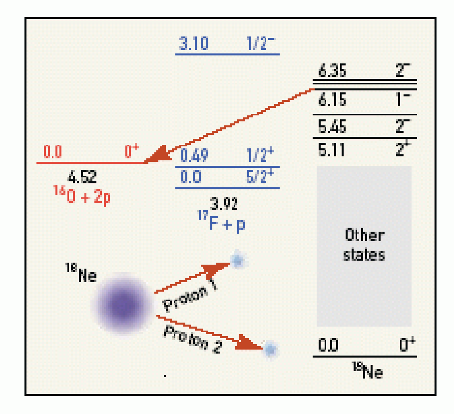

The characterisation of the proton spectra will provide new insight into two-particle correlations and superconductivity in nuclei.

9.5 Neutron-Rich Nuclei: The Physics of Weak Binding

At present, the question of which combination of protons and neutrons form a *bound* nucleus has not been answered experimentally for most of the nuclear chart because of the lack of experimental access to most neutron-rich nuclei. These nuclei are increasingly the focus of present and future experimental and theoretical investigation, as they promise to shed new light on the nuclear many-body problem. They offer a unique terrestrial laboratory for studying neutron-rich matter and their properties represent invaluable input into *astrophysical* problems.

9.6 Nuclear Haloes

By measuring large interaction cross-sections in scattering experiments, it has been deduced that the root-mean-square *'radius'* of ^{11}Li is much larger than expected — implying a diffuse neutron *halo* about the ^{9}Li core.

In 1985 a series of experiments by Tanihata and others using radioactive ion beams of 800 MeV/u found surprising large values of the interaction cross sections for $^{6,8}_{2}\mathrm{He}_{4,6}$ and $^{11}_{3}\mathrm{Li}_{8}$. These results were interpreted in terms of a long tail in the matter distribution. Subsequent measurements revealed that the electric quadrupole moment (see Section 5.3) Q_0 of ^{11}Li is similar to that of the 'normal' sized ^{9}Li so that the proton distributions of the two nuclei must be similar. Therefore the increase in radius observed by Tanihata must come from a neutron tail or **halo**. A halo nucleus is one in which the size of the two (or more) body system is <u>much</u> larger than the range of the nuclear force (1.4 fm). The simplest example is the weakly bound deuteron (see Section 1.7) where the p-n separation is 4 fm.

These nuclei cannot be described by mean field theories such as the shell model or the Hartree Fock method but require descriptions in terms of two- and three- body systems. Such analysis of ^{11}Li suggests that it has a size similar to that of $^{48}_{20}$Ca.

The nucleus ^{6}He is described as a $\alpha + {}^2$n configuration in a two-body system where the di-neutron orbits the α core. More exact three-body descriptions allow both n $-\ \alpha\ -$ n and $\alpha + {}^2$n configurations to co-exist although the latter is more favourable (see Fig. 62).

Figure 62: ^{6}He configurations

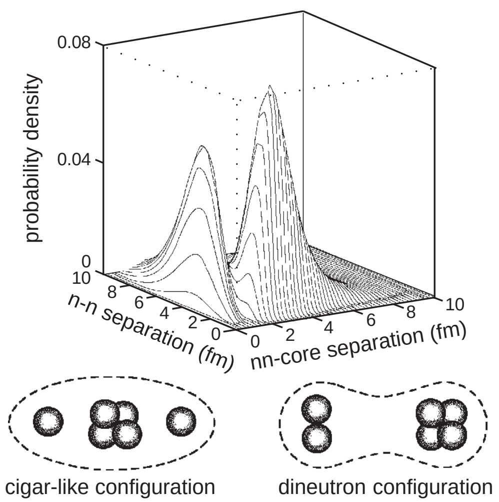

Since both ^{5}He and the di-neutron are unbound, such a system as ^{6}He (or ^{11}Li) is described as a *Borromean* system - if one ring ($\equiv$ neutron or α) is removed then the other two rings will fall apart, see Fig. 63.

Figure 63: Borromean systems

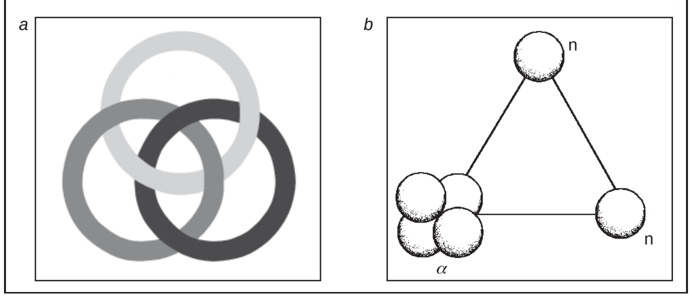

The discovery of halo nuclei has lead to a new form of nuclear matter which can be studied in the laboratory.

Figure 64: The size of ^{11}Li

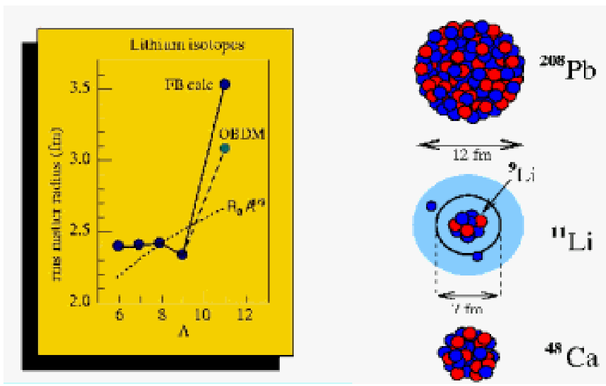

The spatial extent of ^{11}Li with 3 protons is similar to that of ^{208}Pb with 82 protons!

^{11}Li is modelled as a ^{9}Li core plus two valence neutrons that spend more than half their time outside the range of the nuclear force.

Figure 65: The halo nucleus ^{11}Li

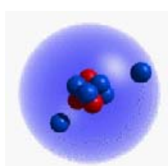

Figure 66: Halo nuclei systematics

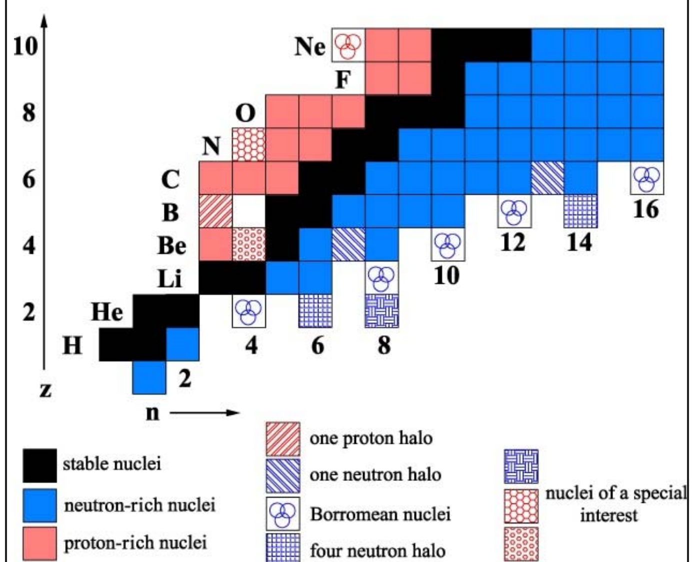

Neutron haloes have now been seen in nuclei as heavy as $^{19}_{6}C_{13}$. Nuclei with two neutrons in their haloes, such as $^{11}_{3}Li_{8}$ and $^{14}_{4}Be_{10}$, have provided insight into a new topology with a *"Borromean"* property — the two-body subsystems of the *stable* three-body system are themselves *unstable*.

Apart from their interest to nuclear physicists, the study of halo nuclei will have applications in the solving of outstanding questions in Big Bang and Stellar Nucleosynthesis, e.g.

- The formation of ^{12}C which arises from
  $\alpha + \alpha \rightarrow {}^{8}$Be
  ^{8}Be + $\alpha \rightarrow$ Borromean ^{12}C $\xrightarrow{\gamma}$ 'normal' ^{12}C
- The reaction ^{4}He(2n,γ)^{6}He(2n,γ)^{8}He can bridge the gaps at A=5 and A=8, which has been a long standing problem in modern astrophysics.
- The solar neutrino problem whereby theory always overestimates the measured neutrino flux from the sun. Most high energy neutrinos are produced from the formation of the proton halo nucleus $^{8}_{5}$B.

9.7 Changing Magic Numbers

The weak binding inherent in nuclei at the driplines is likely to have a profound influence on the nuclear properties, including the underlying shell structure. In additon to changes in the radial behaviour of the potential binding the nucleons together, the *spin-orbit* force, which is crucial for determining the magic shell closures, is expected to decrease near the neutron dripline.

Magic closed-shell numbers (2, 8, 20, 28, 50, 82,...) are well established for nuclei near the region of β-stability. They are predicted by the spherical shell model that approximates the nuclear potential by a harmonic oscillator to which a strong *spin-orbit* term $\underline{\ell}.\underline{s}$ and a *centrifugal* term $\underline{\ell}^2$ are added.

The ordering of the proton (neutron) energy levels strongly depends on the filling of neutron (proton) orbitals through a Hartree-Fock *self-energy* correction. A typical example is the relative ordering of the $1g_{7/2}$ and $2d_{5/2}$ proton orbitals in $_{51}$Sb nuclei as a function of neutron number.

Figure 67: $1g_{7/2}$ and $2d_{5/2}$ relative energies in Sb

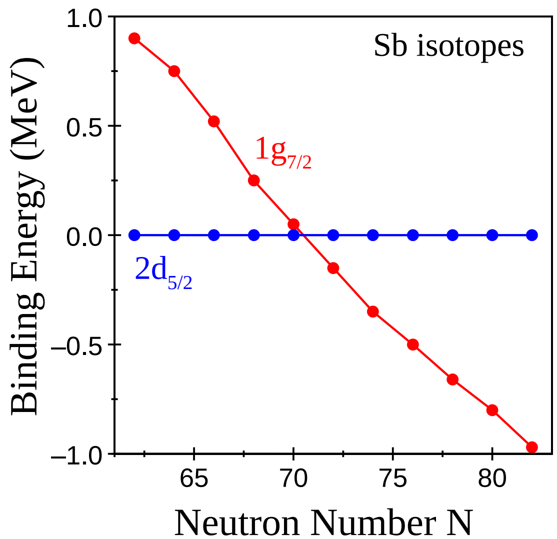

By studying shifts in single-particle energies in light nuclei, it has been shown that the neutron magic numbers at $N = 8, 20$ can be changed into $N = 6, 16$, respectively. This is in agreement with the changes observed in the ordering of shells for neutron-rich light nuclei and seems to originate from a strong attractive *proton-neutron* interaction between *spin-orbit* partners.

9.8 Nuclei at the Extremes of Mass and Charge: Superheavies

Investigations of the heaviest nuclei probe the role of the *Coulomb* force and its interplay with quantal *shell effects* in determining the boundaries of the nuclei landscape.

If nuclei behaved like two-fluid proton-neutron droplets, elements with proton numbers beyond $Z \approx 100$ would not exist — the strong Coulomb force would result in instantaneous *fission*. But *"superheavy"* elements with atomic numbers as high as $Z = 112$ have already been synthesised, and their relative stability is a striking example of nuclear shell structure, which provides the additional *binding energy* needed to overcome the disruptive Coulomb force.

Modern nuclear structure calculations not only predict which combinations of protons and neutrons can be made into heavy nuclei, but also indicate that stability arises in specific cases from the ability of the nucleus to *deform*.

The liquid drop model predicts that if $Z^2/A > 49$ then the fission barrier vanishes. This implies that we cannot form nuclei (e.g. using compound nuclear reactions) with $Z > 100$. However, nuclear models predict that there are substantial shell correction energies for the **ground states** of very heavy deformed nuclei and also nuclei near the next spherical shell closure beyond $Z = 82$ and $N = 126$ (**superheavies**), possibly at $Z = 114$ and $N = 184$.

Figure 68: Calculated fission-barrier heights

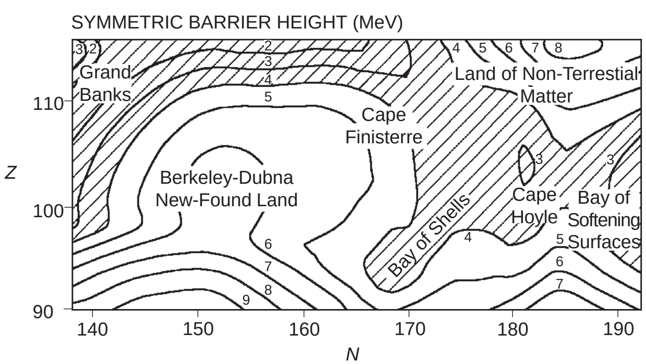

With the shell correction, the barrier heights are calculated to be sufficient to make both superheavies and nuclei with $Z \sim 100 - 110$ and $N \sim 150 - 170$ stable against fission. Fig. 68 shows these calculated values (in MeV).

In fact these nuclei are unstable against α-decay, and the α-decay half life (in s) is given empirically by the relation:

$$\log_{10}(t_{\frac{1}{2}}) = 1.61 Z E_\alpha^{-\frac{1}{2}} - 1.61 Z^{\frac{2}{3}} - 28.9 \qquad (134)$$

In this Equation 134, E_α (in MeV) is the α decay energy which is directly related to the mass difference of the parent (Z, A) and daughter $(Z-2, A-4)$ nuclei. The α decay provides the experimental technique whereby the heavy elements can be identified, by measuring the chain of α-decays until a known nucleus is reached, see Fig. 69

Notice that the α lifetimes are very long ($> 10^{-3}$ s) on the nuclear time scale.

Figure 69: α decay chain

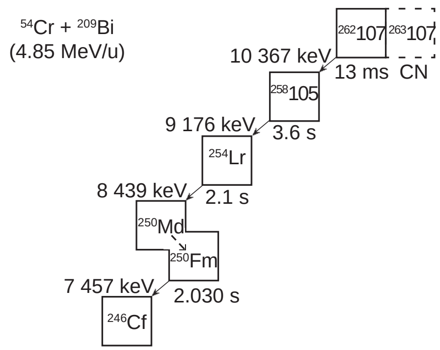

The heaviest element identified so far using this technique is $^{277}112_{165}$ by the Armbruster - Munzenberg group at Darmstadt, Germany.

9.9 Superheavies at high spin

Recently spectral information has been obtained for elements with $Z > 100$.

Nuclei around nobelium:

Figure 70: The superheavy elements

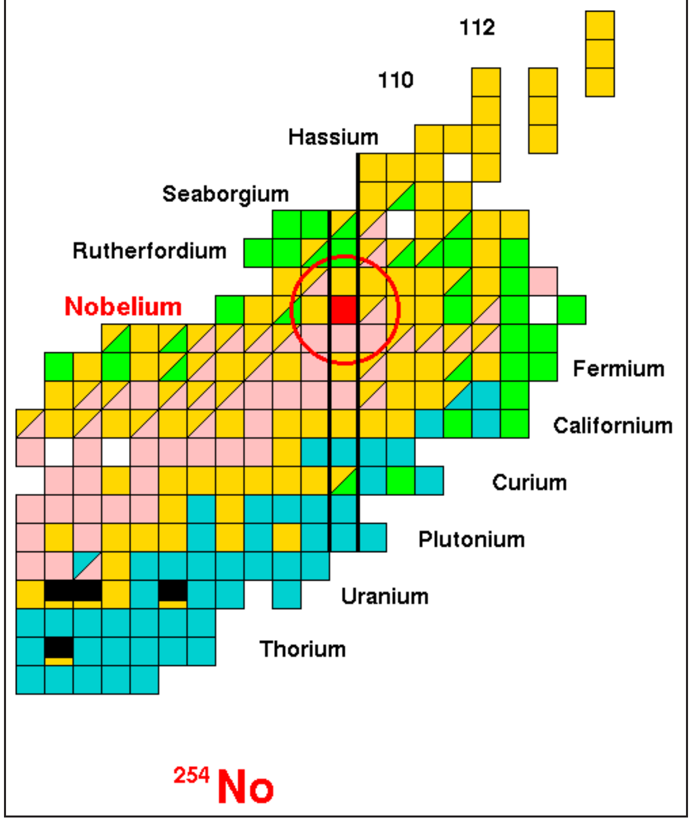

The ground-state rotational band of ${}^{254}_{102}\mathrm{No}_{152}$ has been identified and its behaviour (energy spacing) is consistent with a sizeable prolate deformation for this nucleus — an axis ratio of 4:3 or $\beta_2 \approx 0.3$. In addition, the fact that states up to $20\hbar$ of angular momentum were observed underscores the remarkable resilience of the shell effects against centrifugal force and fission.

Figure 71: Ground-state rotational band in ^{254}No

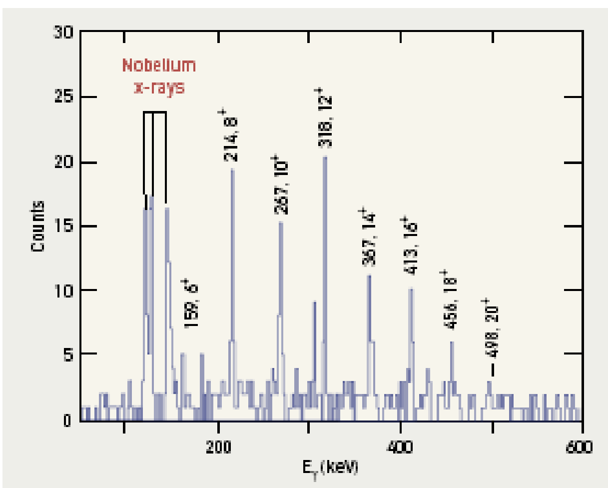

10: Mesoscopic Systems

Microscopic — $\underbrace{\textit{Mesoscopic}}$ — Macroscopic

Large yet *finite* number of constituents.

10.1 Femtostructures and Nanostructures

There is intense research today on quantum nanostructures — grains, droplets or surface structures, which confine a number of electrons within a nanometre-size scale. Nuclei are *femtostructures*. All these small systems share common phenomena which appear on very different energy scales — nuclear: MeV, molecular: eV, solid-state: meV.

A central question is how the structure of mesoscopic systems develops as a function of the number of constituents. In nuclei, this evolution is strongly mediated by the concept of *shell structure*, arising from the basic aspects of the mean field and the effects of the Pauli Exclusion Principle.

Figure 72: Shell structures in nuclei and metal clusters

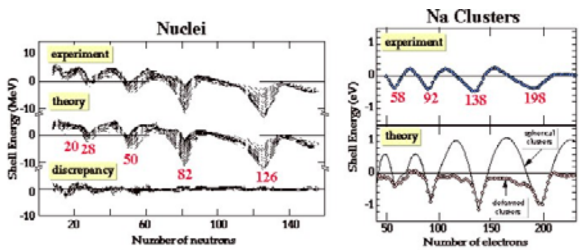

Shell structure has also now been found in metallic clusters and quantum dots and is the key to understanding the structure of these systems.

10.2 The Quantality Parameter

B.R. Mottelson, Nucl. Phys. **A649** (1999) 45c

The *quantality* parameter $\Lambda = \hbar^2/Ma^2V_0$ measures the strength of the two-body attraction V_0 expressed in units of the quantal kinetic energy associated with a localisation of a constituent particle of mass M withan a distance a corresponding to the radius of the force at maximum attraction.

Table 4: Values of the quantality parameter

Constituents	M	V_0 (eV)	a (cm)	Λ	T=0 matter
^{3}He	3	9×10^{-4}	2.9×10^{-8}	0.21	liquid
^{4}He	4	9×10^{-4}	2.9×10^{-8}	0.16	liquid
H_2	2	3×10^{-3}	3.3×10^{-8}	0.07	solid
Ne	20	3×10^{-3}	3.1×10^{-8}	0.007	solid
nuclei	1	1×10^{8}	9×10^{-14}	0.4	liquid

For small Λ the quantal effect is small and the ground state of the many body system will be, as in classical mechanics, a configuration in which each particle finds a static optimal position with respect to its nearest neighbours. If Λ is large enough the ground state may be a *quantum liquid* in which the individual particles are *delocalised* and the low-energy excitations (quasiparticles) have infinite mean free path.

The Pauli Exclusion Principle gives nucleons essentially mean free path and hence the behaviour of the nucleus as a quantum liquid. However, if the strength of the nuclear force was just 2–3 times larger, nuclei could have been crystalline!

Figure 73: Three types of Fermi liquid droplets

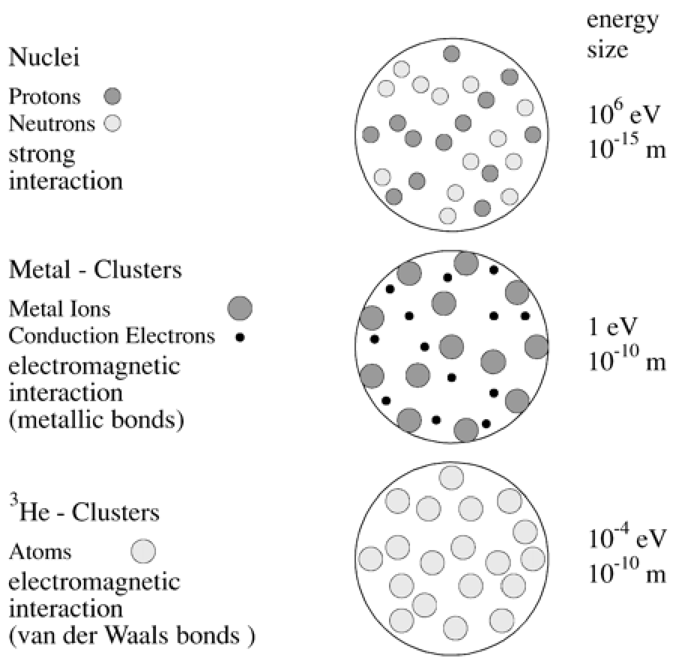

10.3 Atomic Clusters as a Branch of Nuclear Physics

S.G. Frauendorf and C. Guet, Ann. Rev. Nucl. Part. Sci. **51** (2001) 219

The conduction electrons in clusters of simple metal atoms are approximately independent and free. Nucleons in nuclei also behave as *delocalised* and *independent fermions*. This behaviour generates analogies between metal clusters and nuclei. such as shell structure, shapes, and vibrational modes.

Clusters are aggregates of atoms or molecules with a well-defined size varying from a few constituents to several tens of thousands. Cluster physics lies between atomic and molecular physics, on the one hand, and condensed matter physics, on the other.

The finite number of the constituents leads to novel *structural* and *thermodynamic* properties with no equivalent in bulk matter. Clusters are distinguished from bulk matter insofar as their properties are strongly affected by the existence of a *surface* involving a *large fraction* of the number of constituents.

For example, in a cluster of 55 atoms of argon, more than 30 are on its surface!

Quantum dots are nanometre-scale crystals that were developed in the mid-1980s for optoelectronic applications. They are composed of hundreds to thousands of atoms of an inorganic semiconductor material in which *electron-hole* pairs can be created and confined. The size of quantum dots can be tuned with nanometre precision during chemical synthesis.

Both clusters and nuclei are characterised by a constant density in the interior and a relatively thin surface layer — the binding energy can be expanded in powers of $N^{-1/3}$. This is the *liquid drop model* — the first terms of this expansion can be interpreted as the energies of a droplet of charged liquid.

10.4 The Spherical Droplet

The first terms in the expansion are:

$$E_{LD}(N,Z) = fN + 4\pi\sigma R^2 + WZ + C\frac{Z^2e^2}{R}, \quad (135)$$

$$= fN + b_{surf}N^{2/3} + WZ + b_{coul}Z^2N^{-1/3}, \quad (136)$$

where $R = r_{WS}N^{1/3}$ is the radius of the droplet, N the number of atoms, and Z the net charge. The first term is the *volume energy*, which contains the binding energy per particle f of the bulk metal. The second term is the *surface energy*, where σ is the coefficient of surface tension. The third term contains the *work function* W, which is the energy required to remove one electron from the bulk metal. The fourth term is the *Coulomb energy*.

In the case of nuclei, the charge is evenly distributed because the symmetry energy keeps the ratio of the neutron and proton densities roughly constant. Thus, the energy of a homogeneously charged droplet, for which $C = 3/5$, is a good approximation. The density of charge added to a cluster tends to accumulate in the surface — so for a very large cluster $C \rightarrow 1/2$.

10.5 Shell Structures

Shell structure is the bunching of energy levels of a particle in a two- or three-dimensional potential. In the figure, the mass spectrum of Na clusters (top) exhibits a shell structure similar to an electron in a Woods-Saxon potential (bottom):

Figure 74: Shell structure of Na clusters

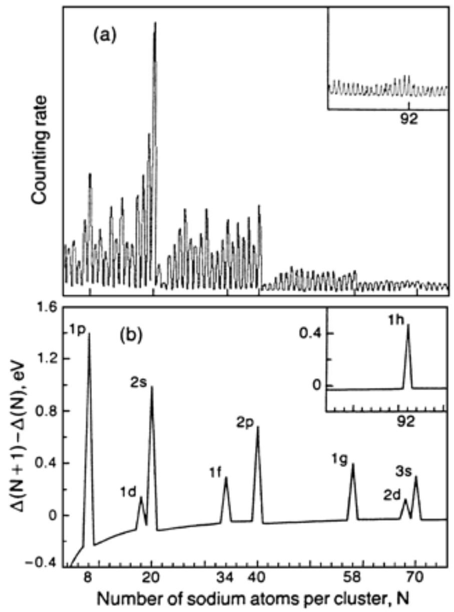

Predicted shell structures — *magic numbers*:

Figure 75: Predicted level sequences

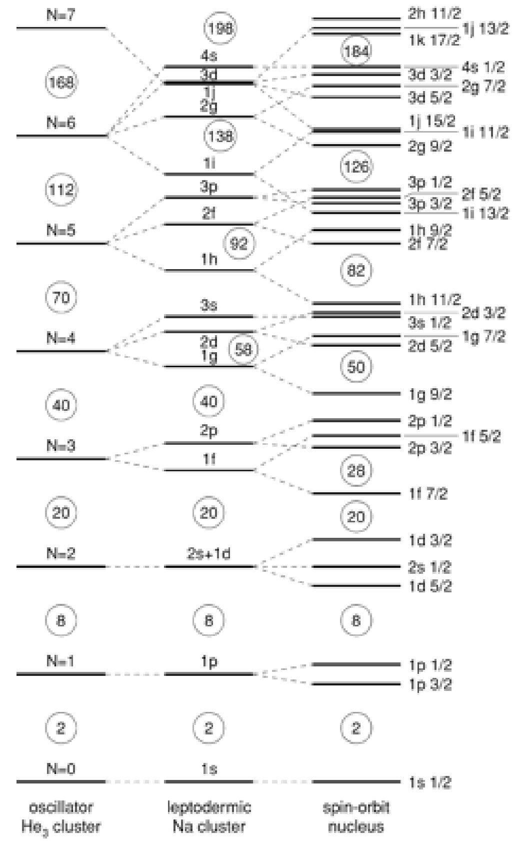

10.6 Supershell Structures

Figure 76: Predicted cluster supershell structure

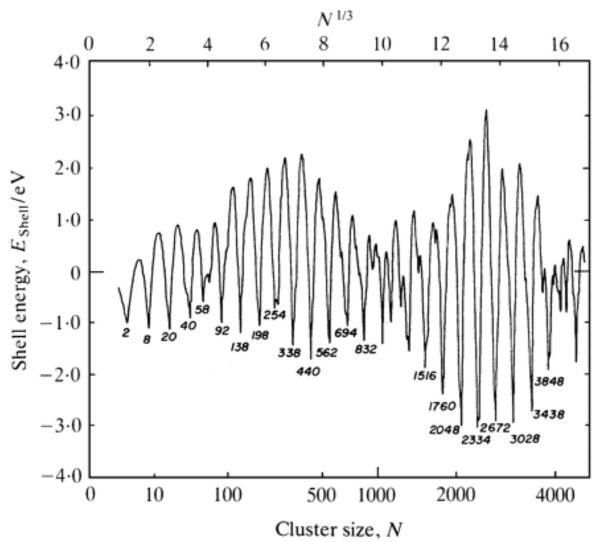

Nuclear theorists Balian and Bloch (1972) studied the density of states in a spherical cavity and noted that its oscillations as a function of energy (shell structure) are enveloped by a long-wavelength oscillation (*beat pattern*). Their work did not receive much attention from nuclear physicists because the effect is not observable in nuclei.

Nuclei become unstable long before the first half period of the long-wavelength oscillation is completed. Nishioka et al. (1990) realised that such *supershell* structure could also occur in metallic clusters. Soon afterwards Pedersen et al. (1991) demonstrated experimentally the existence of supershell structure for Na clusters. The beat structure has its first minimum at $N \approx 1000$.

Figure 77: Experimental supershell structure of Na clusters

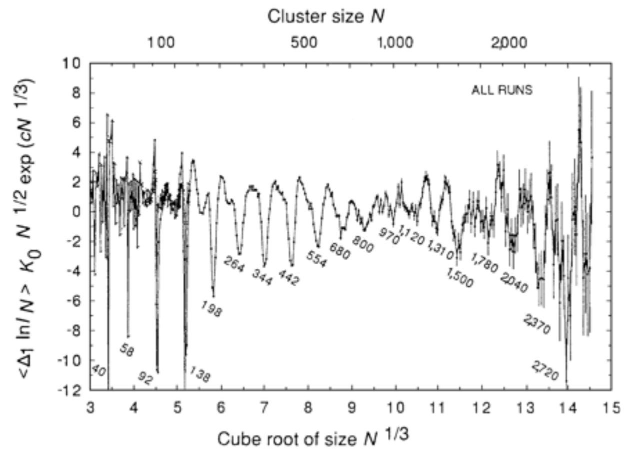

Supershell structure was also found in Li and Ga clusters, where the second beat could be identified.

10.7 Mesoscopic Quantal Effects

Nuclear structure studies resolve the quantal levels of individual nuclei. The interpretation is often based on a comparison between theory and experiment on this *microscopic* level. In cluster physics, the experimental resolution does not permit such an approach. The measured quantities are *averaged* over thermal fluctuations and for heavier clusters also over a certain interval of particle number — a simplified description is then possible.

10.8 Periodic Orbit Theory (POT)

This describes the shell structure in terms of classical orbits. We consider an infinitely deep spherical square-well potential — the electrons occupy all states up to the Fermi energy $e_F = p_F^2/2M$. Their level density is averaged over a certain energy interval Γ. The shell energy is:

$$E_{SH} = e_F N^{1/6} \sum_{\beta} A_\beta \sin\left(\frac{p_F L_\beta}{\hbar} + \nu_\beta\right) D\left(\frac{\Gamma \tau_\beta}{\hbar}\right), \quad (137)$$

where D is a suppression factor.

The sum runs over all families of classical periodic orbits, where L_β is the length of the orbit and $\tau_\beta = L_\beta/v_F$ is the revolution time. For sufficiently large Γ, only the shortest orbits contribute to E_{SH} (finite D). The amplitudes A_β are of the order of one for these orbits, while the phases ν_β are given by the number of reflections on the surface.

The classical system corresponds to a point mass inside a hollow sphere, of radius R, bouncing elastically from the walls. The periodic orbits are polygons. The important orbits are the triangle $\triangle$ and the square $\square$. They are the shortest orbits with lengths $L_\triangle = 5.19R$ and $L_\square = 5.66R$, respectively. Since $L_\triangle \approx L_\square$, we can also use $A_\triangle \approx A_\square \approx A$ and $D_\triangle \approx D_\square \approx D$. Using the addition theorem for sine functions yields:

$$E_{SH} = 2 e_F N^{1/6} A \times \sin\left(\frac{p_F \overline{L}}{\hbar} + \overline{\nu}\right) \cos\left(\frac{p_F \Delta L}{\hbar} + \Delta\nu\right) D\left(\frac{\Gamma\tau}{\hbar}\right), \quad (138)$$

$$\overline{L} = (L_\square + L_\triangle)/2 = 5.42R, \quad (139)$$

$$\Delta L = (L_\square - L_\triangle)/2 = 0.24R. \quad (140)$$

The phases $\overline{\nu}$ and $\Delta\nu$ are defined analogously.

Figure 78: Supershell structure from interfering periodic orbits

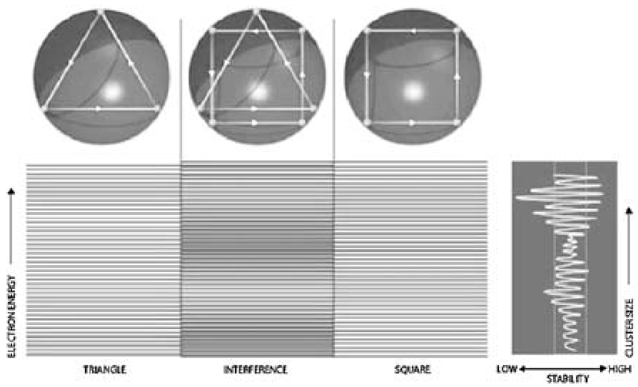

The above figure shows that the superposition of two oscillations (periodic orbits) with similar frequencies results in a *beat pattern*.

The fast oscillation represents the basic shell structure. Its minima appear at $p_F\overline{L} = 2\pi n + c$.

The slow oscillation is the supershell structure. It has a half-period $p_F \Delta L = \pi$ which corresponds to $\overline{L}/2\Delta L \approx 12$ shells. Due to the spin-orbit potential, POT's application to nuclei remains on a more qualitative level than for metallic clusters.

10.9 Deformation: Loss of Spherical Symmetry

Deformation is a common concept for subatomic and mesoscopic systems with many degrees of freedom — nuclei, molecules, clusters. It appears in field theory (Higgs mechanism), in the physics of superconductors, in condensed matter physics and other fields of physics. The microscopic mechanism leading to the existence of deformed configurations, *spontaneous symmetry breaking*, was first proposed by Jahn and Teller (1937) for molecules.

Nuclei with incompletely filled shells tend to *deform* because the level density near the Fermi surface is high for a spherical shape. When the shape of the potential is changed, the nucleonic levels rearrange, such that the level density is reduced which results in an energy gain — nuclear *Jahn-Teller* effect. Nuclei can easily respond because they consist of delocalised nucleons (liquid). The presence of heavy discrete ions leads to a more varied response of clusters. Nevertheless, similar shapes are predicted for nuclei and clusters despite the very different nature of the interactions between the constituents.

Figure 79: Predicted metal-cluster and nuclear shapes

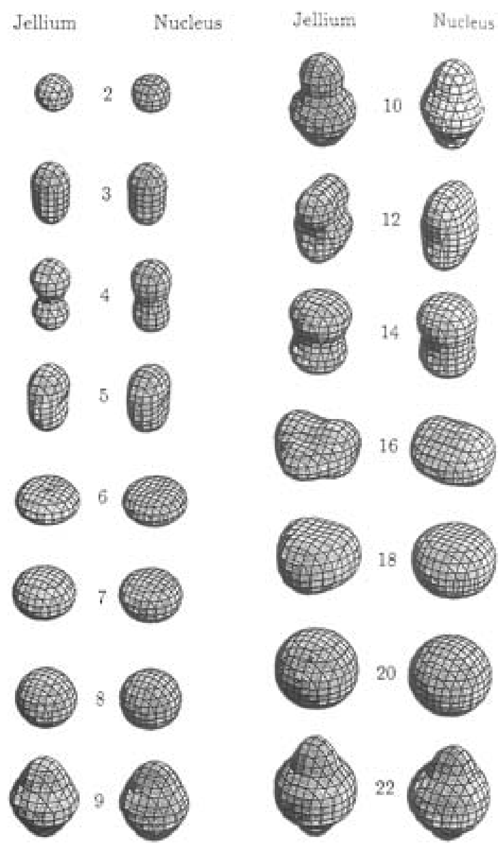

10.10 Vibrational Modes

Unlike nuclei, there is only clear evidence for collective *dipole* vibrations in clusters.

Figure 80: Giant dipole resonances in clusters and nuclei

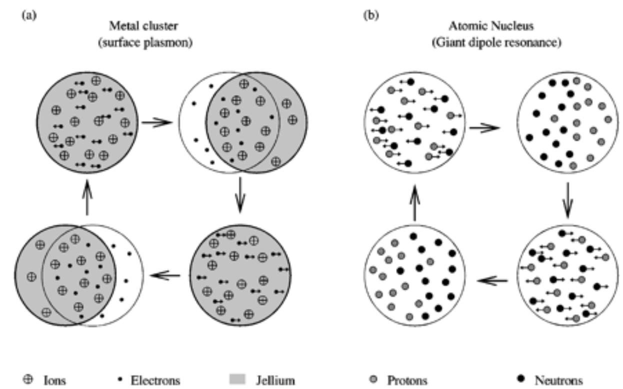

10.11 Differences between Clusters and Nuclei

There is only *one* kind of nuclear matter. It has a *single equation of state* — however, all materials have their own equation of state.

In a cluster, as in bulk matter, it is the constituents that determine the *density* and *binding energy*.

10.12 Phase diagrams

Recent experiments have characterised the liquid-to-vapour phase transition in nuclei. The phase diagram for the nucleus of a Kr atom is shown below compared to that for a macroscopic fluid of Kr atoms. The similarity is a reflection of the fact that the effective forces between nucleons (*strong* force) are similar to those between molecules in ordinary liquids (*electromagnetic* force). In both cases the force is repulsive at short distances yet attractive at long distances.

Figure 81: Phase diagram of Kr nucleus and atomic fluid

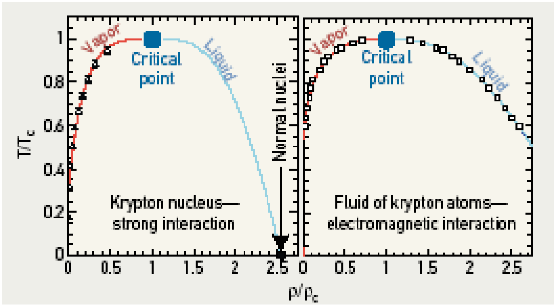

The critical temperatures and densities are however vastly different:

Liquid: $T_C = 209\ K$; $\rho_c \approx 0.1\ moles/cm^3$,

Nucleon: $T_C = 8 \times 10^{10}\ K$; $\rho_c \approx 8 \times 10^{13}\ moles/cm^3$.

10.13 Nuclear Molecules

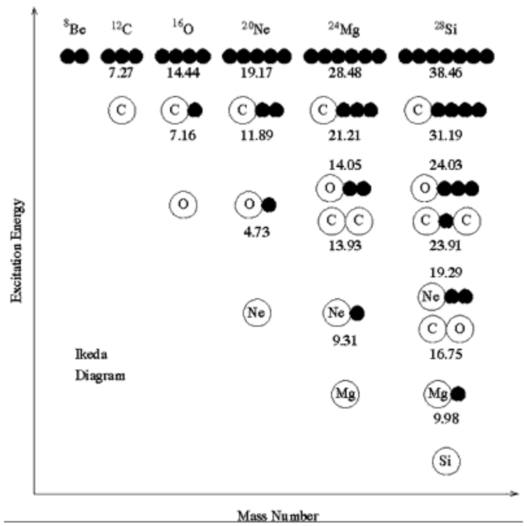

Figure 82: The "Ikeda Diagram"

Speculations about the existence of *clusters*, such as α particles, in nuclei have been around since the earliest days of nuclear physics, stimulated initially by the observation of α-particle decay. However, the observation of a complex fragment emerging from a nucleus does not necessarily imply that it existed as a pre-formed entity in the nucleus.

During the 1960's a number of theoretical groups began work on the problem of describing the nucleus in terms of clusters of α particles. The *Ikeda Diagram* illustrates possible cluster structure in light nuclei. Ikeda believed that the cluster structures would show up at energies just above the relevant separation energies of the fragments.

At the same time Brink presented the light α conjugate nuclei as almost crytalline structures with specific arrangements of the α clusters.

Figure 83: Bloch-Brink cluster model

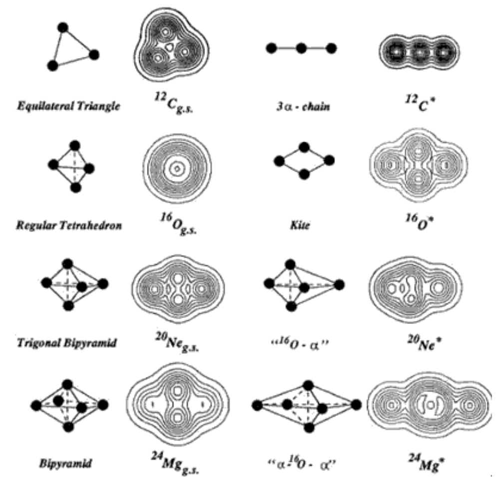

Figure 84: ^{12}C as a cluster of three α particles

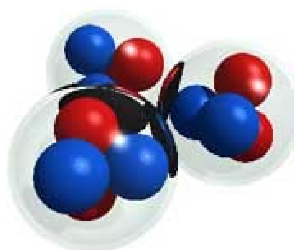

At about the same time that Ikeda and Brink were developing their early models of α clustering, the first experiments which suggested that *larger* clusters might also exist were just beginning. When the yield of reaction products from the collision of two ^{12}C nuclei was measured, narrow *resonances* appeared in the excitation function. This led to the speculation that the two ^{12}C nuclei were forming an intermediate *nuclear molecule* in the reaction. This is an even more extreme form of cluster structure in the nucleus.

When the spins of the resonances were measured, they appeared to increase with energy exactly as expected for the rotation of two touching ^{12}C nuclei!

10.14 Nuclear Sausages

Cluster model calculations for ^{12}C show evidence for a *chain state* consisting of *three* α particles in a row. This shape has an axis ratio of 3:1.

Similarly, calculations for ^{24}Mg show evidence for a *chain state* consisting of *six* α particles in a row. This extreme shape has an axis ratio of 6:1!

Figure 85: Cluster configurations in ^{24}Mg

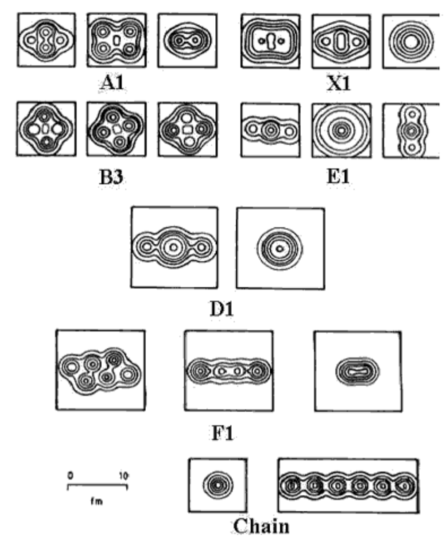

10.15 Binary Cluster Model

It has been observed that measured transition quadrupole moments of many superdeformed bands (axis ratio $\approx$ 2:1) are accurately described by:

$$Q_t \approx 2R_0^2 \left[Z_T A_T^{2/3} - Z_1 A_1^{2/3} - Z_2 A_2^{2/3} \right], \quad (141)$$

with $R_0 = 1.07 fm$. This expression results from considering the states of the nucleus (Z_T, A_T) to be composed of two clusters (Z_i, A_i) in relative motion. To choose the binary fragmentation, differences between a fragment's actual binding energy and its liquid-drop estimate are considered.

Recently, a strongly deformed band in ^{108}Cd was observed (Clark et al., 2001) with a measured $Q_t \sim 9.5\ eb$. The *binary cluster model* predicts the split for ^{108}Cd to be $^{58}_{26}\mathrm{Fe}_{32}$ + $^{50}_{22}\mathrm{Ti}_{28}$, which is slightly asymmetric because of the influence of closed shells at nucleon numbers 20 and 28. This configuration has a predicted quadrupole moment of $Q_t = 9.2\ eb$, which is close to experiment.

These very extended shapes are predicted to be widespread in mass $A \sim 110$ nuclei.

11: Nuclear Reactions

There are various types of reaction depending on:

- Energy of the projectile,
- (Z, A) of the target and projectile,
- Proximity of the paths of the target and projectile (*impact parameter* b)

Figure 86: Various types of reaction

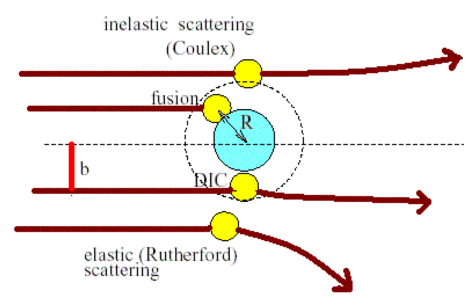

Central Reactions: at small b

- Collision with fusion of target and projectile – compound nucleus formation.

Peripheral Reactions: at large b

- Scattering – incident projectile is present afterwards.
  - Elastic scattering – projectile deflected unscathed from unchanged target.
  - Inelastic scattering – target or projectile becomes excited or breaks up.
    - inelastic nuclear excitation,
    - direct break up,
    - Coulomb excitation,
    - transfer reaction.

Deep Inelastic Collisions (DIC): at intermediate b

- No fusion, but some (massive) transfer of particles between projectile and target.

11.1 Collision Kinematics

Many quantities must be conserved in nuclear reactions – energy (mass), momentum, angular momentum, parity, charge and at low energies the number of protons and neutrons.

Consider the reaction:

$$a + A \rightarrow b + B, \quad \text{usually written: } A(a,b)B$$

where a is a light projectile bombarding a massive target A (at rest). B is the "target-like" product and b is the "projectile-like" product. The Q-value for the reaction is:

$$Q = \left[(M_A + M_a) - (M_B + M_b)\right] c^2. \qquad (142)$$

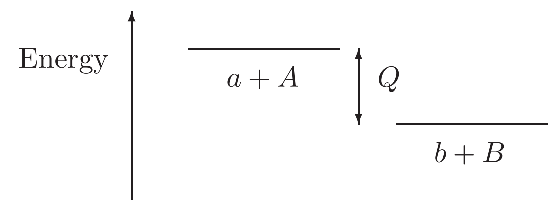

As in chemistry, an *exothermic* reaction ($Q > 0$) gives off energy (kinetic energy of reaction products); an *endothermic* reaction ($Q < 0$) requires an input of energy to occur.

Reactions with $Q > 0$ can, in principle, proceed if the collision occurs at zero incident kinetic energy. For $Q < 0$, we need to input energy – kinetic energy of incident particle.

To take into account the recoil of the products, we consider the kinetic energy available in the centre of mass frame T_c:

$$\text{Momentum}: \quad P_a = M_a V_a,$$
$$\text{Kinetic Energy}: \quad T_a = \tfrac{1}{2} M_a V_a^2 = \tfrac{P_a^2}{2M_a}.$$

$$\text{Momentum}: \quad P_c = P_a \tfrac{M_A}{M_a + M_A},$$
$$\text{Kinetic Energy}: \quad T_{a,c} + T_{A,c} = \tfrac{P_c^2}{2M_a} + \tfrac{P_c^2}{2M_A}.$$

From which it follows:

$$T_c = T_a \frac{M_A}{M_a + M_A}. \tag{143}$$

For a negative-Q reaction to occur:

$$T_c + Q > 0; \; T_c > |Q|; \; T_a > \frac{M_a + M_A}{M_A} |Q|, \tag{144}$$

and this defines a *threshold energy* T_a for the reaction to proceed.

11.2 Compound Nucleus Model

Introduced by Niels Bohr in 1936:

Formation phase		Decay phase
$a + A \rightarrow$	C^*	$\rightarrow a + A^*$
		$\rightarrow b + B^*$
		$\rightarrow \gamma + C^*$

The model assumes that the incident particle a enters the nucleus A, suffers collisions with the constituent nucleons of A until it has lost its incident energy, and becomes an indistinguishable part of the nuclear constituents C^*.

Consider a beam of alpha particles ($E = 5 \; MeV/A$) on ^{60}Ni:

$$\alpha \; + \; ^{60}\text{Ni} \rightarrow \; ^{64}\text{Zn}^*.$$

The energy of the incident particle is:

$$\frac{1}{2} M_\alpha v^2 = 5 \; (MeV/A) \times A,$$
$$\frac{1}{2} A m_N c^2 \left(\frac{v}{c}\right)^2 = 5A.$$

Using relativistic formulae,

$$E = mc^2 = \gamma m_0 c^2 = \gamma M_0, \tag{145}$$

with M_0 is the *rest-mass energy*, the total energy is given by:

$$E = M_0 + T, \tag{146}$$

and hence:

$$T = (\gamma - 1) M_0, \tag{147}$$

where:

$$\gamma = \frac{1}{\sqrt{1-\beta^2}} \quad , \quad \beta = \frac{v}{c}. \tag{148}$$

So by comparing the kinetic energy T to the rest-mass energy M_0, we can estimate γ, and hence β for this reaction. We find that $\beta \sim 0.1$ – i.e. *nonrelativistic*.

It then follows that it takes $\sim 10^{-22}\ s$ for the incident α particle to travel across the target nucleus.

In a compound nucleus, the first emission of a nucleon or a γ-ray takes $> 10^{-20}\ s$, and often $\gg 10^{-20}\ s$ – the α particle could traverse the nucleus more than a hundred times! Hence, within this timescale, the compound nucleus equilibrates all its degrees of freedom – it shares out energy between all the nucleons. The projectile is absorbed and the system *loses its memory* of how it was formed.

Bohr's *hypothesis of independence* states that the formation and decay of a compound nucleus are independent. It does not matter how we form the compound nucleus – the decay modes will be the same. Note, however, that the excitation energy and angular momentum are remembered!

We could make ^{64}Zn by $\alpha\ +\ ^{60}$Ni or $p\ +\ ^{63}$Cu reactions. If the excitation energy (and spin) brought into the compound system were the same for each reaction, then the probability of each decay channel would be the same.

11.3 Geometric Cross-Section

The concept of a cross-section is statistical.

• Definition: The cross-section is the number of processes per second when one scattering centre is exposed to unit flux of incident particles.

In the classical picture shown below, the projectile and target nuclei will interact (fuse) if the *impact parameter* b is less than the sum of their radii. A disk of area $\pi(R_1 + R_2)^2$ is swept out which defines a geometric cross-section. Remember – the units of cross-section are area ($1\ b = 100\ fm^2$)!

Figure 87: Geometric cross-section

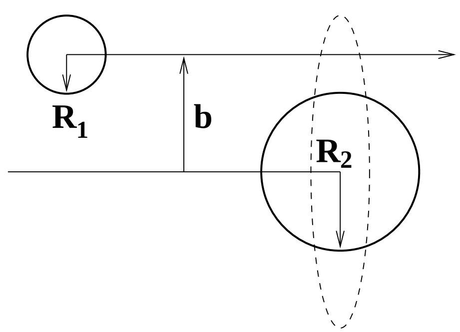

11.4 Coulomb Excitation

In *Coulomb excitation* or *Coulex* reactions, the kinetic energy of the projectile is transferred into nuclear excitation energy by the long-range Coulomb interaction. The biggest effect is for deformed nuclei with high Z. These deformed nuclei show rotational band structures up to spins in excess of $20\hbar$ in Coulex reactions.

In pure Coulex the charge distributions of the two nuclei do not overlap at any point in the collision.

• Example:

^{234}U bombarded by $5.3\ MeV/A$ ^{208}Pb. Note the beam energy is kept low (less than the Coulomb barrier) so that other reactions (e.g. fusion) do not compete, i.e.

$$\begin{aligned} \text{Beam energy} &= 5.3 \times 208\ MeV, \\ &= 1100\ MeV = 1.1\ GeV. \end{aligned}$$

The Coulomb barrier (converting to the lab frame) for this reaction is:

$$\frac{Z_1 Z_2 e^2}{4\pi\varepsilon_0 (R_1 + R_2)} \times \left(\frac{A_1 + A_2}{A_2}\right) \approx 1300\ MeV.$$

11.5 Intermediate Energy Coulex

At higher beam energies ($> 30\ MeV/A$), well above the Coulomb barrier, Coulex can still take place but in competition with other violent reactions. Intermediate energy Coulex is characterised by straight line trajectories with impact parameters larger than the sum of the radii of the two colliding nuclei. The process is now so fast that only the first excited states (2^+ for even-even nuclei) are populated — in both beam and target nuclei.

• Example:

A gold target bombarded by $140\ MeV/A$ ^{108}Sn.

$$\begin{aligned} \text{Beam energy} &= 140 \times 108\ MeV, \\ &= 15120\ MeV = 15.1\ GeV. \end{aligned}$$

At this energy $\beta = 0.48$ — i.e. the projectile is travelling at half the speed of light!

11.6 Neutron Capture

Low energy neutron-capture cross-sections exhibit peaks manifesting a compound system and these peaks are often called *resonances*. An example is the neutron capture of ^{115}In to form ^{116}In.

Figure 88: Neutron capture resonance

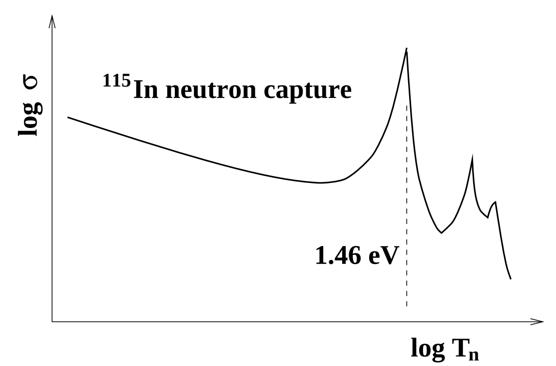

The neutron needs only $1.46\ eV$ to form an excited compound state in ^{116}In*. But note that the excitation energy in ^{116}In is much greater than $1.46\ eV$ – it is in fact $6.8\ MeV$! So even though we only put in $1.46\ eV$, the compound system is highly excited due to the binding energy of the neutron.

Figure 89: Neutron capture and decay

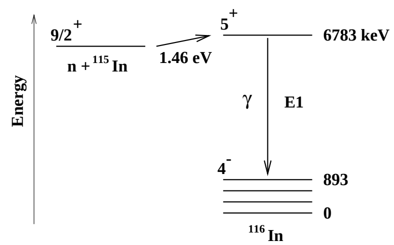

• Cross-section:

At $1.46\ eV$, the total cross-section for neutron capture is $\sigma \sim 2.8 \times 10^4\ barns$. This is much larger than the geometric cross-section ($\pi R^2 \sim 1.1\ b$, with $R \sim 6\ fm$). This is a *quantum effect* and we need to consider the *de Broglie wavelength* ($\lambda/2\pi$) instead of the nuclear radius – slow neutrons have a large wavelength and hence a long range influence. The cross-section becomes:

$$\pi R^2 \Rightarrow \pi \left(\frac{\lambda}{2\pi}\right)^2 .$$

The momentum of the neutron is:

$$\begin{aligned} p_n = \sqrt{2m_nE} &= \sqrt{2 \times 939 \times 1.46 \times 10^{-6}}, \\ &= 0.052\ MeV/c. \end{aligned}$$

The de Broglie wavelength is then:

$$\begin{aligned} \left(\frac{\lambda}{2\pi}\right) = \frac{\hbar c}{p_n c} &= \frac{197}{0.052}, \\ &= 3.7 \times 10^3\ fm, \end{aligned}$$

and hence the cross-section becomes $4.3 \times 10^5\ b$. The measured value is only 6% of this latter estimate – we must also consider other effects such as the spins of the neutron, target and compound nucleus.

• Decay of the compound state:

$$\begin{aligned} {}^{116}\mathrm{In}^* &\rightarrow n +{}^{115}\mathrm{In} \\ &\rightarrow \gamma +{}^{116}\mathrm{In}^* \end{aligned}$$

For compound nucleus decay, neutron decay with energies $> 1\ MeV$ are more likely than γ-decay. However, for the example of ${}^{116}\mathrm{In}^*$ the neutron could only be emitted with the same low $1.46\ eV$. Consequently, γ-decay (e.g. the $5.89\ MeV$ ($E1$) $5^+ \rightarrow 4^-$ transition) dominates, and we find that:

$$\frac{\Gamma_n}{\Gamma_\gamma} = 0.04,$$

i.e. there is a 96% probability for γ-decay and only a 4% probability for neutron emission.

At this energy, there are no other decay modes open and so

$$\frac{\Gamma_n}{\Gamma} \approx 0.04,$$

where Γ is the total decay width or decay probability ($\Gamma = \Gamma_n + \Gamma_\gamma$).

We can also link this decay fraction to the formation cross-section:

$$\pi \left(\frac{\lambda}{2\pi}\right)^2 \times \frac{\Gamma_n}{\Gamma}.$$

Recall that the measured formation cross-section was only 6% of the estimate using the de Broglie wavelength – this factor is similar to the partial neutron decay width!

• Wavefunction picture of a resonance:

There is a matching of the phase of the wavefunctions of the target and projectile at the surface of the target if the derivative at the surface is zero. Once there is a match to penetrate the target, it does not match to get out. There are many reflections and equilibration of the energy.

11.7 Proton Capture

In the case of charged-particle capture (and decay), we have to consider the *Coulomb barrier* which inhibits the formation (or decay). We need sufficient energy to overcome this barrier (several MeV) and so the wavelengths are much smaller than for neutrons. Consequently, the cross-sections for proton capture are $\sim 1\ b$ at maximum.

For heavier ions (e.g. α, ^{12}C, ^{32}S), the Coulomb barrier is larger still and the particle enters a *continuum* of very high level densities and overlapping resonances. The excitation energy of the compound nucleus is much higher (10–80 MeV) and since the neutron binding energy is only $\sim 8\ MeV$, several neutrons are emitted before γ-ray emission becomes dominant. These *fusion evaporation* reactions also bring large amounts of *angular momentum* into the compound system.

11.8 Charged Particle Decay

Figure 90: Neutron capture, proton decay

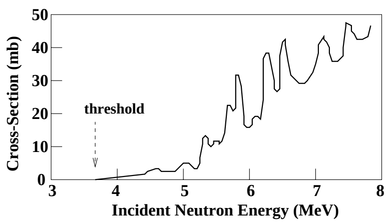

Consider the $^{23}_{11}$Na(n,p)$^{23}_{10}$Ne reaction – a neutron is captured by ^{23}Na to form a ^{24}Na* compound system which then decays by emitting a proton. The Q-value for this reaction is -3.59 MeV (i.e. energy to change n into p) and the threshold (neutron) energy is 3.75 MeV (taking into account the recoil energy of the ^{23}Ne nucleus). The Coulomb barrier for the outgoing proton has a height of ~ 4 MeV. Just above threshold, the proton channel is not present as the Coulomb barrier must be overcome. Above 5 MeV, the barrier becomes increasingly "transparent" to the outgoing proton and resonances occur – although the cross-sections are only mb!

11.9 Fusion-Evaporation Reactions

Heavy Ion (HI,xn) fusion-evaporation reactions are useful in nuclear structure studies. These reactions can bring in large amounts of angular momentum and excitation energy.

Figure 91: Fusion-evaporation reaction

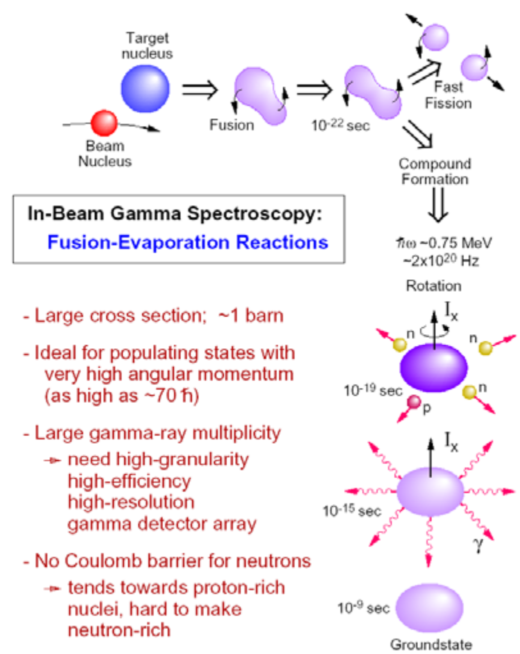

The angular momentum brought into the compound system is dependent on the impact position of the projectile on the target:

Figure 92: Induced angular momentum

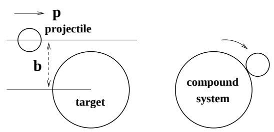

The angular momentum is: $\vec{l} = \vec{b} \wedge \vec{p}$, where b is the impact parameter and p the momentum of the projectile. The partial fusion cross-section is proportional to the angular momentum: $d\sigma_{fus}(l) \propto l$.

Figure 93: Fusion cross-section

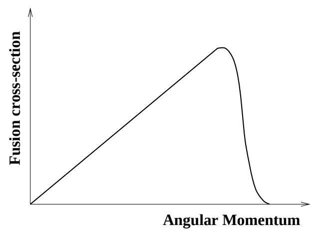

The nucleus ^{132}Ce can be formed by bombarding a stationary ^{100}Mo target with a beam of ^{36}S at an energy of $155\ MeV$ ($4.31\ MeV/nucleon$). At this chosen energy, the residual nucleus with the largest cross-section is ^{132}Ce which is produced by boiling off four neutrons.

• Compound nucleus formation:
$10^{-20}\ s$ after impact, the target has thoroughly absorbed the projectile to produce the excited compound nucleus ^{136}Ce*.

• Neutron emission:
After $10^{-19}\ s$, four neutrons are boiled off which each carry away large amounts of energy (at least equal to the binding energy of $\sim 8\ MeV$), but little angular momentum.

• Statistical (cooling) γ-ray emission:
After $10^{-15}\ s$, high energy ($E1$) γ-ray transitions remove excitation energy but little angular momentum. The nucleus "cools" towards the *yrast line* where all the excitation energy is involved in the rotation – $E \propto I(I+1)$.

• Quadrupole (slowing down) γ-ray emission:

After 10^{-12} s, quadrupole ($E2$) γ-ray emission takes over, dissipating the angular momentum – slowing down the nuclear rotation.

After about 10^{-9} s, the nucleus reaches its ground state after about 10^{11} rotations. This is similar to the number of revolutions of the earth since its creation!

Figure 94: Energy-spin plane

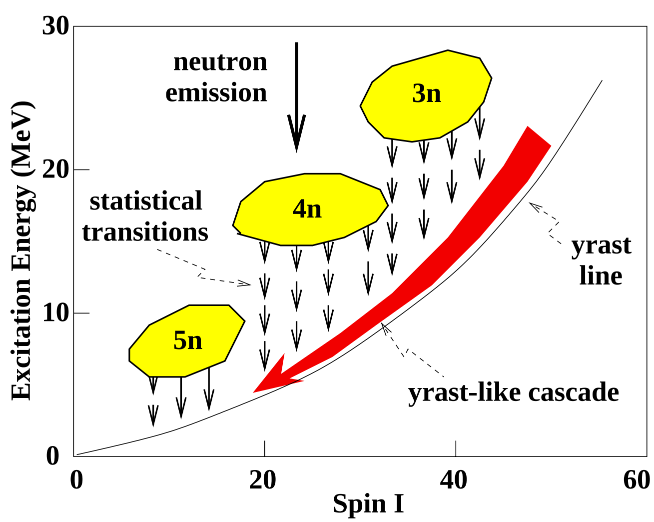

11.10 Transfer Reactions

Transfer reactions occur within a timescale comparable with the transit time of the projectile across the nucleus. The cross-sections are comparable to a fraction of the nuclear area and they vary smoothly and slowly with the projectile energy. The de Broglie wavelength of a 20 MeV incident nucleon is 1 fm and therefore it "sees" or interacts with individual nucleons. These will be the valence nucleons at the nuclear surface and they are transferred to/from the target nucleus.

For example, a (d,p) reaction *strips* a neutron off the projectile (deuteron) leaving a proton, and adds it to the target. Conversely, in a (p,d) reaction, the projectile (proton) *picks up* a neutron from the target to form a deuteron.

The angular distribution (variation of intensity with angle) of the outgoing modified particle (p or d) contains information on the orbit (state) of the captured (lost) neutron. For instance, it contains data on l the transferred angular momentum.

12: Nuclear Astrophysics

"Linking Femtophysics with the Cosmos"

12.1 Origin of the Elements

Big Bang: ^{1}H, ^{2}H, ^{3}He, ^{4}He, ^{7}Li

- Thermonuclear fusion in a rapidly cooling, expanding mixture of protons and neutrons $\Rightarrow$ $^{4}\mathrm{He}/^{1}\mathrm{H} \approx 10\%$ with very small traces of ^{2}H, ^{3}He, and ^{7}Li.
- Low binding energy of ^{2}H
- Stability of ^{4}He
- Lack of stable A=5 and 8 nuclei

Interstellar gas: Li, Be, B

- Spallation and fusion reactions between cosmic rays and ambient nuclei e.g.
  $\mathrm{p} + \mathrm{O} \rightarrow$ Li, Be, B
  $\alpha + \alpha \rightarrow {}^{6}\mathrm{Li}, {}^{7}\mathrm{Li}$

Stars

- Massive ($> 8M_{\odot}$) stars, type II supernovae
  Li, B, C to Fe, heavy (r: rapid)
- Low to intermediate ($< 8M_{\odot}$) mass stars
  Li, C, N, F heavy (s: slow)
- Type Ia supernovae (thermonuclear explosion of a white dwarf) Si to Fe
- Others (novae, black holes,...)

12.2 Turning Hydrogen into Helium

The fusion of four protons into helium is the only way to produce enough energy over the timescale of the Solar System, such that the Sun is still shining brightly today. The main reaction is:

$$4\ {}^{1}\mathrm{H} \rightarrow {}^{4}\mathrm{He} + 2\ \mathrm{e}^{+} + 2\ \nu,$$

which gives off energy. It is unlikely that four protons just happen to coalesce into helium; instead the four protons are processed into helium via a series of simple reactions: the *pp chain* or the *CNO cycle*.

12.3 The Proton-Proton (pp) Chain

This occurs in stars with masses $\leq 1.5 M_{\odot}$. The reactions are:

- ^{1}H + ^{1}H $\rightarrow$ ^{2}H + e^{+} + ν
- ^{2}H + ^{1}H $\rightarrow$ ^{3}He + γ
- ^{3}He + ^{3}He $\rightarrow$ ^{4}He + 2 ^{1}H, *pp1*, Q = 26.20 MeV
- ^{3}He + ^{4}He $\rightarrow$ ^{7}Be + γ
- ^{7}Be + e^{-} $\rightarrow$ ^{7}Li + ν
- ^{7}Li + ^{1}H $\rightarrow$ 2 ^{4}He, *pp2*, Q = 25.66 MeV
- ^{7}Be + ^{1}H $\rightarrow$ ^{8}B + γ
- ^{8}B $\rightarrow$ ^{8}Be + e^{+} + ν
- ^{8}Be $\rightarrow$ 2 ^{4}He, *pp3*, Q = 19.17 MeV

There are three end points when He is formed, each with an effective Q value (positive means energy released).

12.4 The CNO Cycle

The *CNO cycle* converts hydrogen into helium by a sequence of reactions involving carbon, nitrogen and oxygen isotopes, releasing energy in the process. It occurs in stars with mass $> 1.5 M_{\odot}$. The main reaction sequence is:

1. ^{12}C(p,γ)^{13}N, proton capture
2. ^{13}N(e^{+},ν)^{13}C, β deacy
3. ^{13}C(p,γ)^{14}N, proton capture
4. ^{14}N(p,γ)^{15}O, proton capture
5. ^{15}O(e^{+},ν)^{15}N, β decay
6. ^{15}N(p,α)^{12}C, proton capture, α loss

The net result is:

$$4\ ^{1}\mathrm{H} \rightarrow {}^{4}\mathrm{He} + 2\ \mathrm{e}^{+} + 2\ \nu, Q = 26.73 MeV.$$

The cycle is limited by the β decay rates of ^{13}N ($\tau \sim 10$ min) and ^{15}O ($\tau \sim 2$ min). At higher temperatures, proton capture on ^{13}N can begin to compete with the β-decay and the cycle can break out into the *hot CNO cycle*.

Figure 95: CNO and Hot CNO cycles

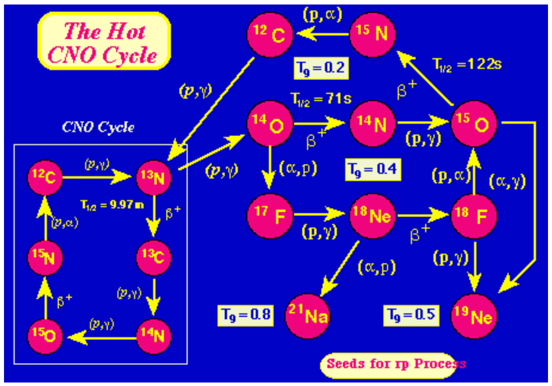

At still higher temperatures, reactions begin to compete that can break out of the hot CNO cycle and ignite a runaway sequence of nuclear burning.

Figure 96: Breakout of Hot CNO cycle

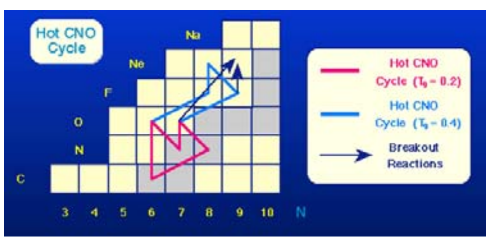

12.5 Explosive Nucleosynthesis

Evidence

- Technetium — no stable isotopes — in S stars
  Tc II lines identified in red giants with strong lines of Y, Zr, Ba, La, etc.

- Cameron (1955) proposed synthesis of these elements by neutron capture:
  neutrons from e.g. ^{13}C(α,n)^{16}O

Elements beyond Fe

- Nuclear fusion?
  Ruled out by B/A maximal at iron

- Neutron capture?
  Can occur at low T but needs high T to activate neutron sources

Stellar abundances imply two different processes

s-process	s ≡ slow	$N(n) \to 0$
r-process	r ≡ rapid	$N(n) \to \infty$

'Low' neutron flux is typically 10^8 neutrons/cm3,
'High' neutron flux is typically 10^{20} neutrons/cm^3.

Rapid proton capture — *rp-process* and rapid neutron capture — *r-process* produce exotic nuclei far away from the line of β stability.

Figure 97: The rp- and r-processes

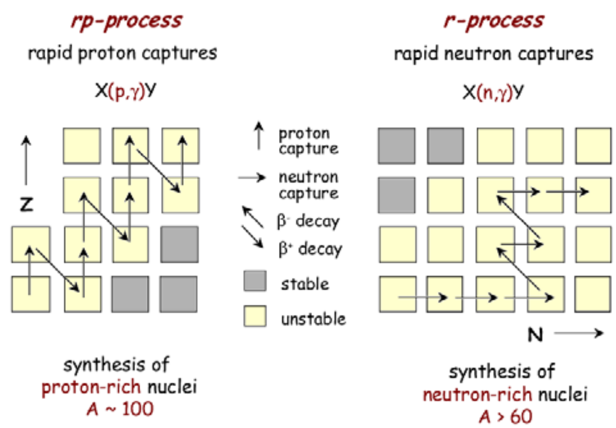

©M. Aliotta, Edinburgh Nuclear Physics Group

Figure 98: The creation of the heavier elements

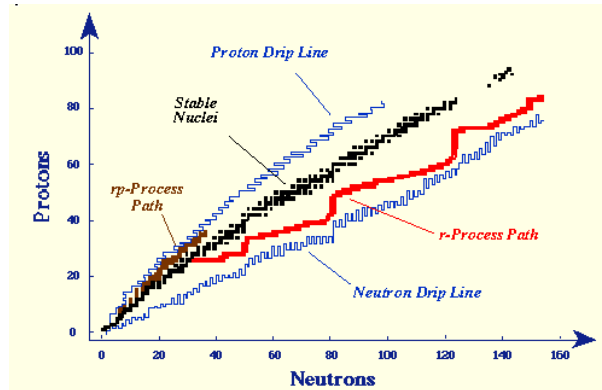

The production of elements in these sequences is described by a coupled set of network equations that give the nuclear abundances as a function of time.

12.6 The rp-process

This sequence of reactions typically lasts 10–1000 seconds, and is called the *rapid proton capture process* (rp-process). This is a series of radiative proton capture reactions and nuclear β^+ decays that process the lower mass nuclei into higher mass, radioactive nuclei.

Figure 99: Creation of proton-rich nuclei by the rp-process

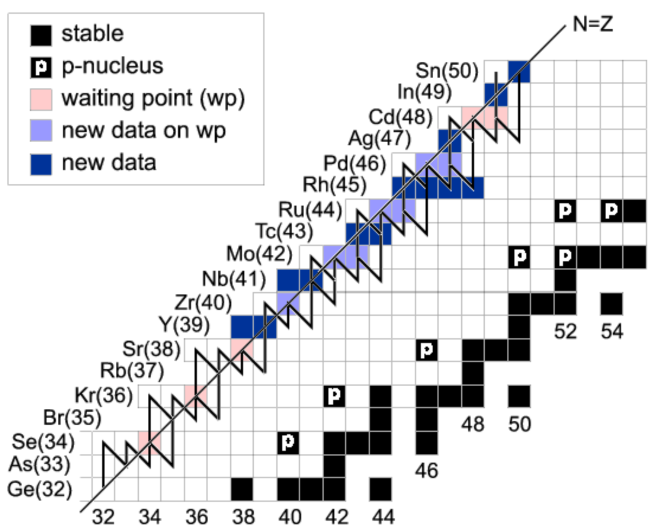

The end point of thr rp-process in thought to be light Te nuclei ($Z = 52$, $A \sim 106$).

Once the thermonuclear flash has ended, the remaining nuclei decay to stable mass nuclei up through the krypton isotopes.

The elemental abundances depend crucially on the reaction rates (cross-sections) — i.e. proton (neutron) capture vs. β-decay. These can now be studied using accelerated beams of *radioactive beams*. Several worldwide laboratories are being developed for such beams. An example is the measurement of the reaction ^{21}Na(p,γ)^{22}Mg recently carried out at TRIUMF Canada, using a radioactive ^{21}Na beam.

Figure 100: ^{21}Na beam and ^{22}Mg recoils

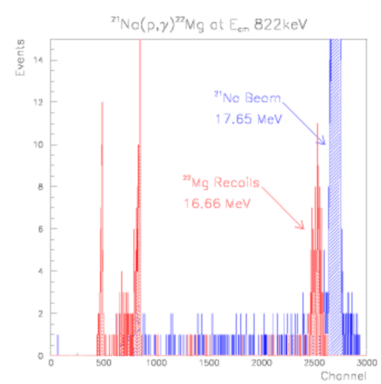

12.7 Astrophysical sites of the rp-process

Figure 101: Binary system accretion disk

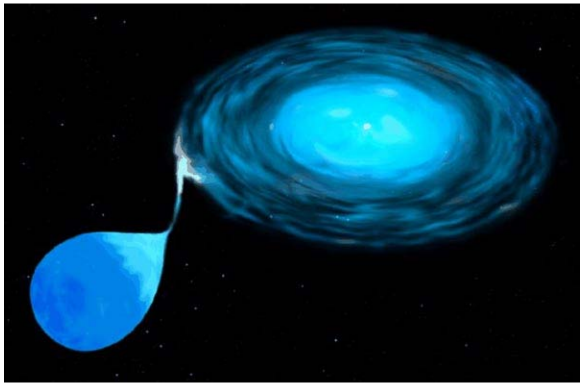

Four astrophysical sites have been proposed for the rp-process:

- novae
- X-ray bursters
- shock waves pasing through the envelope of supernova progenitors
- Thorne-Zytkow objects — a neutron star merges with a supergiant and sinks to its centre

12.8 Neutron-rich nuclei

Adding more and more neutrons to a nucleus may change the shell structure. It has been predicted that the *shell gaps* (magic numbers) are washed out far from the line of stability. Some evidence comes from the measured abundances of r-process nuclei. Theoretical calculations including *quenched* shell structure appear to describe the data better.

Figure 102: Abundances of r-process elements

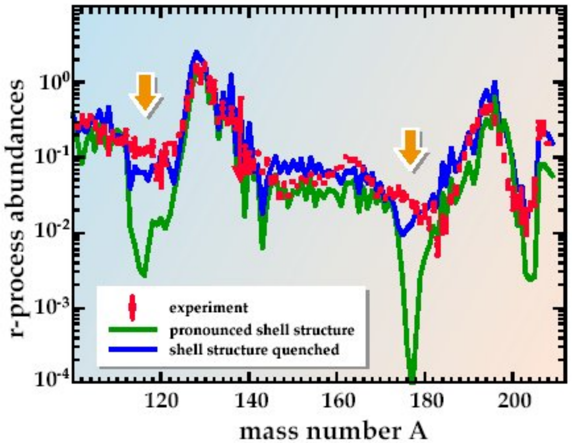

Figure 103: Quenching of shell structure in neutron-rich nuclei

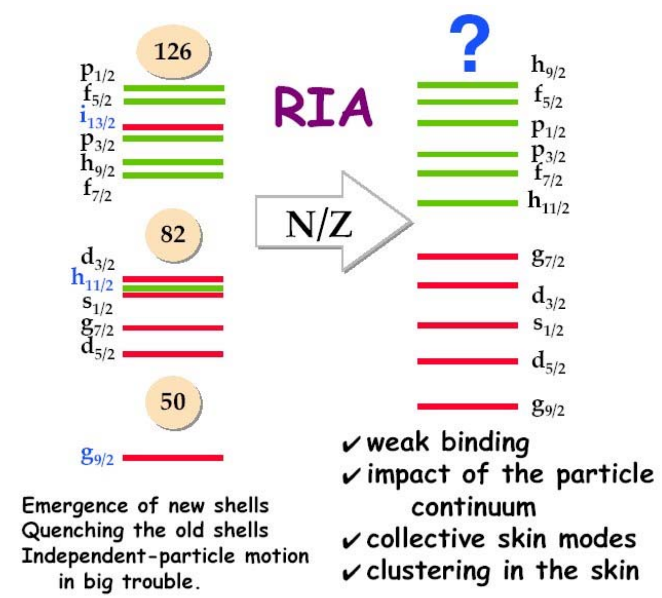

©Witek Nazarewicz, ORNL

13.1 Radioactive Ion-Beam Physics

From GANIL (EXOGAM) website:

Figure 104: Physics with radioactive beams

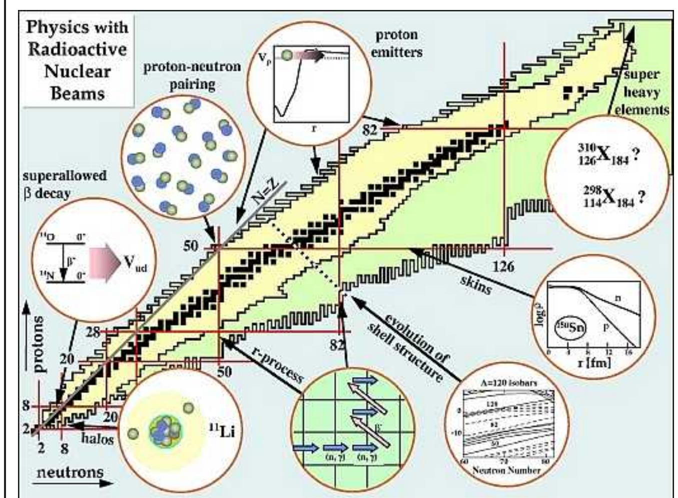

• Proton-rich systems:

The addition of protons to a nucleus rapidly decreases the binding energy of the system through the increase in the repulsive electrostatic interaction between protons; as a consequence nuclei are rapidly reached which are unstable towards the emission of protons. The majority of our current understanding of nuclei and their structure comes from studies of moderately proton-rich species. The production of very proton-rich nuclides, near to the proton dripline, is limited by the use of stable beams because of the extremely small production cross-sections for pure neutron emission. These restrictions will be lifted by the use of radioactive beams since it will become feasible to populate such nuclei via the much more prolific charged particle evaporation channels. Not only do such channels correspond to higher cross-sections, but charged-particle emission facilitates rather easy high efficiency selection of the nuclei of interest if appropriate ancillary detectors are used in conjunction with a γ-ray spectrometer.

• Self-conjugate nuclei:

Of the proton-rich species, systems with N = Z are of particular interest. For masses less than 40, N = Z self-conjugate nuclei are strongly bound and β stable, whereas for A > 56, the line of β stability moves away towards more neutron-rich systems and N = Z nuclei become progressively less bound as

the mass increases. With increasing mass, such systems become more and more difficult to access experimentally. Structurally, self-conjugate nuclei are important for the high degree of symmetry they display between the proton and neutron degrees of freedom. Protons and neutrons simultaneously fill identical single-particle orbitals, leading to a large overlap between nucleon wavefunctions. Such systems are therefore subject to very strong correlations in their motion which can amplify many structural phenomena. A rich variety of different types of structure are exhibited; oblate and prolate deformed systems, spherical and superelongated systems occur and the changes in structure from one nuclide to another, and also structural evolution with angular momentum and excitation within a single species, are sudden and dramatic. Such nuclear landscapes provide stringent tests of our nuclear models. Furthermore, the rp-process passes through these isotopes and structural properties can influence these reactions chains. There is no definite astrophysical site in which the rp-process is known to occur and so such information is important in order to locate and understand possible explosive nuclear synthesis sites.

• Nuclear structure around ^{100}Sn:

The self-conjugate nucleus, ^{100}Sn (N = Z = 50) has recently been shown to be bound in its ground state by experiments carried out at GSI and GANIL. Its excited states are expected to be bound up to ~ 4 MeV and higher states might be quasi-bound by centrifugal and Coulomb barriers, which can confine nucleon wavefunctions, even when the proton separation energies are small. It is expected that this nucleus has a rather simple structure associated with a doubly magic system. However, the actual binding energies are very sensitive in such a weakly bound system to residual interactions and correlations. The regions around doubly magic nuclei have traditionally been the source of experimental matrix elements used as input for shell-model descriptions of large regions of nuclei. The study of excited states in ^{100}Sn and neighbouring nuclei, via observation of their electromagnetic decay, will provide important information about the nuclear mean field, spin-orbit and residual interactions and nucleon correlations

which would be of relevance to the structure of all medium-mass nuclei. Furthermore, the study of the polarising effects of excited valence nucleons, such as those seen in particle-hole states in ^{16}O and ^{40}Ca doubly magic systems, could be extended with the application of radioactive beams to γ-ray spectroscopic measurements in ^{56}Ni and ^{100}Sn. Studies of these polarising effects can then be related back to the issue of the onset of stable ground-state deformation.

• Valence nucleon interactions: T=0 pairing:

The N = Z nuclides also provide a unique system for the study of certain valence nucleon interactions which affect nuclear structure in various ways. The valence nucleon interaction can be split up into two forms: a T = 1 force giving rise to the well known p-p and n-n pairing correlations and a T = 0 force which gives rise to collectivity and deformation via configuration mixing. The T = 0 force appears predominately in monopole and quadrupole forms; the latter playing a key role in the development of quadrupole collective effects in deformed regions and quadrupole vibrational degrees of freedom. The

T = 0 monopole component is less well known but has been encountered in light N = Z nuclides. It is of great interest to study such effects in medium-mass systems, where level densities are high enough for the monopole T = 0 force to give rise to a potentially well-developed pair field. It might be possible for such neutron-proton pairing interactions to lead to the development of a pairing gap in odd-odd systems or effects in the alignments of nucleon pairs at moderate spins and other phenomena. These would be apparent in measurements of the γ-decay of energy levels in such nuclei. It is known that the T = 0 effects in N = Z nuclei are large, and the magnitude drops rapidly when moving away from nuclei in the vicinity of N = Z. Self-conjugate nuclei are thus unique candidates for investigating such phenomena.

• Isospin symmetry:

More subtle aspects of self-conjugate nuclei concern various aspects of isospin. The demise of isospin symmetry has not been properly addressed since it remains a fairly good symmetry throughout the known periodic table. Coulomb effects are small in

light nuclei and washed out by a neutron excess in heavier systems, leading to a persistence of isospin symmetry. Along the N = Z line however, a large Coulomb energy can be built up, without the relief of a neutron excess, thus breaking the symmetry in the behaviour of charged protons and chargeless neutrons. Recent estimates of isospin mixing indicate that it has a roughly $Z^{8/3}$ dependence for self-conjugate nuclei. This would correspond to admixtures of T = 0 components of around 5% in the ground-state wavefunction of ^{100}Sn, hence suggesting that the structure of this nucleus may not be as simple as first imagined. No other region allows access to nuclei exhibiting such extreme breakdown in this symmetry. Measurements of the electromagnetic transitions between low-lying states in the heavier N = Z systems could elucidate these expectations with the observation of E1 transitions which are forbidden for self-conjugate nuclei in the case of perfect symmetry.

• Mirror nuclei:

The spectroscopy of mirror nuclei (N = Z + 1 or Z – 1) provides information on the difference between the proton and neutron nuclear potentials. Spectroscopic studies in mirror nuclei allow a systematic study of the changes between the positions of proton and neutron Fermi surfaces. The interplay between Coulomb and nuclear forces can also be studied via Coulomb energy differences in mirror nuclei. With radioactive beams, it will be possible to study far heavier pairs of mirror nuclei than is currently feasible, and moreover, to study them to high spin. Results of an experiment to investigate the mirror pair ^{49}Mn/^{49}Cr have shown that there is a clear correlation between the behaviour of the Coulomb energy differences and the rotational alignment of nucleons.

• Spectroscopy of nuclei beyond the proton dripline:

Nuclear species beyond the proton dripline are unbound towards proton emission. With radioactive ion beams it becomes possible to populate some unbound systems. In principle, electromagnetic decays can compete with particle emission, but only realistically in cases where the latter is hindered in some way. For low-lying states with high angular

momentum, particle emission probabilities can be reduced by the effects of Coulomb and centripetal barriers and such states might well decay by emitting γ-rays as in a normal bound system. The subsequent proton decay of lower-lying states can then be used to identify the γ-emitting nuclide. Such techniques, combining an array of γ-ray detectors with measurements of proton radioactivity using a radioactive beam, will open up previously unstudied regions of the Segre chart, for example, the predicted deformed region centred on very neutron-deficient gadolinium isotopes. In addition, it will allow studies to be made of the relative particle- and γ-decay probabilities and the rather sensitive role that structure is expected to play in that competition.

• Neutron-rich systems:

The structure of neutron-rich nuclei presents a major challenge to our understanding of nuclei as a whole. The development of a large excess of one type of particle in nuclei leads to the expectation that the physics of such systems is liable to be fundamentally different from that which we are used to in neutron-deficient and near-stable nuclei. Changes are expected in nucleon-density distributions and effective interactions, which lead to alterations of nuclear structure as discussed below. The nucleus can bind a much greater excess of neutrons than protons, hence the neutron dripline is very far from stability. As a consequence it has only been reached for the very lightest systems. The position of the neutron dripline in heavy systems is an open and hotly debated question. Recent calculations have indicated that a substantial difference between proton and neutron rms radii develops with increasing neutron excess. These effects are established in light systems where neutron haloes have been experimentally observed. The presence and extent of neutron skins in heavier systems are not fully established and the effects of the development of such a neutron skin in medium- and heavy-mass systems are an open question. If such a change in the density distributions of the two nucleon systems arises, this will be reflected in a concomitant alteration in the geometries of the associated nucleon potentials. The resulting change in the mean fields would influence the single-particle

structure near the Fermi surface and therefore have a dramatic effect on the structure of neutron-rich nuclides. Studies of such systems therefore hold the key to addressing the issue of whether a measurable difference does develop between the charge and mass distributions with increasing neutron excess. This would yield information on the relative strengths of the isoscalar and isovector components of the nucleon interaction; e.g., are protons pulled out by the neutron excess thereby reducing charge densities and altering binding energy and stability, or does a neutron skin develop? If so what are its structural consequences?

The spin-orbit interaction was introduced in the early years of nuclear structure to account for the observed sequence of magic numbers in the nuclear system. Its strength obviously has a direct effect on nuclear structure by shifting the ordering and energetic locations of single-particle orbitals. There are predictions that the strength of this interaction is modified by an increasing neutron excess, although a theoretical consensus has not yet emerged. Observation of modifications of structure by changes in the spin-orbit interaction would give insight into the origins of the interaction itself; for example, is it generated by a purely two-body force, or as some theorists suspect from studies of light nuclei, does it have many-body components?

The nuclear pairing interaction has had a profound effect in our appreciation of nuclear structure. In weakly bound systems the nucleon pairing interaction may scatter pairs of particles from bound to continuum states, drastically increasing the pair correlations to the extent that the behaviour of nucleons is altered and structure modified. Such phenomena might be observable in the most neutron-rich species near the drip line, manifest by a possible increase in pair gaps or delay in band-crossing frequencies.

• Coulomb excitation:

At the simplest level, Coulomb excitation to the low-lying states would be able to quickly map out the basic structural features of whole regions of nuclides. A simple measurement of the positions of the first two or three excited states will enable the development of vibrational collectivity and

deformation to be observed. Such effects are influenced to a large degree by the valence single-particle structure, orderings of levels, pairing and major shell gaps. Modifications to fundamental nuclear properties (potential, effective interactions and pairing) would influence the single-particle structure near the Fermi surface, and therefore the basic features exhibited by the structure of low-lying states. A recent example of the use of such methods has employed intermediate-energy Coulomb excitation of a ^{32}Mg beam from fragmentation reactions. Measurements made on just the first excited state have produced evidence that the well-known N = 20 spherical shell gap is broken down by the onset of strong deformation in heavy neutron-rich isotopes.

• High-spin spectroscopy of neutron-rich isotopes:

The measurement of medium- to high-spin states has been a fruitful area of research in testing the validity of our understanding of nuclear structure. Such states are populated in heavy-ion fusion-evaporation reactions, which, with stable beams, imposes the restriction of studying only moderately proton-rich systems, due to the curvature of the line of stability. The study of nuclear properties at high angular momentum sheds light on the various modes of excitation that nuclei can accommodate and the evolution of such modes as a function of spin and excitation. The study of exotic metastable shapes (for example, octupole, super- and hyper-deformation) in nuclei provides severe tests for nuclear theories; many of the predictions of such states occur at moderate spins in stable and neutron-rich nuclei. Observations of high-K isomers based on yrast many-quasiparticle states can elucidate the effect of extensive blocking of valence orbitals on the nucleon pairing interaction. Again, many predictions of such yrast isomers occur in nuclei only accessible to study with a γ-ray spectrometer deployed at a radioactive ion beam facility.

High-spin studies also address the general problems of modifications to shell structure and nuclear properties by an increasing neutron excess discussed previously, but now with the added variables of spin and excitation. Do potentials and effective

interactions alter at high spin as shown by changes in shell gaps, deformation and band-crossing frequencies, or does the presence of appreciable angular momentum alter the development of a neutron skin? Is pairing quenched at high spin or does continuum coupling allow it to persist? Such questions are open at the present time.

• Extension of complete spectroscopic measurements in stable nuclei:

Very complete low-spin information exists for some stable nuclei through detailed studies of electromagnetic transitions following neutron capture reactions. Spectroscopy of such systems can be guaranteed to be 'complete', in the sense that all states below a particular spin (around 4–5$\hbar$) and excitation energy (a few MeV) are certain to be populated. Such extensive data sets have been used to establish the existence of certain symmetries in the nuclear structure of low-lying levels, as described by, for example, the interacting boson models. The point in spin or excitation at which such symmetries are broken, and the role of other nuclear properties in lifting such symmetries, are unknown due to the lack of information extending neutron capture studies to a higher spin and excitation regime. Spectroscopic measurements of such stable systems, at higher spins than those available in neutron capture, would begin to address these areas, but radioactive heavy-ion beams are required.

• Structure of heavy nuclei:

Nuclear collectivity depends on the availability of specific combinations of nuclear configurations near the Fermi surface. Collective modes appear when pairs of orbits are available which have large matrix elements for the appropriate operator. For example, octupole effects are seen when protons or neutrons differing in orbital angular momentum and total spin by three units are active near the Fermi surface. Other combinations of exotic configurations will become accessible with the advent of radioactive beams. The heavy nuclei offer prospects of investigating even higher multipole modes of excitation. For example, the hexadecapole mode could be studied in heavy Pd (A $\sim$ 116–120) and Os (A $>$ 192) nuclei, where high-K unique-parity

proton and neutron orbits, favourable to large ε_4 shape components, lie close to the Fermi surface. Another exciting possibility is the chance to observe a $\Delta l = 5$ collective mode by reaching nuclei such as the neutron rich Ra-Th isotopes, where $\pi(p_{3/2} - i_{13/2})$ and $\nu(d_{5/2} - j_{15/2})$ orbit pairs favour the creation of excitations with sufficient two-quasiparticle components to generate collectivity in this highly exotic mode. It is not feasible to study such modes with stable beams and targets.

There is no definite evidence for the existence of rotationally stabilised triaxial shapes in nuclei. Such nuclei are expected to occur when the shape-driving effects of valence protons and neutrons are in an opposite sense (i.e., one prolate- and one oblate-driving). This generally occurs when one Fermi surface is at the bottom of a major shell and the other at the top. In heavy nuclei such situations will occur in extremely neutron-deficient or -rich species. For example, the light Hf to Pt nuclei with N $\sim$ 90 would be good candidates with which to pursue stable triaxiality. However, the best examples for studying such states lie just beyond the lightest nuclei that can be populated at high-spin with stable beams and targets. Similarly, oblate ground-state deformation has been observed in very few nuclei (some Pt and Au isotopes). Here oblate-driving proton and neutron orbits are required. Interesting candidates might be found in neutron-deficient Se/Kr nuclei, light Ba isotopes and Au systems. In order to reach candidates for either phenomenon, radioactive beams are necessary.

It has been suggested that nucleon transfer prior to the fusion of two nuclei can lead to large enhancements in sub-barrier fusion cross sections. Transfer reactions involving reaction participants with loosely bound nucleons occur at larger radii than those involving well-bound stable systems, providing further information on sub-barrier effects. Heavy beams with exotic N/Z ratios may also yield enhanced multiple pair transfers, as equilibration of the N/Z ratio favours the onset of neutron and proton currents, whose consequences may lead to new physics. A possible example is related to the

pairing degree of freedom and the associated multipair transfer processes. At large inter-nuclear distances proton transfer is inhibited because of the Coulomb barrier, neutron transfer is therefore favoured, especially if one of the participants is neutron rich. If it were possible to transfer a large number of pairs then that could give rise to new modes of collective motion, and a new method of synthesising neutron-rich nuclei.